Preparation and characterization of biopolymeric microparticles for surface-enhanced Raman spectroscopy and fluorescent microscopy imaging

Ph.D. Thesis

Author

Malik Hadi Mahmood

Supervisor:

Dr. Miklós Veres (Wigner RCP)

Doctoral School of Physics
Department of Optics and Quantum Electronics
Faculty of Science and Informatics
University of Szeged

Institute of Solid State Physics and Optics
Wigner Research Centre for Physics

Szeged, Hungary 2021

I am dedicating this thesis to my beloved wife and daughters.

Table of contents

List of abbreviations

θ_{det}	Half-angle of light collection
λ_{em}	Emission wavelength
λ_{exc}	Excitation wavelength
^{60}Co	Cobalt-60
A	Adenine
AEF	Analytical enhancement factor
C	Cytosine
CCD	Charge coupling device
CDHC	Cystamine dihydrochloride
CdTe	Cadmium telluride
CE	Chemical enhancement
CF	Color filter
DC	Degree of conversion
DEGDMA	Diethylene glycol dimethacrylate
DFT	Density functional theory
DNA	Deoxyribonucleic acid
DTA	Differential thermal analysis
EDMA	Ethylene dimethacrylate
EF	Enhancement factor
EM	Electromagnetic
FITC	Fluorescein isothiocyanate
FPS	Fluorescent polystyrene
fps	Frame per second
FTIR	Fourier transform infrared
FWHM	Full width at half-maximum
G	Guanine
GMA	Glycidyl methacrylate
kGy	kilogray
LSFM	Light-sheet fluorescent microscopy

LSP	Localized surface plasmons
LSPR	Localized surface plasmon resonance
MCH	6-mercapto-1-hexanol
NA	Numerical aperture
NA_{det}	Detection numerical aperture
NA_{exc}	Excitation numerical aperture
NDF	Neutral density filter
NEF	Normalized enhancement factor
NMR	Nuclear magnetic resonance
NPs	Nanoparticles
OPFOS	Orthogonal plane fluorescence optical sectioning
PATP	P-aminothiophenol
PL	Photoluminescence
PS	Polystyrene
R6G	Rhodamine 6G
R_{axial}	Axial resolution
$R_{lateral}$	Lateral resolution
SEM	Scanning electron microscopy
SERS	Surface-enhanced Raman scattering
SMEF	Single molecule enhancement factor
SPIM	Selective plane illumination microscopy
SPP	Surface plasmon polariton
SPR	Surface plasmon resonance
T	Thymine
TCEP.HCl	Tris(2-carboxyethyl)phosphine hydrochloride
TEGDMA	Triethylene glycol dimethacrylate
TL	Tube lens
UDMA	Urethane dimethacrylate

1. Introduction and goals

Polymer materials nowadays are essential parts of everyday life. Hundreds of thousands of polymer building blocks – monomers – have been discovered, together with a large number of preparation and modification methods, allowing to fabricate polymers with a broad variety of sizes, shapes, chemical and physical characteristics. Hydrophilic or hydrophobic, soft or hard, bulk or porous, insulating or conducting, light emitting or light absorbing, nano-, micro-, or kilometer-sized – polymers allow to fabricate materials with wide spectrum of properties – in many cases even from the same monomer.

In my research, I was focusing on the preparation and laser spectroscopic study of micron-sized polymeric objects – microparticles for different applications. Polymeric micro- and nanoparticle systems are utilized in many different areas such as in drug delivery systems, vaccines [1,2], biomedical diagnostics, aerosol research and tracking [3,4], as fillers, reference particles in simulation experiments, process troubleshooting, etc. Some tasks require highly monodisperse microparticles that are easiest to fabricate from polymeric materials. In addition to those inherited from the monomer, the properties of a polymeric structure can strongly be influenced and controlled using additives. The incorporation of organic dyes into polymer matrices enables the creation of novel and desirable structures for a variety of applications in the technology, including life sciences (as biomarkers for biological imaging) [5–9], flow devices [10], and biomedical areas [11]. While the traditional organic dyes and fluorescent proteins exhibit high photobleaching rate during in vivo or in vitro imaging, making long-term imaging difficult due to sample photodamage [12], the incorporation of the fluorescent molecule into a host polymer microparticle can be a good strategy for reducing photobleaching and photodamage [13].

Another promising application of polymeric microparticles is their use as supports for surface-enhanced Raman spectroscopy (SERS). Raman spectroscopy is based on the inelastic scattering (Raman scattering) of photons by the characteristic vibrations of molecules, crystal lattice, and other structural components. This method can be used to investigate a wide variety of organic and inorganic, solid, liquid, and gaseous, ordered and disordered materials [14–16]. With this technique, no sample preparation is required, and the sample does not deteriorate under proper measurement conditions. The Raman signal is inherently weak, but a strong signal enhancement can be observed if the analyte molecule is adsorbed on a surface consisting of active metal nanostructures like gold and silver. This effect is known as surface-enhanced

Raman scattering [17]. SERS is working on metallic nanoparticles or nanostructures in colloidal or solid substrate form. Being a promising technique with proven single-molecule detection development of efficient SERS agents is targeted by many research projects. In SERS substrate development gold coating of nano- or micro-sized morphologies fabricated by lithography [18,19], chemical modification of gold and silver, attachment of metallic nanoparticles to different substrates [20] are the main development areas. In spite of the huge efforts and successful developments, there is still a lack of easy, reproducible, effective and cost-efficient preparation methods for SERS substrates. While the group of metals suitable for SERS is limited, there are much more possibilities in case of the supports, and polymers could be promising materials for that. SERS agents on polymeric supports were fabricated earlier by Cao *et al.* [21] and Chen *et al.* [22]. Polymeric microparticles have several advantageous properties as SERS supports. They can be used to fabricate large-area SERS substrates from dense microparticle monolayers or flow-through SERS cells by filling channels with the spheres; as single microparticles, they can easily be delivered in fluid or gas streams for remote sensing. The exposed parts of the microparticle not covered with the metal can also be functionalized to facilitate the attachment to specific sites.

Several methods are known to produce polymeric microparticles, including suspension, emulsion, solvent polymerization [23–25]. The main disadvantage of these preparation methods is their dependence on surfactants and stabilizers as basic additives in the polymerization in order to maintain the polymer phase in the synthesized solution, reduce the accumulation of product particles, prevent adhering to the solution [26,27]. In contrast, gamma radiation-initiated precipitation polymerization is a facile method to fabricate polymeric microparticles [28]. The activation of the monomers by high-energy radiation requires only the monomer and the solvent for the chemical preparation, so the particles can be created without any initiator or stabilizer. This easy and relatively simple technique allows to control the shape, size, and size uniformity of produced particles through the composition of the monomer mixture, irradiation dose, dose rate, and even the reaction time [29]. The wide pool of monomers allows to fabricate microparticles of specific surface properties.

My work was aimed to develop polymeric microparticles for fluorescent imaging and surface-enhanced Raman spectroscopic applications. For this, diethylene glycol dimethacrylate (DEGDMA) has been selected as a monomer. DEGDMA based polymers are widely used in dentistry [30,31], and this biocompatible material was found to be a highly flexible subject for polymer synthesis by gamma radiation initiated polymerization [32–34]. While having only a

monomer solution, the use of appropriate solvent and concentrations allows to fabricate bulk, micro- and microporous, and even DEGDMA-polymer particles. In general, precipitation polymerization can be used to obtain monodisperse DEGDMA microspheres.

My work included the following tasks:

1. Study the degree of conversion of DEGDMA polymers by Raman spectroscopy with different solvents. The monomer solutions of different concentrations were irradiated by various doses of gamma radiation, and this research allowed also to study the reaction kinetics of the polymerization and to determine its parameters by fitting with the Avrami equation.

2. Optimize the preparation conditions for DEGDMA microparticles obtained by gamma radiation-initiated polymerization technique and characterization of the obtained microspheres with different methods.

3. Synthesize fluorescent monodisperse microparticles through incorporation of FITC dye into the DEGDMA structure during gamma radiation-induced polymerization technique. Characterize the fluorescent microparticles with different methods and test their performance. The wide applications of using the fluorescent particles in the imaging field motivated me to build light-sheet fluorescent microscopy as part of my research and utilize it in imaging of prepared fluorescent microparticles.

4. Develop a technique to fabricate SERS substrates consisting of DEGDMA microparticles decorated with gold nanoparticles. Examine the performance and capabilities of the obtained SERS substrates by the detection of biomolecules.

2. Scientific background

The main purpose of this chapter is to provide a basic theoretical background of the materials and methods used in this work. It furnishes a scientific introduction to the principles and theoretical considerations of photoluminescence and light-sheet fluorescent microscopy, Raman spectroscopy, surface-enhanced Raman scattering and gamma radiation-induced polymerization as methods used to fabricate and characterize the microparticles used in the study.

The chapter is divided into two main sections related to polymeric microparticles and microscopic and spectroscopic techniques used. The first section explains free radical polymerization and how to use gamma radiation-induced polymerization as a technique to prepare polymeric, fluorescent micro/nanoparticles, and polymeric SERS-active substrates. The second section illustrates an overview of the photoluminescence effect, and the origin of light-sheet microscopy and its developments are given in brief, theoretical approaches describing the Raman scattering phenomenon, and followed by an introduction to the principles of the surface-enhanced Raman scattering effect.

2.1. Polymeric microparticles

In my research, diethylene glycol dimethacrylate (DEGDMA) monomer was utilized in all experiments. DEGDMA is a member of the vinyl family of polymers, in which carbon–carbon double bonding is present (Figure 1) [35], and is one of the commercial materials used in dental composites [30]. The polymerization and crosslinking process of the DEGDMA monomer that we investigated belong to the radical polymerization reactions. In this case, the initial system consists of the monomer and the solvent (and if necessary, the initiator). The rate and kinetics of the polymerization and properties of the resulted polymer depend on many factors, including the type of solvent, concentration ratios, temperature, *etc.* [33].
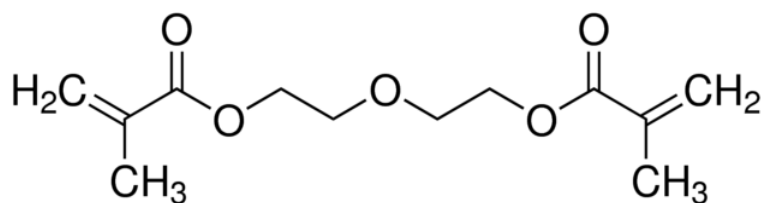

Figure 1: Chemical structure of diethylene glycol dimethacrylate (DEGDMA) monomer.
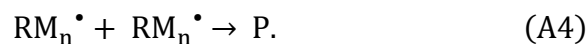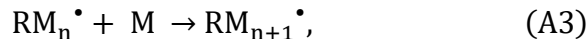
2.1.1. Free radical polymerization

Polymerization is divided into two classes according to modern terminology: chain-growth and step-growth polymerizations. They differ in a number of features: (i) the identities of the species that are capable of reacting with one another and (ii) the way in which the molecular size of the polymer is affected by the degree of conversion. The stepwise reaction between the functional groups of reactants, when pairs of reactants are combined at each step to form a longer polymer molecule, is known as step-growth polymerization, more details in Ref. [35]. In chain-growth the only chain-extension reaction step is the addition of a monomer to a growing chain with an active centre (free radical, *etc.*). Free radical polymerization is the most widely used method of chain-growth polymerization. Several ways are known for carrying out this polymerization such as block, suspension, emulsion, solvent polymerization. The mechanism of the polymerization reactions is complex, but can be divided into three main steps: initiation, chain-growth (propagation) and chain transfer or chain closure (termination) [35,36].

The first step is to create a nucleus or a centre capable of initiating active growth. Activation can be induced by chemical or physical methods. For chemical initiation, the radicals (radical is an atom, molecule, or ion that possesses an unpaired valence electron; the presence of unpaired electrons causes radicals to be extremely reactive chemically) are formed from the monomers by the influence of other substances in the monomer mixture that decompose relatively easily into radical initiators. These substances then undergo some chemical reactions with the monomer. Radical formation can be initiated also by physical effects, like heating or radiation (UV light, gamma-radiation). Radiation-initiated polymerization in the liquid phase most often occurs with a radical mechanism at or above room temperature [35,36].

During radiation initiation, the active centers are produced by irradiation. Depending on the type of radiation, we can talk about photoinitiated or ionizing radiation initiation. In photoinitiated polymerization, the radicals are formed upon the interaction of the monomer mixture with photons (most of the time UV light is used). This kind of chain-growth polymerization process also involves initiating, propagating, and terminating the reaction. Photoinitiated radical polymerization is particularly well suited for monomers containing carbon–carbon double bonds, such as methacrylic monomers. Limitations of photoinduced polymerization are short penetration depth and length dependency of light absorption, which limits the size and shape of the prepared polymer. Another drawback related to the polymerization mechanism, the photoinitiator is required for the initiation step [33,35–38].

In contrast, the absorption of high-energy radiation is not selective because the energy of the radiation exceeds the energy of chemical bonds by several orders of magnitude. High-energy radiation (gamma, electron, and X-ray) produces active centers that are formed with the help of fast electrons. These radicals are generated directly on the monomer and solvent, so no initiator is required. During the gamma irradiation process, the polymerization can be started at any temperature and under any conditions; we have a wide range of monomers and polymers (because the energy absorption of the radiation is not selective); the polymerization and crosslinking process can be controlled on a wide scale as required. Because the process does not require additives (there are no any initiators or catalysts whose residues can contaminate the product), a pure product can be easily obtained [39].

In the case of gamma or electron irradiation, the $R^\bullet$ radicals formed from the molecules of the monomer (M) or the solvent (O) can be considered as homogeneously distributed in the first approximation (A1) [36,40]:

$$M, O \xrightarrow{\gamma} R^\bullet, \qquad\qquad\qquad (A1)$$

$$R^\bullet + M \rightarrow RM^\bullet, \qquad\qquad\qquad (A2)$$

$$RM_n^\bullet + M \rightarrow RM_{n+1}^\bullet, \qquad\qquad (A3)$$

$$RM_n^\bullet + RM_n^\bullet \rightarrow P. \qquad\qquad (A4)$$

As an initial step in radical polymerization, the $R^\bullet$ radical is added to the monomeric molecule in reaction (A2), followed by series of additions according to (A3). The growing radical chain has a short average life: a chain of more than 1000 units can be formed in 10^{-2} to 10^{-3} sec [29]. The growing macro radical nucleus is very reactive and several side reactions (branching) can occur during the chain reaction. The stopping of the chain-growth, or chain closure termination (A4) can take place in several ways: by the interaction of two chain ends, reaction with another molecule (solvent, monomer radical) and due to pollution (oxygen).

In the case of DEGDMA monomer, with the formation of the crosslinked polymer, the system in some cases is no longer in a homogeneous phase because the polymer precipitates out of solution, so the system becomes heterogeneous. Macro radicals may remain in the polymer that precipitates from the mixture, which, depending on the state of the system, self-seal or continue to grow upon reaction with the diffused monomer. Crosslinking can result in the formation of

pores and networks of different sizes (Figure 2). The purity of the solvent is particularly important because contaminants can inhibit polymerization.
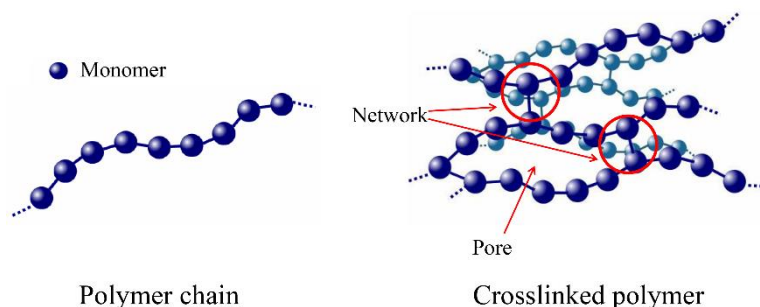

Figure 2: Diagram of crosslinked polymer.

Upon polymerization, the degree of conversion (DC) is one of the key factors used to prove the efficiency of the polymerization process. DC is the percentage of monomer which was polymerized and is determined by measuring quantities being specific to the monomers and the end-product. The simplest method to evaluate the DC is the mass difference, which means measuring the weight of the monomer and the weight of the polymer. Beside the mass difference method, several spectroscopic and other techniques such as Raman or Fourier transform infrared (FTIR) spectroscopy [41], differential thermal analysis (DTA) [42], nuclear magnetic resonance (NMR) [43] are used to determine the DC of polymers. Among these, Raman spectroscopy was found to be a highly efficient and reliable non-contact method [30,31]. Lempel *et al.* studied DC by using Raman spectroscopy to evaluate the influence of the energy of polymerization delivered on the composite material and the applied resin layer thickness on these properties by investigating the formation and bonding structure of bulk urethane dimethacrylate (UDMA) and triethylene glycol dimethacrylate (TEGDMA) as polymers of different porosity [30].

The reaction kinetics and the polymerization rate can be determined by fitting the data of DC and polymerization time with the Avrami model. The latter describes how materials transform from one phase to another (liquid to solid) at a constant temperature. It can precisely illustrate the kinetics of crystallization of polymers. The model is commonly utilized generally to study changes in the phase of materials and also to provide information on the nucleation density and growth process, which can be meaningful in analyses of materials [44,45]. Details will be given later, in section 4.1.

2.1.2. Gamma radiation-initiated polymerization

The main advantage of gamma radiation-initiated polymerization method is that the radicals are created directly into the monomer (Figue 3), therefore no initiator is required (pure, additive-free process). The synthesis can be done at any temperature, a large number of solvents can be used, the production time is short, and the prepared polymer can be used immediately. Due to the large penetration depth of ionizing radiation the polymer size and shape can be varied within a wide range, so the desired application production can be adapted to the area. The method is not selective, which is sometimes an advantage, sometimes a disadvantage [34].

Gamma-initiated precipitation polymerization technique has been successfully used in the past also for the production of monodisperse polymer microspheres and porous polymer. The prepared polymer in this method could be bulk or monodisperse [34].
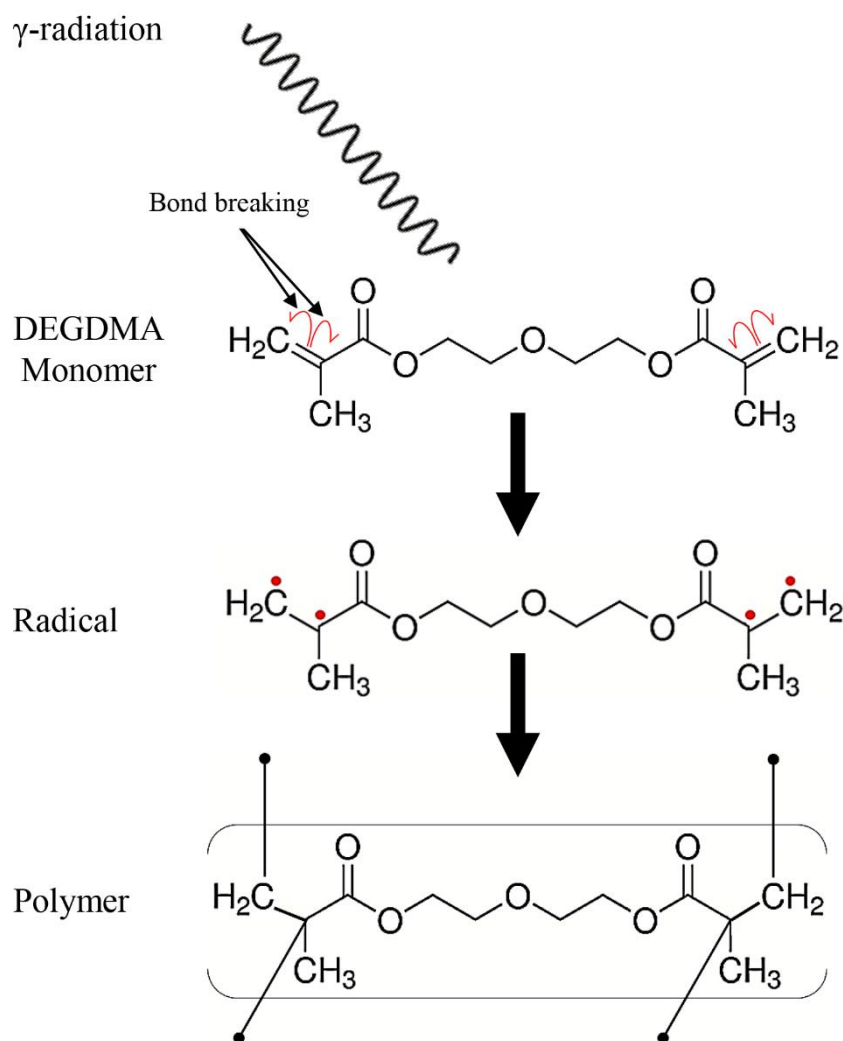
Figure 3: Diagram of gamma radiation-initiated polymerization.

Microspheres were made from DEGDMA monomer in the presence of various organic solvents [28,34,46,47]. The polymerization temperature, type of the monomer and solvent, irradiation dose and dose rate are parameters that affect the kinetics of polymerization and the properties of obtained products [46,47]. The condition for the production of DEGDMA microspheres is that the solubility parameter of the solvent used is almost the same as that of the monomer, and the viscosity of the solvent should be low. Large spheres (4.8 μm) can be produced with low viscosity solvents and longer irradiation times [47]. Alcohols do not promote the production of microspheres due to their solubility and viscosity [48].

The results obtained in the production of microspheres show the pore size can be changed with the irradiation temperature, type of the monomer, solvent and crosslinking compound, their concentration, and with dose and dose rate [29,34]. Grasselli *et al.* [34] synthesized monodisperse microspheres and porous polymers with epoxy functionality by radiation polymerization. The production of microbeads was also possible with less than 30% monomer concentration, while porous polymers were obtained with monomer concentrations between 30-50%. At higher concentrations, the obtained polymer was a bulk homopolymer. The effect of the monomer concentration, dose effect on the polymer structure were also investigated. It was found that when a 30 vol% monomer solution is irradiated with doses above 15 kGy (1 Gray (Gy) = 1 J/kg = 100 rad), the polymerization was complete. The effect of solvents was most pronounced: with alcohols like methanol, ethanol, 2-propanol and butanol – ("macroporous" solvents) samples with large pores were formed, while solvents such as acetone, ethyl acetate, tetrahydrofuran and ethyl propionate – ("microporous" solvents) monoliths with very small pore size were obtained.

2.1.3. Preparation of fluorescent polymeric microparticles

Nowadays, due to their wide applications area, polymeric micro- and nanoparticles are interesting topics for many researchers. Micro- and nanoparticle systems play a significant role in many applications like delivery systems for drugs, vaccines by uploading drugs into excipients of polymer to improve the influences of the drug or for the treatment of disease, here the regulator particle diameter is an important variable that can be effective of a loaded medication [1,2], aerosol research as tracking [3,4], biomedical diagnostic [25] and optical imaging [49].

Polymer micro- and nanoparticles are solid particles characterized by sizes ranging between 1-250 μm and 100-1000 nm, respectively [50]. The emulsion [27,51], dispersion

[26,52], suspension [53] and self-organized precipitation [54] polymerization methods can be used to prepare polymeric particles with micro or nano size. The size of particles depends on many factors, including the properties of the polymeric composition like viscosity, surface tension and preparation method [1]. Nevertheless, surfactant materials (surfactants are organic substances with hydrophobic (tail) and hydrophilic (head) groups, having either water-insoluble (or oil-soluble) and water-soluble components) are adding to the preparation composition which can control the size of particles by manipulating the characteristic surface tension of the mixture. The selection of appropriate surfactant material is based on the required size for the application [55].

On the other hand, incorporating organic dye in the polymer matrix opens chances for designing new and desired structures for multiple applications in the technology. It was demonstrated that fluorescent organic micro- and nanoparticles are powerful tools for various applications including life sciences (as biomarkers for biological imaging) [5–9], flow devices [10], biomedical fields [11]. In previous studies, conventional organic dyes or fluorescent proteins have been used for *in vivo* or *in vitro* imaging, but one of the main issues with them is the high photobleaching rate due to the solubility of the dye and because the specimen might be immersed or covered completely by the dye, thus long-term imaging is a challenge due to photodamage in the sample [12]. Photobleaching is the photochemical alteration of a dye or a fluorophore molecule that results in the molecule becoming nonfluorescent. This might be due to photolysis or other reactions, such as the bonding of excited fluorophores to surrounding molecules [56]. Uptake of a fluorescent dye into a host polymer microparticle is a promising approach to decrease the photobleaching problem that can also reduce the photodamage effect [13]. Emulsion polymerization is a form of radical polymerization that typically begins with water, monomer and surfactant emulsion which can be utilized to create fluorescent monodisperse polymeric particles [27,51]. Figure 4 shows fluorescent microparticles fabricated by emulsion polymerization method. The method relies on surfactant materials and stabilizers, as basic additives in the polymerization to (i) maintain the phase of the polymer in the composite solution; (ii) reduce the aggregation of product particles; (iii) prevent the adhesion into solution. Moreover, the yield of particles is influenced by the stabilizer and appropriate surfactant [26,27].
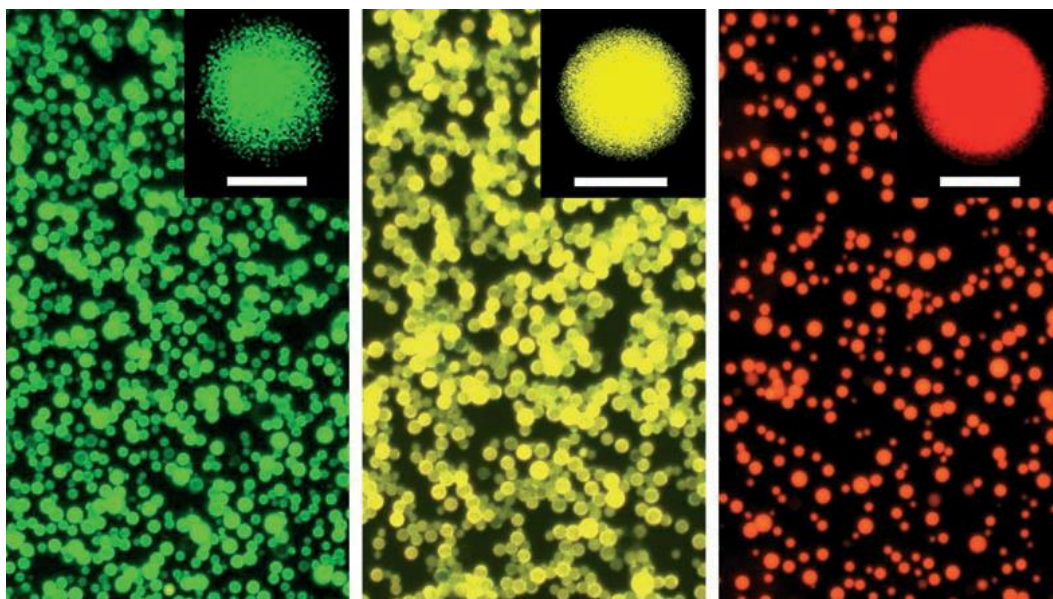
Figure 4: Fluorescence images of PS particles filled with green (left), yellow (center) and red CdTe dots (right). The insets show the confocal fluorescence images that correlate to them. The scale bars are 2 μm [57].

On the other hand, the challenge is how to create polymeric particles with a facile method or one step, without stabilizers, and with less/no surfactants. Therefore, the gamma precipitation polymerization is initiated without any initiator and stabilizer by selecting the appropriate combination of the compounds that allow creation of particles having a spherical shape and uniform size. In addition, other molecules can simply be incorporated into the polymer matrix by their addition to the monomer mixture [58].

In this part, we report on the preparation and characterization of fluorescent microparticles, formed of FITC dye dissolved into DEGDMA microparticles prepared during gamma radiation-initiated polymerization method. I characterized the fluorescent microparticles with different methods and tested their performance by Raman spectroscopy and SEM. To evaluate the emission of the fabricated FITC/DEGDMA microparticles, I built light-sheet fluorescent microscopy and utilized it in imaging of prepared fluorescent microparticles besides the photoluminescence measurement.

2.1.4. Polymeric SERS-active substrates

SERS effect is an increased Raman signal based on the interaction of electromagnetic fields of incident or scattered light with collective oscillations of free electrons in metal nanoparticles. Several different types of substrates have been developed and tested for SERS spectroscopy since the invention of SERS in 1974 [59]. SERS effect was observed on noble

metals like silver which is the most common element, followed by gold. Despite the fact that gold offers a lower overall SERS enhancement than silver, the former is especially desirable for biological and biomedical applications because of its long-term stability and biocompatibility, while the latter is particularly attractive due to its low cost. Today, SERS substrates that are frequently used in SERS applications include metal electrodes, island thin films, colloidal nanoparticles (NPs), and highly ordered nanostructures, made by techniques like self-assembling, lithography, and nanoimprint [59–63]. Figure 5 shows an example of SERS substrate utilizing nanosphere lithography [61]. It is worth noting that a typical SERS-active substrate for an application should (i) display Raman enhancement, (ii) be uniform throughout the whole surface, and (iii) exhibit excellent spectral stability and repeatability. Finding SERS active substrates that adequately meet these criteria is an interesting research topic for scientists nowadays.
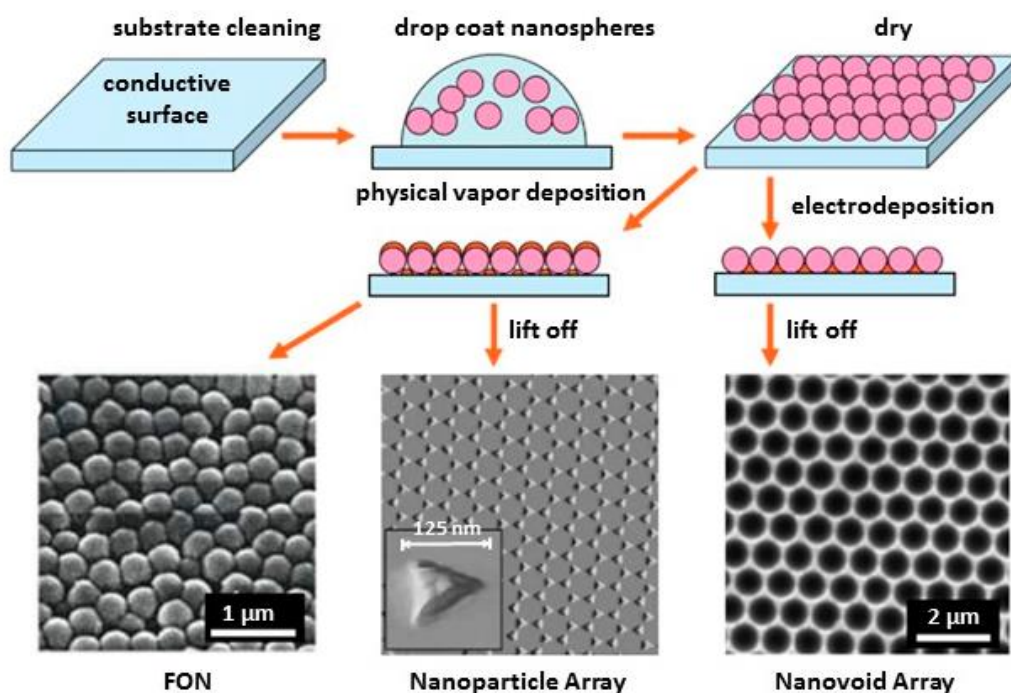

Figure 5: Diagram showing of the nanosphere lithography method, which is used to fabricate metal film over nanosphere (FON), periodic nanoparticle arrays, and nanovoid arrays [61].

Although the porous polymer materials have been extensively proven in many applications like separation or detection of biomolecules, *etc.* [64,65], their usage as polymeric SERS-active substrates for the detection of proteins has only lately become popular [66]. Wang *et al.* [67] recently developed monolithic poly(glycidyl methacrylate ethylene dimethacrylate) (poly(GMA-co-EDMA)) rods containing epoxide groups that react with aqueous solution of

ammonia to generate amine functionalities, allowing for the immobilization of silver nanoparticles in the rods. SERS tests with rhodamine 6G (R6G) performed with this substance revealed a statistically significant enhancement factor. The same monolith of poly(GMA-co-EDMA) was produced in a capillary tube and reacted with cysteamine to produce monoliths containing thiol functionalities, which were significant for the connection of gold nanoparticles with polymeric monoliths [68], SERS measurements of p-aminothiophenol (PATP) were performed on the prepared monolith composite and it demonstrated excellent sensitivity and high SERS enhancement [69]. Cao *et al.* created a polymeric planar SERS active layer by polymerizing glycidyl methacrylate-ethylene dimethacrylate (GMA-co-EDMA) that was reacted with cysteamine to functionalize the layer with gold nanoparticles. The SERS layer was used for sensing bacteria [21]. Figure 6 shows a scanning electron microscope image of a porous poly(GMA-co-EDMA) layer that has been functionalized with 40 nm AuNPs (left), in the schematic Figure (a, centre), E. coli bacteria are trapped on an AuNP/monolith substrate and their SERS spectra on 40 nm AuNP/monolith substrates functionalized with propanethiol (b, right), 3-mercaptopropionic acid (c, centre) and cysteamine are shown (d, right). Despite the monolithic polymers being fabricated as substrates to detect SERS effect and format them as capillary tubes or planar layers, they have shown good SERS signals as well. Investigations into the typical design of a SERS active substrate that presents the best characteristics remain the focus of researchers, particularly in the case of monodisperse microparticles.
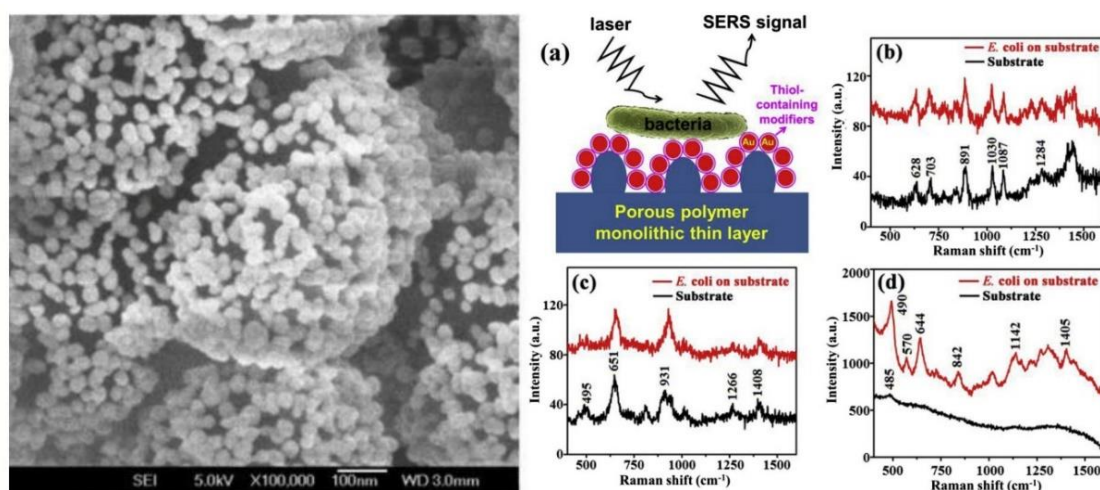

Figure 6: SEM image of porous poly(GMA-co-EDMA) layer functionalized with 40 nm AuNPs (left), a schematic diagram showing the cross-sectional view of bacteria captured on a modified AuNP/monolith substrate (a, centre), and the SERS spectra of E. coli bacterium on 40 nm AuNP/monolith substrate functionalized with propanethiol (b, right), 3-mercaptopropionic acid (c, centre), and cysteamine (d, right) [21].

In this thesis, we report on the preparation and characterization of a novel type of SERS active substrates, formed of AuNPs attached to poly(DEGDMA) microparticles prepared by gamma radiation-initiated polymerization method. To evaluate the performance of the fabricated composite, the aqueous solution of R6G was used as a Raman standard. The effect of the excitation wavelength on the SERS enhancement was investigated. Also, the stability of the resultant poly(DEGDMA)/AuNPs composite particles with time was evaluated. Moreover, the SERS performance of the developed substrate has also been tested in real conditions by detecting DNA strand-specific of the parasite Giardia lamblia (the β-giardin gene) as a promising biological application.

2.2. Microscopic and spectroscopic techniques

2.2.1. Photoluminescence

Photoluminescence (PL) involves the irradiation of the sample to be characterized with photons of energy greater than the band-gap energy of that material. The incident photons will create electron-hole pairs. When these electrons and holes recombine, this recombination energy will transform partly into non-radiative emission and partly into radiative emission. In other words, PL process involves three main steps: 1) Excitation: creation electron hole pair due to the absorption of a photon emitted by a laser source, xenon lamp, tungsten bulb, or other light source by exciting electron to higher energy level; 2) Relaxation: the excited pair relaxes towards quasi-thermal equilibrium distribution after thermalization; 3) Recombination: when the electron returns to its original ground state, the energy may be released in the form of a lower energy photon [70,71].

2.2.2. Light-sheet fluorescent microscopy

Over twenty years ago, light-sheet fluorescent microscopy (LSFM) has been an imaging method that has achieved superior development in imaging science [72,73]. The technique consists of the excitation part to illuminate the specimen with a thin light sheet and the detection part perpendicularly to the excitation side of the sample. Because the illumination and detection parts are organized at a right angle, it is possible to obtain a single plane image in (xy-axes) and move the specimen toward the detection path (z-axis), which allows for 3D imaging and even observing the growth of the specimen in biological samples. In addition, other advantages of the technique include low photobleaching, phototoxicity, and photodamage due to the low excitation power [74,75].

The first light-sheet imaging microscope technique was described in 1903 by an Austrian/Hungarian chemist Richard Zsigmondy and a German physicist Henry Siedentopf. The researchers wished to improve the optical microscope's resolution in order to image nanostructured materials such as colloidal gold. Abbe's study had previously proven that the resolution was limited and that one needed to utilize lenses with a large numerical aperture (NA) and short wavelengths of light in order to achieve higher resolution [74]. An employee with Zeiss at the time realized, to the benefit of Zsigmondy and Siedentopf, that a high contrast image is crucial to increasing the degree of visibility of any features. They illuminated the sample perpendicularly to the detection axis in their microscope and observed the scattered light by the gold nanoparticles, in so called Tyndall cones. During that time, since microscopic photography had not developed adequately, the studies were required to observe the phenomena by the researchers with their own eyes, and the light source, although strong, was changeable due to it involved focused sunlight. On the other hand, in all these determinations, different colors were observed for particles of various sizes and materials [74].

Scientists were able to use light-sheet microscopy to investigate small sizes within tissues or organs due to advancements in technology in the fields of microscopic cameras and semiconductor lasers in the late twentieth century. Voie *et al.* developed a light-sheet microscope, called Orthogonal Plane Fluorescence Optical Sectioning (OPFOS) to image the internal architecture of the guinea pig cochlea with high-resolution images. In this research, the lateral and axial resolutions of the images were 10 and 26 μm, respectively, within a 1.5-mm field of view [76]. Many LSFM systems use the same components: laser source, telescope as a beam expander, cylindrical lens, specimen chamber, illumination part being orthogonal to the direction of detection and specimen movement perpendicular to the light sheet plane (formed by the illumination and detection axes) to create a z-stack [77]. Huisken *et al.* published an article on Selective Plane Illumination Microscopy (SPIM) in 2004. The researchers developed SPIM to produce multidimensional sample images of up to a few millimeters in size, and they used the device to investigate and image *in vivo* the embryogenesis of the relatively opaque fruit fly (Drosophila melanogaster) [78].

Figure 7 shows the schematics of a light sheet fluorescence microscope with one side illumination. In the diagram, the laser beam is passed through the cylindrical (that will create the light sheet) lens before the excitation objective. Then the light sheet created by the cylindrical lens excites the specimen through an illuminating objective that reduces light aberrations. It is worth to mention that the cylindrical lens is a type of lens that concentrates

light into a line rather than a point, as a spherical lens would. After that, the scattered light is captured at the specimen by detecting objective. Since the illumination part is connected with a translational stage, multi-sheet images of the specimen can be recorded using the camera that with appropriate software post processing can create a 3D image of the scanned volume [77].
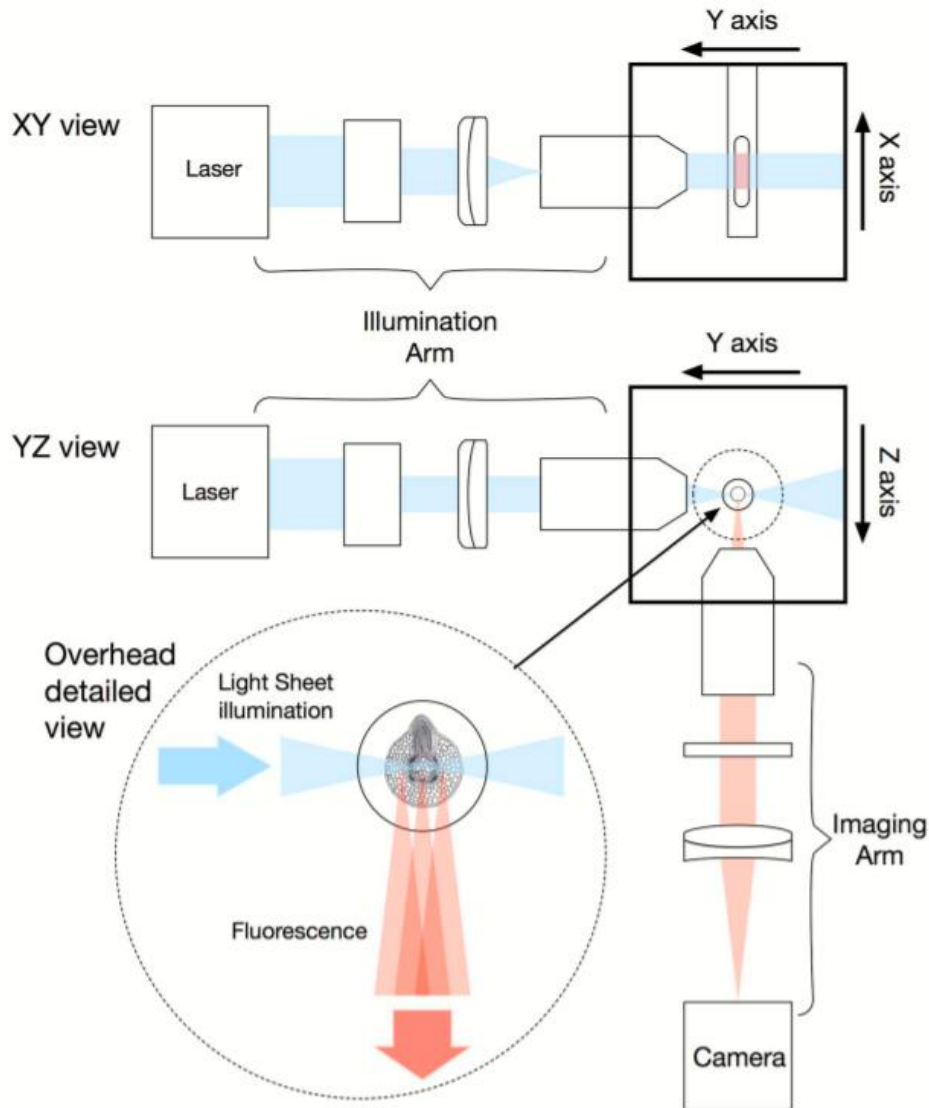

Figure 7: Light-sheet fluorescence microscope is formed using a cylindrical lens before the excitation objective and the orthogonal imaging arm. The XY plane view is shown in the top drawing, where the objective keeps the light focused on the sample. The YZ plane view, seen at the bottom, is where the objective completely concentrates light on the sample [74].

Another LSFM configuration to that shown in Figure 1 is adding a second illumination part on the opposite side to the first, this known as dual-sided illumination [72]. Advantages of this configuration are: (i) it reduces shadow artifacts; (ii) it provides a more intense beam; and (iii) it allows the illumination of a larger specimen. In contrast, the disadvantage is the difficult

alignment of both light sheets in three-dimensional space, which makes the optical focus not optimal [77].

The challenges and limitations like high cost, limited field of view and low resolution in the field of imaging related to traditional microscopy methods give the motivation to explore and investigate Light Sheet Fluorescence Microscopy (LSFM) technique for improving image measurement accuracy. LSFM, is based on the Selective Plane Illumination Microscopy (SPIM) system [79], is an optical technique that has been used to image specimens by monitoring the scattered light after the specimen is illuminated with an appropriate wavelength [74]. Here, it is worth mentioning that the cylindrical lens is a basic unit for forming the light sheet of the laser beam. In other words, the main feature of the cylindrical lens is to compress light in the direction perpendicular to this line, but it remains unchanged in the direction parallel to it based on the lens design.

Three-dimensional spatial resolution of the LSFM is controlled by the numerical apertures used for excitation and detection (NA_{exc} and NA_{det}, respectively). By taking into account the diffraction limit of wide-field microscopy, the lateral resolution ($R_{lateral}$) and the axial resolution (R_{axial}) are [80]:

$$R_{lateral} = \frac{\lambda_{em}}{2NA_{det}} \tag{1}$$

$$R_{axial} = \left(\frac{2NA_{exc}}{\lambda_{exc}} + \frac{n(1 - cos\theta_{det})}{\lambda_{em}} \right)^{-1} \tag{2}$$

The axial resolution corresponds to the illuminating light sheet's thickness, $\left(\frac{2NA_{exc}}{\lambda_{exc}} \right)$, and the axial resolution of the detection objective lens, $\left(\frac{\lambda_{em}}{n(1-cos\theta_{det})} \right)$, where λ_{em}, λ_{exc} are the emission and excitation wavelengths, respectively, n is the refractive index of the imaging buffer, and $\theta_{det} = sin^{-1}(NA_{det}/n)$ is the half-angle of light collection in the imaging buffer. Clearly, increasing NA_{exc} results in an increase of the axial resolution, which corresponds to a thinner light sheet [80].

2.2.3. Raman spectroscopy

Raman spectroscopy is an effective light scattering technique for the detection of characteristic vibrations of molecules, solids, liquids and gases. The technique can be used to

characterize the molecular structure and bonding configuration of materials by observing the frequency shift between the excitation photon and the photon scattered by the medium [81–83]. The method is based on the inelastic light scattering effect induced by the interaction between the incident photons and the building blocks of the medium. In 1928, the Raman scattering phenomenon was first noticed by Indian scientist Chandrasekhara Venkata Raman [84] and, in 1930, Raman got a Nobel Prize in physics for that discovery. Although the earlier applications of Raman spectroscopy in physics and chemistry were related to the investigation of vibrations and bonding structure of gases, liquids and solids [17], nowadays, Raman spectroscopy is utilized in vast range of applications such as in environmental protection, quality monitoring, temperature measurements, medical diagnostics, biology and nanomedicine [85,86].

Due to the weak scattering, the large intensity of the excitation light is one of the main requirements to observe a detectable Raman signal. The discovery of the laser in 1960 and its utilization in a Raman system [87,88], the development of imaging cameras and charge coupling devices (CCD) [89] and the possibility to prepare filters cutting out the light of the exciting laser [90] were significant factors to improve the conditions of the Raman technique. Then, the confocal Raman microscope gave a significant impact on the rapid development of high-resolution measurements and to obtain the surface distribution of a given compound through the generation of compositional maps or images of heterogeneous samples [91]. So molecular and Raman scattering it is necessary to know the fundamentals of molecular vibrations, what will be described in the next chapter.

2.2.3.1. Molecular vibrations

During the Raman scattering effect, the incident photon excites the characteristic vibrations of the medium: phonons in the case of crystals and molecular vibrations in the case of molecules. It is beneficial to review the theoretical background of molecular vibrations to understand the Raman scattering mechanism.

During the light-matter interaction, a photon can be absorbed by the molecule, and the energy of this absorbed photon can excite the molecule from a lower to a higher state, as illustrated in Figure 8. Vibration, rotation and translation are three types of molecular motions that can be excited by the incident photon. In the molecules, the atoms are connected by chemical bonds and the vibration indicates a periodic change in the characteristics of bonds (bond length and/or angle) [92].
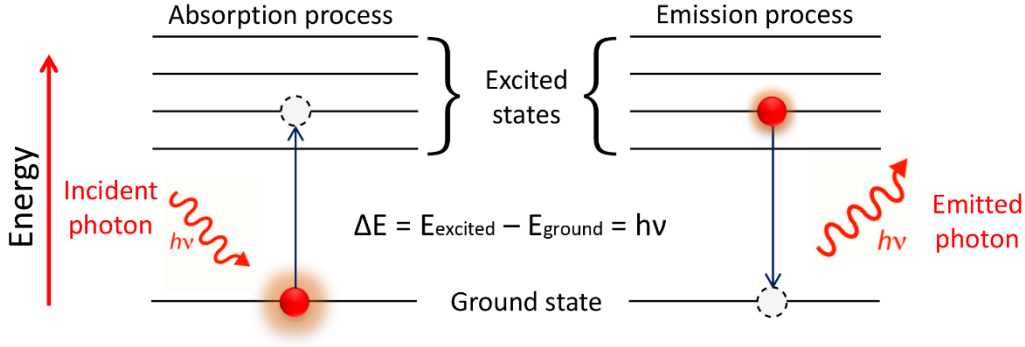
Figure 8: Simple diagram shows a light-matter interaction process.

2.2.3.2. Raman scattering

Many interactions can occur between light and matter. Depending on the internal structure of the medium and energy of the incident photon, the light can be reflected, absorbed, and scattered. As a consequence of the interaction with light, the electrons within the molecule are disturbed periodically by the electromagnetic field of frequency v_i, which leads to the formation of an induced electric dipole moment. In other words, a dipole moment will be induced by the oscillating electrical field in a molecule [92].

There are two types of scattering processes: elastic and inelastic. In the first type, the emitted radiation has the same frequency as the incident light, and it is also called Rayleigh or Mie-Tyndall scattering. During the inelastic scattering, the scattered light has a frequency being different from that of the incident wave. This process is known as Raman and Brillouin scattering [17,93].

The difference in the frequency between the incident and the scattered light is known as Raman shift by the following [92]:

$$\Delta v(cm^{-1}) = (v_{incident} - v_{scattered}) \tag{3}$$

It should be noted that, in general, this frequency difference does not depend on the frequency of the incident photon, so for a given peak, the same Raman shift will be observed when exciting the molecule with photons of different energy.

During the light-matter interaction, the medium is affected by a time-varying electric field $E = \varepsilon_0 \bar{x} E_0 \cos(2\pi v_i)$ of incident radiation which induces an electric dipole moment (P) [94]:

$$P = \alpha_{ij}E = \varepsilon_0 \bar{x}_{ij}E = \varepsilon_0 \bar{x}_{ij}E_0 \cos(2\pi v_i t) \tag{4}$$

19

where α_{ij} is the polarizability of the molecule, ε_0 is the dielectric constant of vacuum, and $\bar{x}_{ij}$ is the susceptibility, which is a tensor quantity characteristic for the medium. As we will see, the polarizability is a significant quantity for the Raman activity of materials [92,95].

The vibration with a frequency of v_{vib} will change the displacement (x) of the atoms as

$$x = x_0 \cos(v_{vib}t) \tag{5}$$

If the polarizability is not constant during the vibrations of the molecule and, assuming the displacement (x) is small, it can be written for the normal coordinates of vibration in the form of Taylor series:

$$\alpha = \alpha_0 + \frac{\partial \alpha}{\partial x_{x=0}} x + \cdots \tag{6}$$

Combining Eq. (6) with Eq. (5) gives

$$\alpha = \alpha_0 + \frac{\partial \alpha}{\partial x_{x=0}} x_0 \cos(v_{vib}t) \tag{7}$$

By substituting Eq. (7) into Eq. (4) we get:

$$P = \left[\alpha_0 + \frac{\partial \alpha}{\partial x_{x=0}} x_0 \cos(v_{vib}t)\right] E_0 \cos(2\pi v_i t)$$

$$P = \left[\alpha_0 E_0 \cos(2\pi v_i t) + E_0 \frac{\partial \alpha}{\partial x_{x=0}} x_0 \cos(v_{vib}t) \cos(2\pi v_i t)\right] \tag{8}$$

Equation (8) can be rearranged using the trigonometric identity:

$$\cos a \cos b = \frac{1}{2}\{\cos(a + b) + \cos(a - b)\}$$

$$P = \left[\underbrace{\alpha_0 E_0 \cos(2\pi v_i t)}_{Rayleigh} + \frac{x_0 E_0}{2} \frac{\partial \alpha}{\partial x_{x=0}} \left[\cos 2\pi \underbrace{(v_i - v_{vib})}_{\substack{Stokes \\ Raman}} t + \cos 2\pi \underbrace{(v_i + v_{vib})}_{\substack{Anti-Stokes \\ Raman}} t\right]\right] \tag{9}$$

According to Eq. (9), it is clear that the scattered light spectrum of a molecule consists of three main distinct terms. The first term represents "Rayleigh scattering" which corresponds to the frequency of incident light v_i, hence the induced dipole has the frequency of the excited light. The latter two terms, where the frequency changes, are related to the Raman scattering. The

lower frequency $v_i - v_{vib}$ is known as a **Stokes shift,** which means the light is scattered with lower energy that is equal to the energy of the molecular vibration. The term with additional energy, $v_i + v_{vib}$ known as an **anti-Stokes shift** means the scattered radiation has gained energy equal to the energy of a molecular vibration when the molecule participated in the process of excitation to a vibrational state [17,94]. The anti-Stokes process requires the molecule to already be in an excited vibrational state the energy of which can be transferred to the scattered photon. Figure 9 shows the diagrammatic representation of Rayleigh scattering Stokes Raman and anti-Stokes Raman scattering.
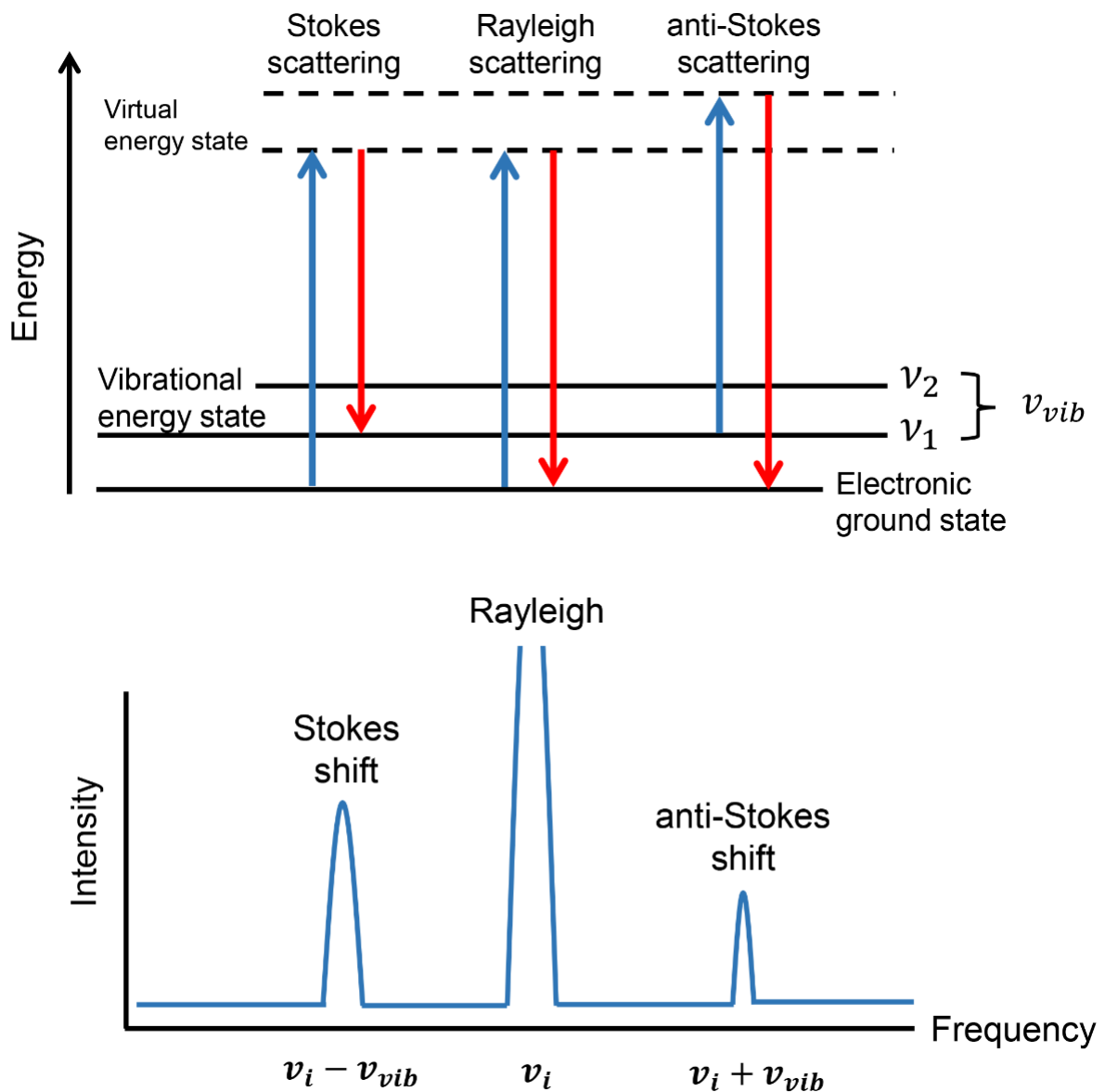

Figure 9: Diagram of Rayleigh scattering, Stokes Raman and anti-Stokes Raman scattering.

Actually, the molecules tend to be stable at room temperature. Therefore the vast majority of an assemble will be in the ground state, and only a minority will be in the excited vibrational state. Therefore, at low temperatures, the Stokes Raman scattering will dominate over anti-Stokes scattering. On the other hand, the molecules distribution in the vibrational ground state and excited state according to Boltzmann's equation determines the ratio of the Stokes intensity to the anti-Stokes [96]:

$$\frac{I_{Stokes}}{I_{anti-Stokes}} = \left(\frac{v_i - v_{vib}}{v_i + v_{vib}}\right)^4 e^{\frac{\hbar v_i}{k_B T}} \tag{10}$$

According to Eq. (9), the essential criterion for observing the Raman scattering is

$$\frac{\partial \alpha}{\partial x_{x=0}} \neq 0 \tag{11}$$

Eq. (11), means the derivative of the molecule's polarizability must be non-zero at the equilibrium position of the vibration, and this is a mandatory condition for the Stokes or anti-Stokes Raman scattering to occur [97].
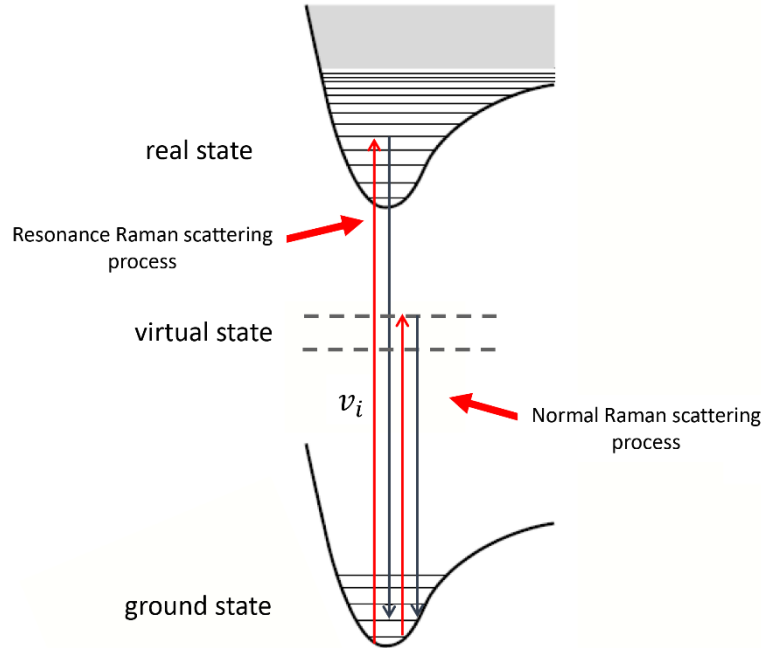

Figure 10: Diagram of Resonance Raman scattering and normal Raman process.

Quantum theory provides a complete description of the Raman scattering phenomenon by studying the transition between energy state levels; the quantum theory allows us to appraise intensities of Raman bands. This approach is assumed the incident light wave as time-dependent perturbation in the scattered medium [17,98].

On another hand, Resonance Raman scattering occurs when the energy of the excitation is equal or close to an electronic transition of the molecule or solid because otherwise, Raman scattering involves a virtual state. But in the real level, it can be resonant Raman scattering. Figure 10 shows the scheme of the Resonance Raman scattering process. An increase in Raman scattering of specific vibrational modes occurs when a molecule is excited electronically. Electronically excited vibrational modes with changed bond length exhibit increased polarizability and hence Raman intensity [14]. The normal Raman scattering process is also mentioned in Figure 10.

2.2.4. Surface-enhanced Raman spectroscopy

Surface-enhanced Raman spectroscopy or surface-enhanced Raman scattering (SERS) is a spectroscopy tool used to enhance the intensity of Raman scattering light by adsorbing the analyte molecules on rough metal surfaces or nanoparticles as SERS active substrates [17,20,99,100]. During SERS the low Raman scattered light is amplified through its interaction with localized plasmons – collective oscillations of the free electrons in the metal.

Fleischmann *et al.* [59] first identified the SERS phenomenon in 1974, when they discovered unexpectedly enhanced Raman signals while researching pyridine adsorbed on a roughened silver electrode [60]. In 1977, Fleischmann's observations were confirmed by two independent research groups, Jeanmaire and van Duyne [101] and Albrecht and Creighton [102]. According to their experiments, the phenomenon was caused by the creation of strong electrochemical electromagnetic fields or by the formation of molecular-metal complexes at the metal surface. Later, Moskovits [103,104] suggested that the large enhanced Raman signal is due to the optical excitation of the collective oscillations of electrons on the metallic surface. Although many enhancement mechanisms were suggested in the early days of SERS, only two of them are accepted nowadays: the electromagnetic (EM) and the chemical enhancement (CE) mechanisms [20,105–107].

The CE mechanism incorporates the intrinsic characteristics of the adsorbate and the new properties are resulting from the formation of adsorbate-metal complexes at the substrate leading to the alteration of the polarizability of the molecule [108]. In other words, a chemical bond is formed between the molecule and the metal surface during the chemical enhancement process. Consequently, there is a charge transfer between them, resulting in the formation of new electron states [14]. The main contributions of the CE mechanism is due to the resonant Raman effect involving these new states, which results in a Raman amplification of about four

orders of magnitude [108]. Further information on this topic can be found for example in references [107,109].

During EM mechanism, the incident and/or scattered light interacts with the metal surface, where localized surface plasmons (LSP) are excited. LSP are collective charge (electron) oscillations at the metallic surface, the frequency of which is affected by the material, size, shape, *etc*. of the metal. In the case of resonant excitation (*e.g.* the frequency of the external EM field is equal to the LSP frequency) a significant enhancement of the Raman signal by the LSP can be experienced near the surface. SERS enhancement occurs only with plasmon oscillations perpendicular to the metal surface. In-plane plasmons do not contribute to the SERS enhancement. In other words, roughened surfaces or arrangements of nanoparticles show excellent performance in SERS measurements [14].

SERS is a phenomenon related to plasmonics, therefore it is worthwhile to review this field in more detail. It's beneficial to study the optical properties of metals to get a better understanding of the concept of plasmonic surface amplification. Discussion in the frames of the Drude model is sufficiently precise for metals suitable to SERS, such as gold and silver, as well as for wavelength ranges relevant for Raman measurements, including the visible and the near-infrared regions [107,110].

The optical properties of bulk materials are determined by the frequency-dependent (ω) dielectric function. The dielectric function is connected to the refractive index by the relation $n(\omega) = \sqrt{\varepsilon(\omega)}$, and it is a complex quantity for most substances [111]. The Drude model considers delocalized electrons moving in the lattice of metals as an ideal gas (since they are charged particles, plasma) and gives the following relation for the dielectric function [107]:

$$\varepsilon(\omega) = \varepsilon_\infty \left(1 - \frac{\omega_p^2}{(\omega^2 + i\tau_0\omega)} \right) \tag{12}$$

where ε_∞ is the dielectric constant at infinitely high frequency, τ_0 is the damping factor, that corresponds to the collision rate of free electrons with ions and impurities and ω_P included in the equation is:

$$\omega_P = \sqrt{\frac{ne^2}{m\varepsilon_0\varepsilon_\infty}}, \tag{13}$$

the frequency of the charge density change of the free electron plasma, *i.e.*, the plasma frequency. In the equation, *e* is the charge of the electron, *n* is the number of free electrons per unit volume, and *m* is their mass, ε_0 is the dielectric constant of the vacuum.

If the incident photon has a frequency greater than the plasmon frequency (as is usually the case with UV photons), the light will be transmitted or absorbed by the interband electrons and there are no free electron oscillations occur. On the other hand, photons with a frequency less than that of the plasmon frequency will induce oscillations and will be reflected by the metal. Since the electric field of the incident light cannot penetrate the bulk of the metal, this will excite plasmons at the metal surface, affecting just a small fraction of the free electrons [112].

The real and imaginary parts of $\varepsilon(\omega)$ Eq. (12) are:

$$\text{Re}[\varepsilon(\omega)] = \varepsilon_\infty \left(1 - \frac{\omega_p^2}{(\omega^2 + \tau_0^2)} \right) \tag{14}$$

and

$$\text{Im}[\varepsilon(\omega)] = \frac{\varepsilon_\infty \omega_p^2 \tau_0}{\omega(\omega^2 + \tau_0^2)} \tag{15}$$

Considering the relation $\tau_0 \ll \omega$, the plasmon frequency can be determined in the case $Re[\varepsilon(\omega)] \approx 0$. It can also be seen from the above relations that for $\omega < \omega_p$ we have $Re[\varepsilon(\omega)] < 0$. Furthermore, if ω is not too small, the value of $Im[\varepsilon(\omega)]$ will have small values. If these two conditions are met – the real part of the dielectric function is negative (and its magnitude is large) and the imaginary part is small – plasmon resonance can occur in the bulk material.

The oscillations of conductive electrons in metals at a metal-dielectric interface caused by an incident electromagnetic field is called plasmon resonance, which results in intense electromagnetic fields near the metal's surface. This phenomenon can be classified into two categories: propagating surface plasmon resonance (SPR) on metal layers and localized surface plasmon resonance (LSPR) on metallic nanoparticles [113,114].

In Figure 11a, charge waves propagate in the XY plane around the interface area for a few tens to hundreds of microns and decay evanescently in the z-direction [115]. These are referred to as surface plasmon polaritons (SPP). Polariton is a term that refers to a hybrid excitation that happens when a surface plasmon couples with a photon, resulting in charge waves traveling along the surface [116]. While, in Figure 11b, light interacts with particles much smaller than the incident wavelength in the case of localized surface plasmons. This results in the formation

of a plasmon that oscillates at a frequency known as the LSPR locally around the nanoparticle [115,117].
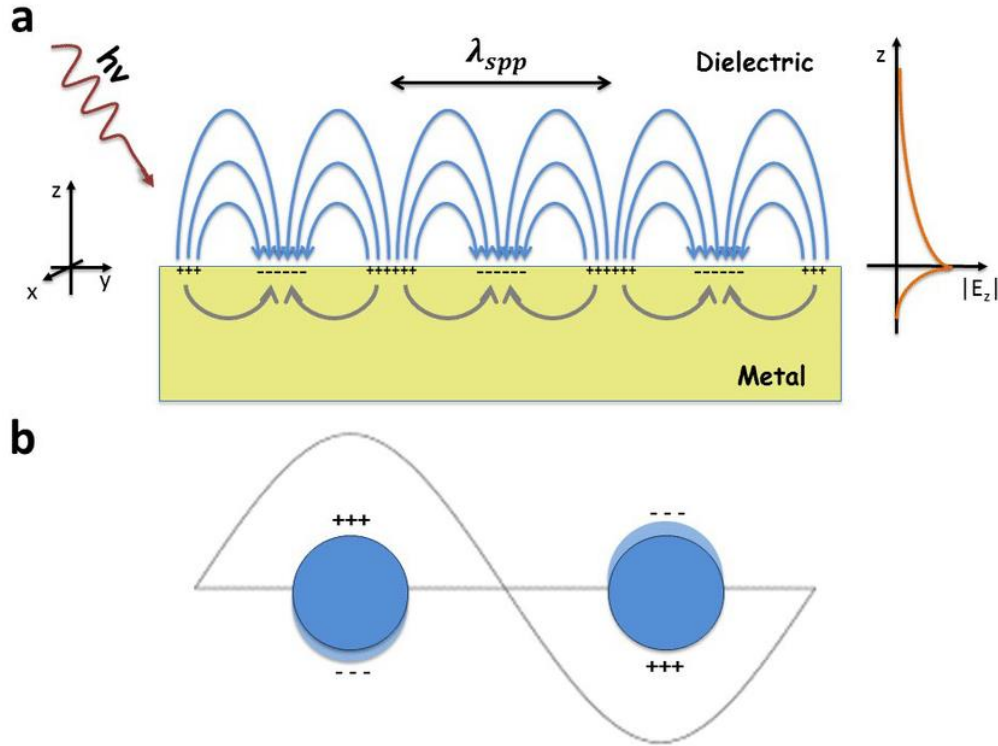

Figure 11: Mechanisms of surface plasmon polariton (a) and localized surface plasmon resonance (b) [115].

When an external electromagnetic field is applied on a flat and infinite surface it excites electrons in a very thin layer (a few or a few tens of nanometres) near the surface. A surface electromagnetic wave can form between a metal surface that can be described by a dielectric function $\varepsilon_{metal}(\omega)$ and an insulating surrounding medium with a dielectric function $\varepsilon_{diel}(\omega)$. This wave is a longitudinal charge density wave (as opposed to transverse light waves). A charge wave, as previously stated, can be coupled to an electromagnetic wave generating a surface plasmon wave. The dispersion curve of SPP excitation can be given as [118]:

$$K_{SPP} = \frac{w}{c}\sqrt{\frac{\varepsilon_{metal}(\omega)\varepsilon_{diel}(\omega)}{\varepsilon_{metal}(\omega)+\varepsilon_{diel}(\omega)}} \tag{16}$$

where K_{SPP} is the wave vector of light necessary to excite a SPP for a given interface, the value below the square root is greater than the value for metals, so the wave vector of the plasmon wave is greater than the wave travelling in free space. Then, surface plasmons form only under special conditions.

The electronic excitation of SPP is seen in Eq. (16) depends on both the metal layer properties and on its surrounding environment. This relationship makes excitation of surface plasmon resonance an excellent tool for sensing, as it allows for the detection of changes in the dielectric properties of the metal layer's local environment through changes in the resonance frequency (or coupling angle) of surface plasmon polariton. This is the fundamental premise of the SPR sensing technique. So, the resonance frequency of SPR (ω_{SPR}) is depending on the plasmon frequency (ω_p) of the metal and the dielectric function (ε_{diel}) of the environment medium which given as [118]:

$$\omega_{SPR} = \frac{\omega_p}{\sqrt{1 + \varepsilon_{diel}}} \tag{17}$$

In contrast to SPR, LSPR has a resonance frequency (ω_{LSPR}) that is determined by the metal's plasmon frequency and the dielectric function of the local surrounding medium [119]:

$$\omega_{LSPR} = \frac{\omega_p}{\sqrt{1 + 2\varepsilon_{diel}}}. \tag{18}$$

As it is seen from the eqs. (17) and (18) the factor 2 is an only difference, which results in a significant change in the resonance frequencies of the same metal-dielectric depending on the geometrical structure. In other words, when an incident photon interacts with a metallic surface, it influences the resonance frequency of the SPR or LSPR as a function of the dielectric constant, which results in generating the SERS effect, the latter depending on particular physical and chemical conditions.

SERS enhancement factor (EF) is a fundamental characteristic of the SERS effect. It is affected by many factors, including the wavelength, polarization and the angle of incidence of the excitation light; characteristics of the SERS support: material, geometry, morphology; refractive index of the medium adjacent to the SERS support; characteristics of the sample used for the experiment: concentration and coverage on the SERS support's surface, actual distance from the SERS surface.

While being so important, it is not easy te determine the SERS EF precisely, especially because it is difficult to measure the pure SERS and normal Raman contributions for the same amount of sample. To characterize the SERS EF, three main quantities were introduced, the single molecule enhancement factor (SMEF), the normalized enhancement factor (NEF), and the analytical enhancement factor (AEF) [107,120].

The use of these enhancement factors depends on the characteristics of the SERS experiment. The SMEF is used for very low concentration samples in single-molecule measurements and can be determined according to the following equation [120]:

$$\text{SMEF} = \frac{I_{SERS}^{SM}}{I_{RS}^{SM}} \tag{19}$$

where I_{SERS}^{SM} is the SERS intensity of the molecule under the study and I_{RS}^{SM} is the normal Raman intensity of the molecule for the same sample.

In many SERS applications and investigations, the SMEF distribution on the substrate, even if it has a high value, is unimportant because it's dealing with average signals of SERS. Finding the appropriate enhancement factors method is essential which can be utilized to compare the SERS enhancements across different substrates. Therefore, NEF is the common expression of normalized SERS enhancement is defined by the equation [120]:

$$\text{NEF} = \left(\frac{N_{RS}}{N_{SERS}}\right) \times \left(\frac{I_{SERS}}{I_{RS}}\right) \tag{20}$$

where N_{SERS} is the number of molecules involved in the SERS process, which is usually equal to the number of molecules absorbed on the surface, N_{RS} is the number of molecules involved in the conventional Raman process, which is equal to the number of molecules in the excited volume. One of the disadvantages of this approach is that in most measurements in bulk liquids, the normal Raman signal of the molecules present in the bulk volume is also added to the SERS signal of those adsorbed on the surface.

In the case of using a solution as a test sample, the number of molecules absorbed on the surface is orders of magnitude lower than the number of molecules involved in normal Raman scattering. Therefore, the analytical enhancement factor (AEF) can be given as follows [120–122]:

$$\text{AEF} = \left(\frac{C_{RS}}{C_{SERS}}\right) \times \left(\frac{I_{SERS}}{I_{RS}}\right) \tag{21}$$

where I_{SERS} and I_{RS} represent the Raman intensities of the analyte molecule at the same wavenumber in SERS and normal Raman spectrum, respectively, and C_{SERS} and C_{RS} are the concentrations of the analyte molecule under SERS and normal Raman conditions, respectively.

In brief, the surface enhancement depends on the SERS experimental conditions, specifically the metallic substrate, the analyte target, and the excitation wavelength. Apart from having

different dielectric properties, Ag has a higher enhancement factor than Au in the 400–600 nm excitation field, but, Au becomes equivalent to Ag at wavelengths greater than 600 nm [107].

3. Materials and methods

This chapter is divided into four sections: materials, preparation of polymeric structures by gamma radiation-initiated polymerization, preparation of poly(DEGDMA) microparticles decorated with gold nanoparticles and characterization systems. The first section shows the list of main compounds and solvents that were used in the study. The second section describes the different sample preparations by gamma radiation-induced polymerization method to form different polymeric structures, including microparticles and fluorescent microparticles. The third part explains the protocol that was used to attach gold nanoparticles to poly(DEGDMA) microspheres to create SERS substrate for DNA detection. The final part deals with the characterization systems used in my research.

3.1. Materials

In this work, diethylene glycol dimethacrylate (DEGDMA) monomer, fluorescein isothiocyanate isomer-I (FITC) and rhodamine 6G (R6G) dyes were purchased from the Sigma-Aldrich and used as received, without any further purification. The chemical structures of the monomer and the dyes are shown in Figure 12.
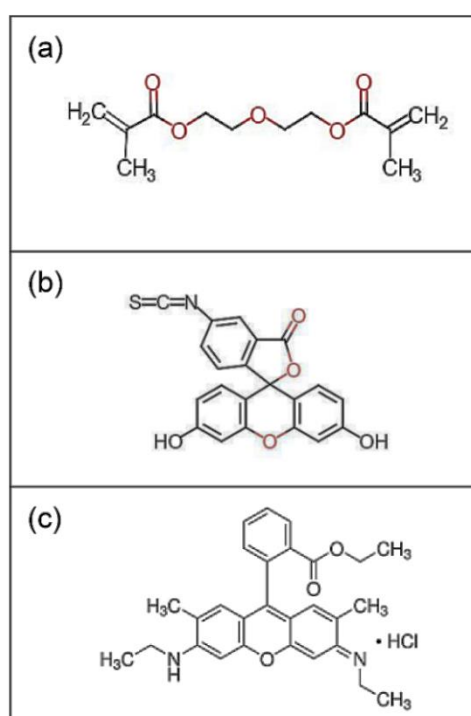

Figure 12: Chemical structure of (a) DEGDMA monomer, (b) FITC dye, and (c) R6G dye. DEGDMA has a linear formula: $C_{12}H_{18}O_5$, molecular weight: 242.27 g/mol, and refractive index: 1.458; FITC has a linear formula: $C_{21}H_{11}NO_5S$ and molecular weight: 389.04 g/mol; and R6G has a linear formula: $C_{28}H_{31}N_2O_3Cl$ and molecular weight: 479.01 g/mol.

Cystamine dihydrochloride (CDHC), sodium hydroxide (NaOH), tris(2-carboxyethyl)phosphine hydrochloride (TCEP.HCl), 6-mercapto-1-hexanol (MCH), colloidal gold nanoparticles (AuNPs) with a 40 nm diameter, deoxyribonucleic acid (DNA), pH test strips, ethyl propionate, methanol, ethanol, 2-propanol, ethyl acetate, acetone, and distilled water were purchased from Sigma Aldrich. The chemical materials and solvents were used as received.

3.2. Preparation of polymeric structures by gamma radiation-initiated polymerization

During my experiments, a Cobalt-60 (^{60}Co) γ-source with typical energies of 1.27 MeV and 16 kGy/h dose rate was used to irradiate all samples.

Firstly, DEGDMA monomer and methanol, ethanol, 2-propanol, ethyl acetate, acetone, and ethyl propionate solvents were used as structural materials. For the sample preparation, deoxygenated solutions of 30 vol% DEGDMA in different solvents were placed in plastic bags, sealed under nitrogen and irradiated with γ-source with doses between 1 and 40 kGy. The obtained samples were washed three times with the corresponding solvent to remove the non-reacted monomers. Then, they were dried at 50°C for 2 weeks before Raman and other measurements.

Polymer microparticles were prepared by gamma radiation-induced polymerization technique (Figure 13a). The DEGDMA monomer was dissolved in ethyl propionate at different concentrations and irradiated with different doses (Table 1), in order to study the dependence of the particle size on the monomer concentration and dose. The mixtures of different compositions were prepared in 2 ml vials, following the procedure described earlier.

Figure 13b shows polymer microparticles with embedded fluorescent dye were also prepared by gamma radiation-induced polymerization technique. A particular concentration of DEGDMA monomer was dissolved with ethyl propionate, a FITC in acetone solvent was added to the mixture as a highly fluorescent organic dye. To avoid contamination from the surroundings, the sample preparation procedures were carried out in a MBraun UNIlab Glovebox under a nitrogen atmosphere. Then the polymeric microparticles of FITC/DEGDMA were fabricated. 0, 5, 10, 15, and 20 vol% concentrations of FITC dye dissolved into acetone were dissolved with a fixed 5 vol% DEGDMA (Table 2). These samples were prepared as homogeneous solutions by using ethyl propionate solvent and placed in 2 ml vials.
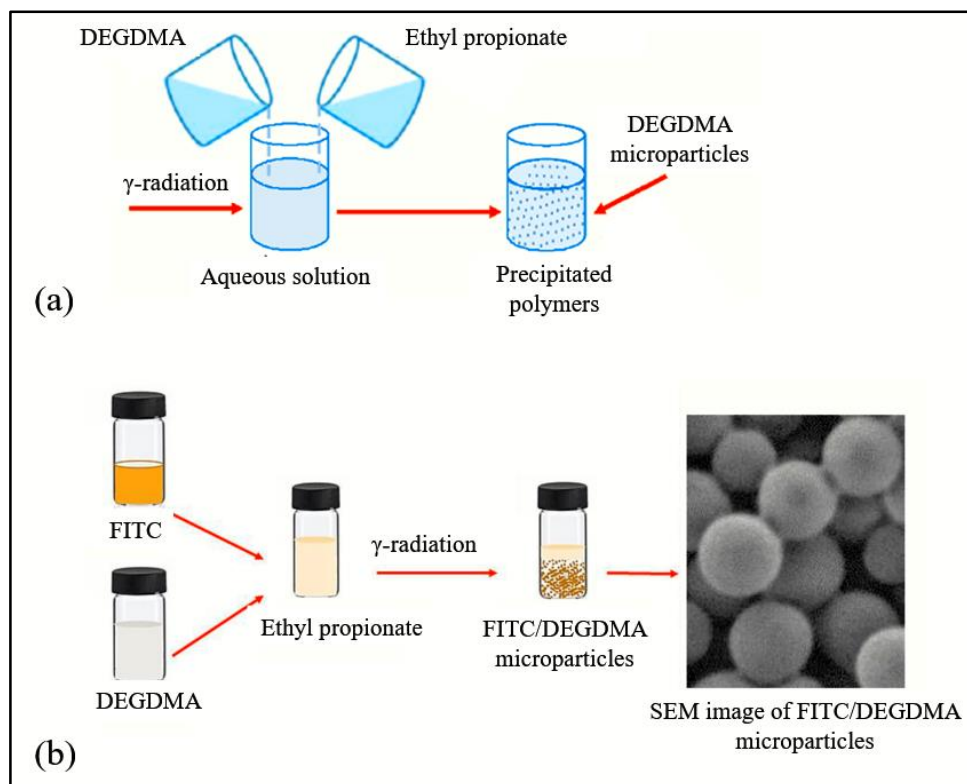
Figure 13: Diagram of preparation poly(DEGDMA) monodisperse microparticles by gamma radiation-initiated polymerization (a) without FITC dye and (b) with FITC dye.

Table 1: Different concentrations of DEGDMA dissolved in ethyl propionate at different irradiation doses to prepare polymeric particles.

Sample No.	DEGDMA concentration (vol%)	Ethyl propionate (vol%)	Dose (kGy)
a1	1	99	4
a2	1	99	7
a3	1	99	10
a4	1	99	15
b1	5	95	4
b2	5	95	7
b3	5	95	10
b4	5	95	15
c1	10	90	4
c2	10	90	7
c3	10	90	10
c4	10	90	15

Table 2: Different concentrations of FITC with 5 vol% DEGDMA dissolved in ethyl propionate at 10 kGy irradiation dose to prepare fluorescent polymeric microparticles.

Sample No.	FITC concentration (vol%)	Ethyl propionate (vol%)
S1	0	95
S2	5	90
S3	10	85
S4	15	80
S5	20	75

3.3. Preparation of poly(DEGDMA) microparticles decorated with gold nanoparticles

For the decoration with gold nanoparticles, polymeric microparticles were fabricated as described above. Then, the preparation continued with steps of attaching AuNPs to poly(DEGDMA) microparticles. This procedure is based on binding the gold nanoparticles to the polymer surface by thiol bonds, and consists of the following steps:

A. Fabrication of thiol-functionalized polymeric microparticles

To attach thiol groups to poly(DEGDMA) microparticles, we adopted a protocol used by Cao *et al.* [21]. The approach consists of two parts (see Figure 14): mixing 1.0 mol/L CDHC and 2.0 mol/L aqueous NaOH, and to react it with poly(DEGDMA) microparticles for 2 h at room temperature. Then, the microparticles were washed with distilled water several times to neutralize the pH. Subsequently, to liberate the free thiol groups, the microparticles were reacted with a 0.25 mol/L TCEP.HCl solution for 2 h at room temperature then washed with distilled water.

B. Combination of polymeric microparticles with gold nanoparticles (AuNPs)

Before the attachment of AuNPs to poly(DEGDMA) microparticles, a concentrated fraction of 40 nm AuNP colloid was separated by using an Eppendorf centrifuge with 12,000 rpm for 10 min. Then, 200 µl of concentrated AuNPs with size of 40 nm were added to 8 µl poly(DEGDMA) microparticles suspension and left for 3 h at room temperature, then washed to extract the unattached AuNPs. This step was repeated 3 times in order to maximize the number of AuNPs attached to poly(DEGDMA) microparticles. Figure 14 illustrates the schematic structure of polymeric microparticles decorated with AuNPs.
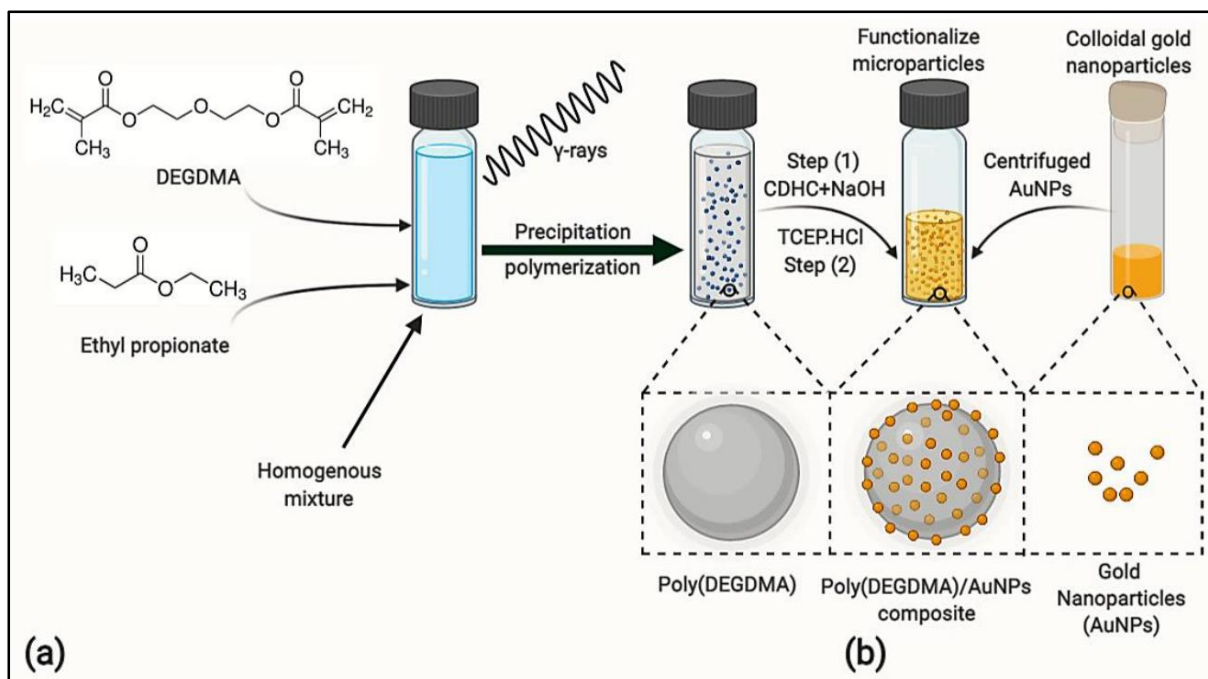
Figure 14: Preparation routine of poly(DEGDMA) microparticles by gamma radiation-initiated polymerization (a) without AuNPs and (b) with AuNPs. [CDHC ≡ cystamine dihydrochloride, NaOH ≡ sodium hydroxide, and TCEP.HCl ≡ tris(2-carboxyethyl)phosphine hydrochloride]. [T3]

C. Sample preparation for SERS detection of DNA

The synthesized poly(DEGDMA)/AuNPs composite was used to investigate DNA. Here we utilized DNA functionalization protocols as tested in previous work [123]. The purpose is to immobilize DNA on the gold surface in order to enhance the DNA Raman signal and this can be realized by creating a thiol group between DNA and the AuNPs surface. The protocol consists of the following main steps: 1) overnight immobilization of probe-DNA from a 1 µmol/L solution; 2) 30 min treatment with 6-mercapto-1-hexanol (MCH) after probe immobilization to reduce nonspecific binding of DNA on the gold surface; 3) 2 h binding of target-DNA from a 1 µmol/L solution. This protocol allowed to achieve a limit of detection of around 5 nmol/L for this target-DNA with a localized surface plasmon resonance sensor [124]. The base sequences of the probe-DNA and target-DNA: (from 5′ to 3′): probe-DNA: CGTACATCTTCTTCCTTTTT-[ThiC6]; target-DNA: AGGAAGAAGATGTACGACCA.

3.4. Sample characterization

3.4.1. Scanning electron microscopy

Scanning electron microscopy (SEM) is a versatile method for 2D and 3D characterization of the morphology of materials down to the nanometer level. SEM is one of the main

instruments for the study of the size, size distribution and shape of micro- and nanoparticles. During a SEM measurement, an electron beam is scanned over the sample to investigate its surface morphology. The scattered electrons from the sample are captured by detectors to create an image of the sample. The advantage of SEM is that it provides an image with high magnification and better resolution compared to the optical microscope [125,126].

In this work, SEM studies were performed to evaluate the morphology of prepared DEGDMA microparticles, fluorescent DEGDMA microparticles, poly(DEGDMA)/AuNPs composite and to characterize the particle size and size distribution. The SEM measurements were performed at the Institute for Solid State Physics and Optics of Wigner Research Centre for Physics (Budapest, Hungary) by using a Tescan MIRA3 scanning electron microscope (Figure 15). Imaging was performed with 1-5 kV electron energies to avoid charging and damaging the samples. The SEM images were analyzed with the ImageJ software.
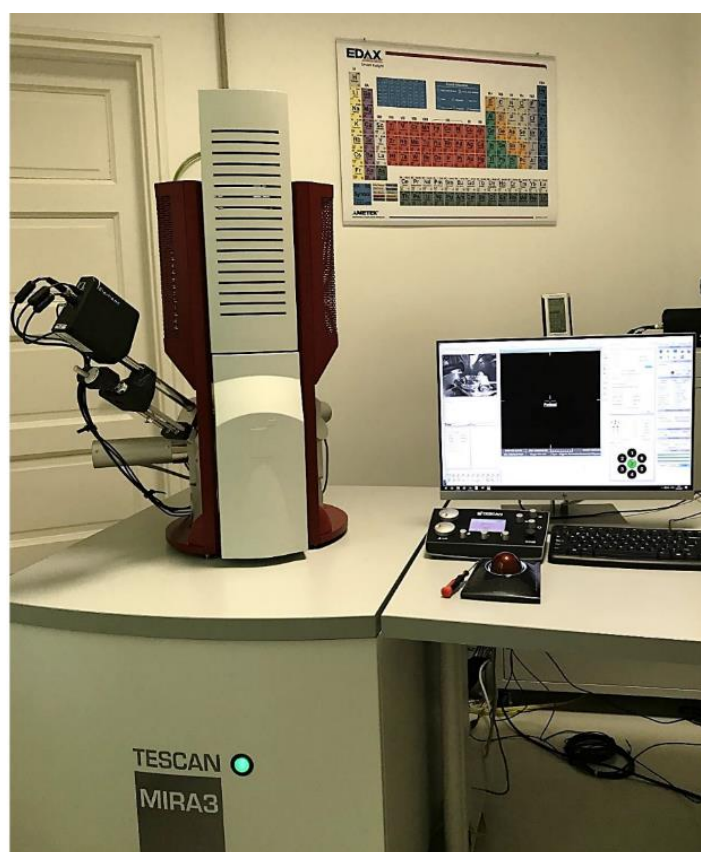

Figure 15: The Tescan MIRA3 scanning electron microscope.

3.4.2. Raman spectroscopy

In this work, I used two instruments for Raman and SERS measurements on my samples: a Renishaw 1000 Raman spectrometer integrated with a Leica DM/LM microscope (Figure 16a)

and a Renishaw inVia Raman system integrated with a Leica DM2700 microscope (Figure 16b). The two devices are similar, with the latter being essentially an improved version of the former, with motorized mirror control and higher sensitivity and higher resolution detectors.
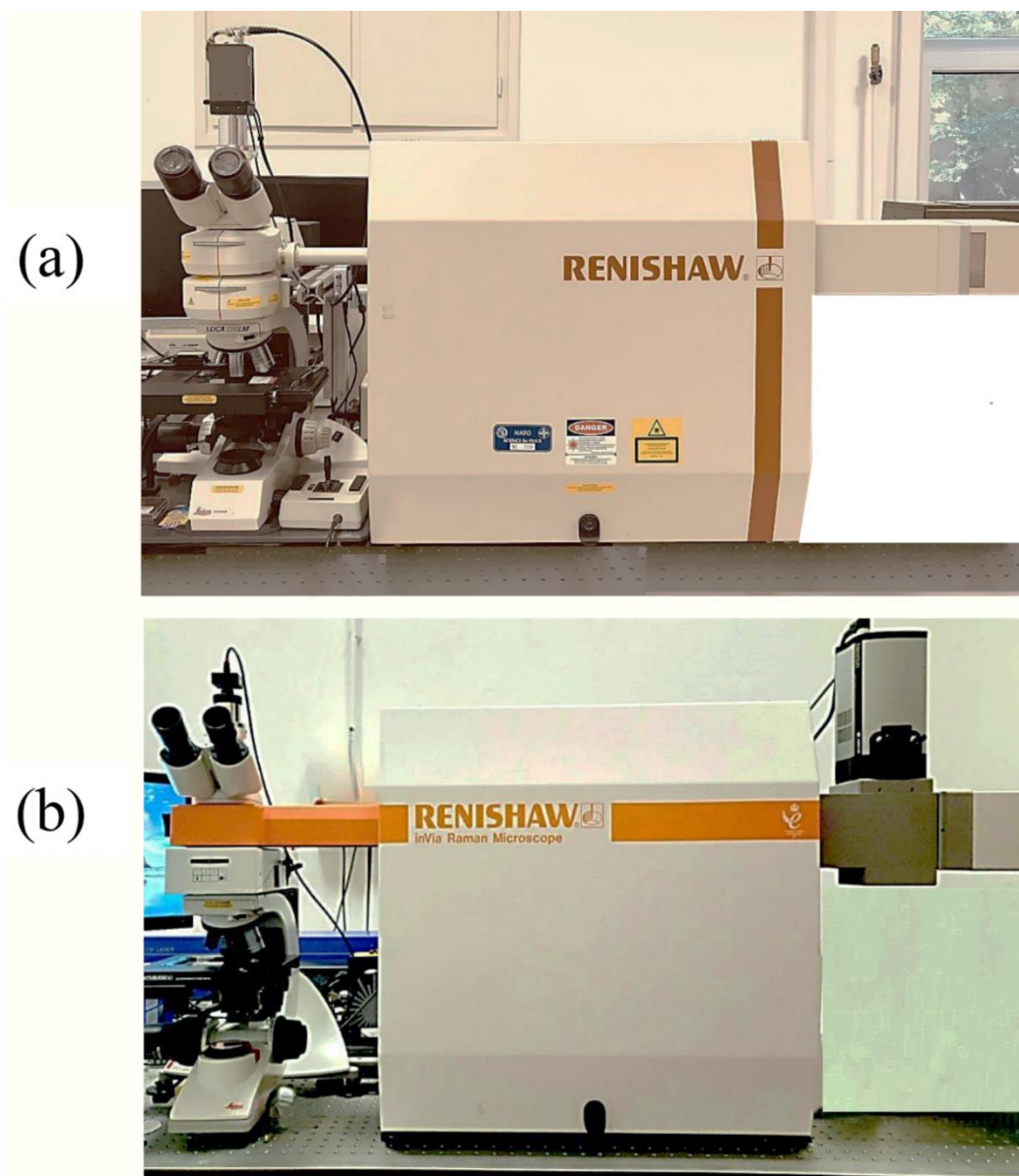

Figure 16: The (a) Renishaw 1000 and (b) Renishaw inVia micro-Raman spectrometers used for the Raman measurements.

A schematic layout of the Renishaw 1000 micro-Raman spectrometer, with labeled individual components, is shown in Figure 17.

The instrument measures the Raman spectrum in backscattering geometry. The movement of the sample under the objective lens of the microscope is performed with a motorized XYZ stage.
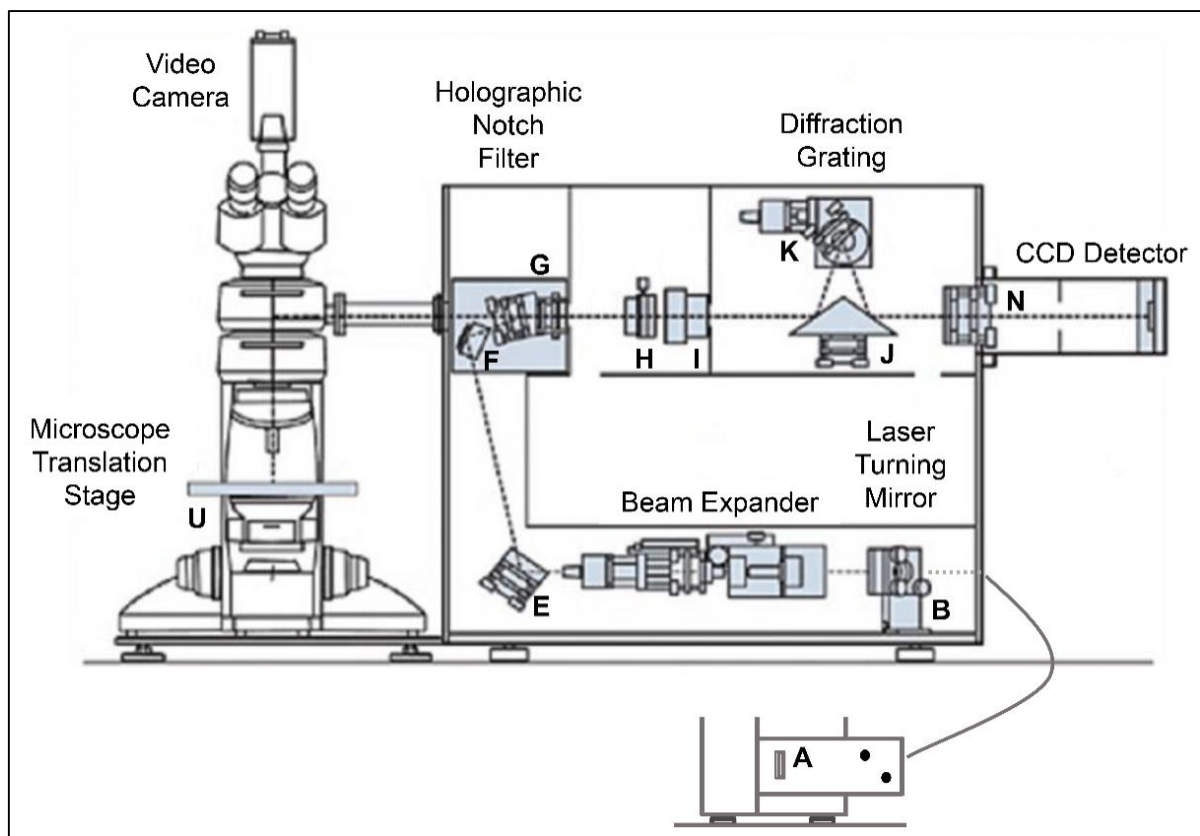
Figure 17: Schematic layout of the Renishaw 1000 micro-Raman spectrometer [127].

The main parameters for the Renishaw 1000 and Renishaw inVia systems are summarized in Table 3. The spectra are displayed by the appropriate versions of the Renishaw WIRE software running on the computers connected to the devices. The Raman measurements of the prepared materials were performed with the 785 nm excitation.

Table 3: Comparison of the main parameters of the Raman devices used for the measurements.

Feature	Renishaw 1000	Renishaw inVia
Excitation wavelength, nm	785 and 488	532, 633, and 785
Detector	576 x 20 pixel CCD	1024 x 256 pixel CCD
Microscope objective lenses	5x, 20x, 50x, 100x	5x, 20x, 50x, 100x
Automatic sample movement resolution, μm	0.2 in the XY direction	0.1 in the XY direction 0.02 in the Z direction
Optical grating density, 1/mm	1200	1200, 1800, 2400, 3000
Maximum achievable spectral resolution, cm^{-1}	1.5	0.3

Raman spectroscopic measurements on the obtained bulk and microparticle DEGDMA samples were performed at room temperature by using a Renishaw 1000 micro-Raman spectrometer attached to a Leica DL-LM microscope. A 785 nm diode laser with 20 mW maximum output power was used as an excitation source. The spot size was ~1 μm, while the laser power was 8 mW on the sample surface. The spectra were recorded with 1.5 cm^{-1} spectral resolution. While the SERS measurements of DNA were carried out on poly(DEGDMA)/AuNPs composite sample using a Renishaw InVia Raman spectrometer at a laser wavelength of 785 nm. Spectra were collected within one run and using 5 s acquisition time.

All recorded Raman and SERS spectra were processed by using the OriginPro 2018 software. First, a baseline correction has been performed by polynomial fitting. This was followed by fitting the Raman bands with a set of Gaussian and/or Lorentzian peaks.

In order to facilitate the assignment of the Raman bands of DEGDMA, the theoretical description of the Raman peaks was also studied using the calculated vibrational frequencies and their Raman activities for two methacrylate models. The density functional theory (DFT) method was used for simulations. DFT calculations of the Raman active modes of DEGDMA allowed us to identify the structural characteristics inside the generated model's designated area of interest. The computational part consists of geometry optimization and subsequent calculations of the Raman lines of monomer and polymer states of methacrylate models with the Gaussian-09 program package [128]. The self-consistent DFT field method with the hybrid B3LYP functional consisting of a linear combination of the pure corrected exchange functional by Becke [129] and the three-parameter gradient-corrected correlation functional by Lee *et al.* [130] was used for calculations. The triple zeta valence (TZV) Pople 6-311++G(d,p) basis set with the diffuse and polarization functions was used for C, O, and H atoms [131].

3.4.3. Photoluminescence spectroscopy

Photoluminescence (PL) is an optical phenomenon related to light emission from any kind of matter after absorption of a photon of wavelength λ1. The absorbed photon excites an electron, which decays to a lower energy excited electronic state, and then emits light of wavelength λ2, as it radiatively decays to its ground electronic state. The wavelength of emission, λ2, is usually longer than the excitation wavelength (i.e., the emitted photon has lower energy) [132,133].

In my work, I measured PL spectra to characterize the intrinsic luminescent properties of the fabricated optical material. The measurements were performed using Horiba Jobin Yvon 3-22 Fluorolog fluorimeter with a 450 W Xenon lamp excitation source. Figure 18a,b shows the PL spectrometer and optical layout of the PL system that was used in the research, respectively. PL emission spectra of the prepared luminescent polymeric microparticles structures were investigated in the 400-900 nm range, with the excitation wavelength 400-500 nm range using 0.1 s integration time. The excitation and emission slits were set to 5 nm. All PL spectra were recorded at room temperature.
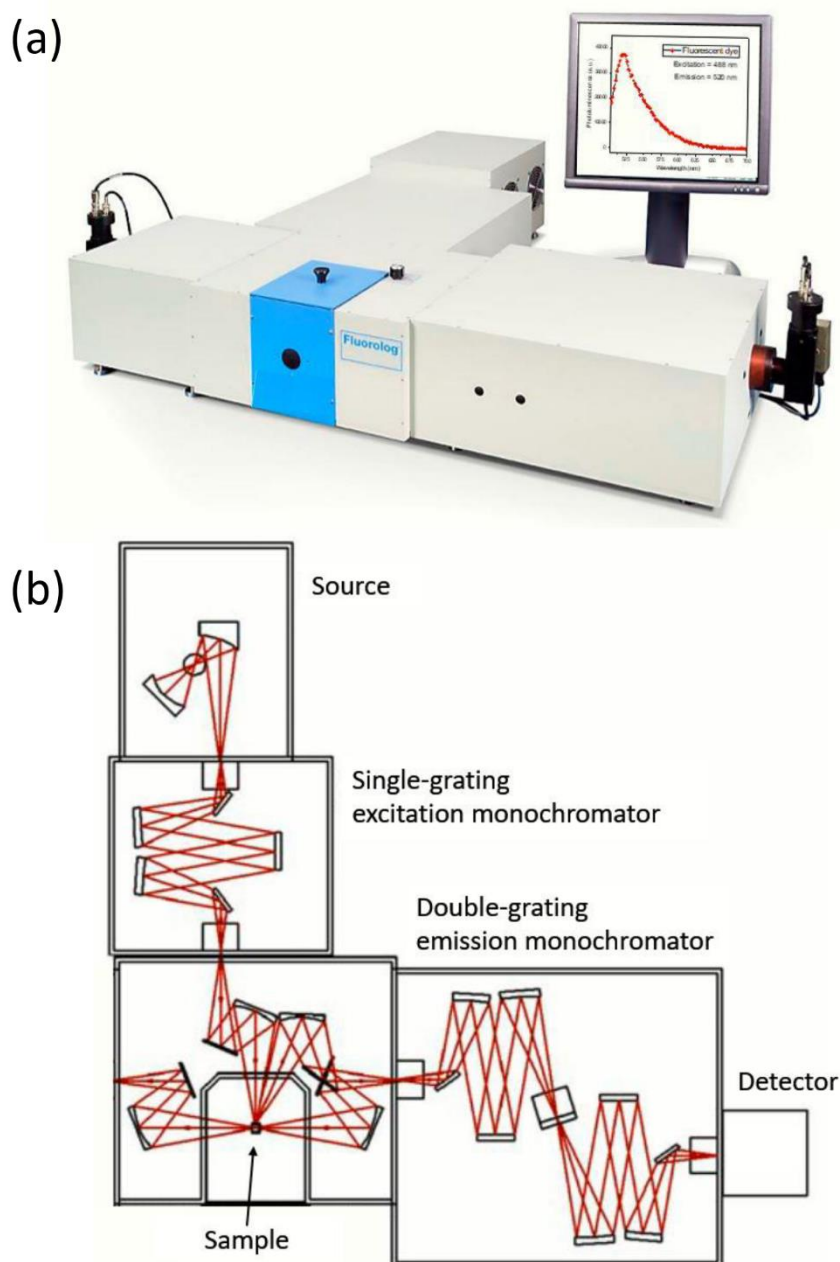
Figure 18: The (a) PL spectrometer and (b) optical layout of the Horiba Jobin Yvon 3-22 Fluorolog system.

3.4.4. Light-sheet fluorescent microscopy

In this dissertation, light-sheet fluorescent microscopy (LSFM) for imaging the luminescent microparticles, based on the SPIM system [79] was designed, built, and used by me to image standard fluorescent microparticles firstly then for the prepared particles in this work by their fluorescent emission. Figure 19 shows the LSFM system that was designed and constructed in the study [see **Appendix A**].
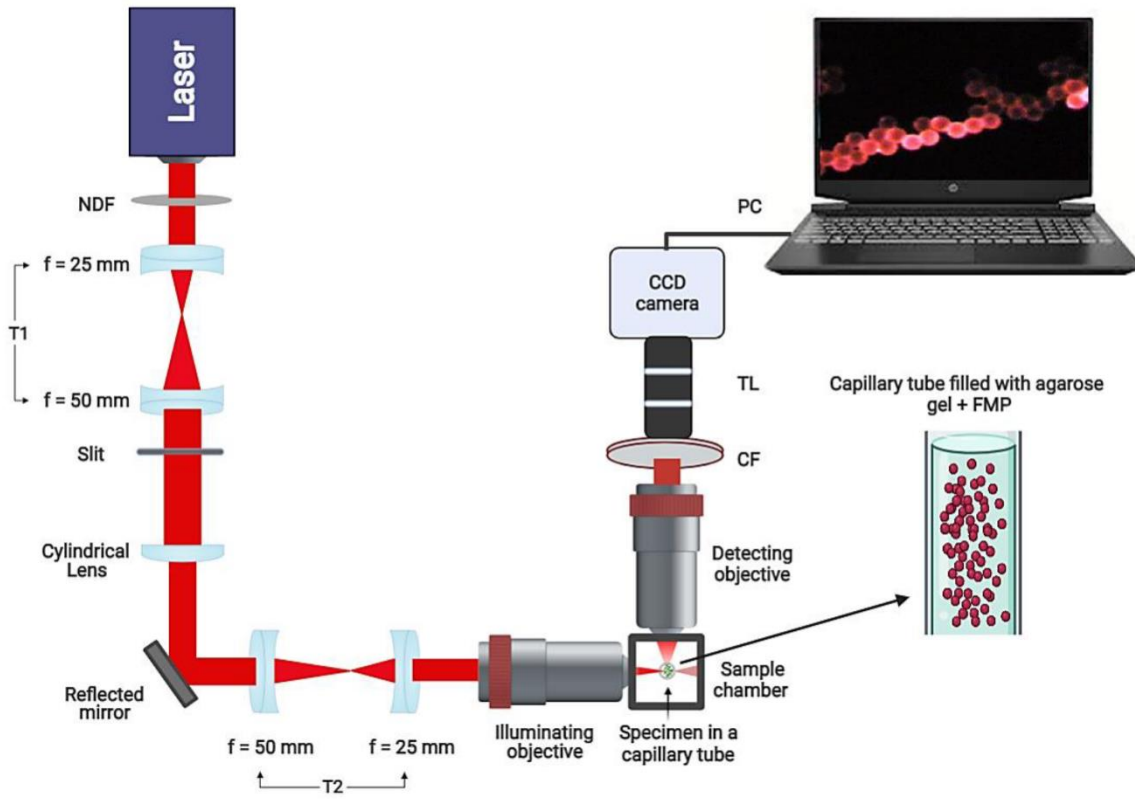

Figure 19: Schematics of the experimental LSFM system built and used for my experiments. NDF – neutral density filter, CF – color filter, TL– tube lens, T1, T2– first and second telescope, respectively.

As shown in Figure 19, the LSFM system can be summarized in four main parts:

A. Illumination part

This part consists of Gaussian mode laser. Three different wavelengths are available for illumination at 488, 532, and 633 nm with a maximum output powers of 65, 45, and 109 mW, respectively. These lasers can be used separately to excite the sample. Neutral density filter (NDF) is used to reduce the intensity of the laser beam. The collimated beam is passed through two achromatic doublet lenses with focal lengths of f1=25 and f2=50 mm, respectively. These are lenses of the first telescope (T1) which is used to increase the diameter of the laser beam in order to provide uniform illumination of the sheet. The central part of the expanded beam is

cropped in one direction by an adjustable rectangular mechanical slit before entering the cylindrical lens that creates the light sheet. Figure 20 shows the diagram of a cylindrical lens. The sheet is reflected by a mirror (M1), then passes into the second telescope (T2) to retrieve the laser beam to its original diameter. Then, the light sheet is narrowed down by an Olympus UMPLFLN 10X /0.3 water dipping objective lens to illuminate a small portion of the specimen in the focal plane.
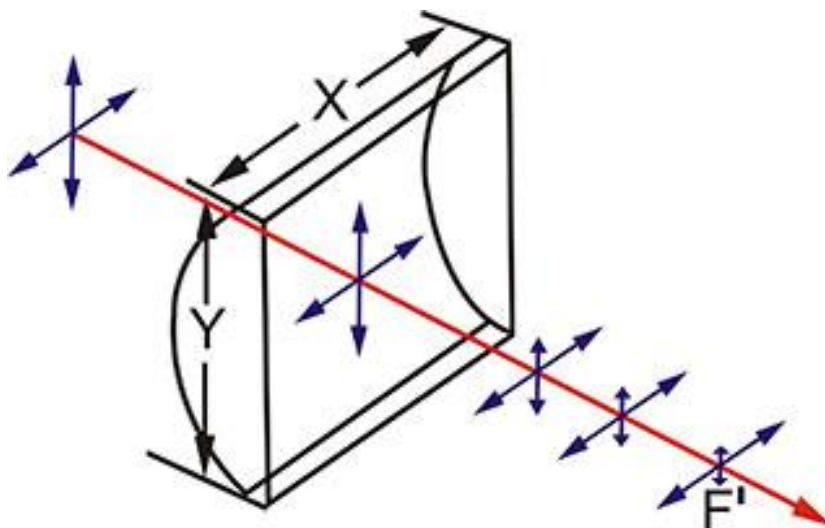

Figure 20: Diagram of a cylindrical lens.

B. Detection part

The detection part is like that of a traditional microscope. In brief, it consists of an objective lens, a color filter with a holder for selecting the detection wavelength, a tube lens, a shutter instrument, and a charge coupled device (CCD) camera as a detector. The emission color filter cuts the excitation light and allows the fluorescence signal emitted by the sample to transmit. A primary fluorescent image formed via the set of lenses behind the emission filter can be detected on the CCD camera, which is controlled by a computer.

In my research, I utilized air-/water dipping-objective lenses (Leica 50X /0.4 air lens and Olympus UMPLFLN 20X /0.5 water dipping objective lens). Based on Eq. (37) and Eq. (38), the lateral and axial resolutions of the system are 0.5 and 0.7 μm, respectively. For the fluorescein isothiocyanate isomer-I (FITC) dye a 500 nm long-pass filter was used with 488 nm excitation. While for imaging fluorescent polystyrene (FPS) microparticles a 650 nm long-pass filter was utilized with 633 nm excitation. A monochrome QImaging camera, type 01-QIC-F-M-12-C, (www.qimaging.com) with 1392x1040 pixel resolution, 4.65 x 4.65 μm pixel size, and 10 fps frame rate was utilized for the detection.

C. Specimen part

In my experiments, the illumination and detection parts were fixed. However, three-dimensional stacks of images were acquired by moving the sample along the detection side's optical axis and across the focal plane of the illumination. This was realized by placing the samples on a 4D-translation stage providing precise motion control. The Picard-Industries 4D-translation stage has a compact 4 axis motor assembly allowing to move the sample along four-dimensional (X, Y, Z, R) axes (R means the rotation of the sample around the vertical axis). The samples were placed in a small cylinder or a glass capillary tube filled with agarose gel to prevent them from moving. The transparent agarose gel allows for three-dimensional images to be captured from large sample volumes. The gel is composed of 1% agarose [0.4 g of pure agarose is dissolved into 100 ml of distilled water and placed in the oven for 2-4 mins until the solution becoming clear and transparent] in a medium that is appropriate for the specimen and the experimental circumstances.

A sample chamber can be designed and manufactured according to the objective lenses, in order to provide orthogonal placement of the two objective lenses. In my research, the chamber is a plastic cube (it is made in our lab using a 3D printing machine). It is designed with two perpendicular windows, one used for the illumination and the other for the detection objective lens. For water-dipping objective lenses, a rubber ring can be inserted between the lens and the window which enables the lens to be fixed into the chamber without any water leakage. The main benefit of the water dipping lens configuration is to decrease the relative refraction of the extra glass surfaces in the optical path of the detecting system.

The main components of the built LSFM system are described in Table 4. Images of the self-made LSFM parts are presented in **Appendix B**.

I have made a specific sample holder for the LSFM system, it was designed using Fusion 360 3D CAD software. Figure 21a,b shows a flow-through-sample holder that I made in the lab. The holder is in the shape of a cylindrical channel with an inner diameter of about 0.9 mm, and it is supported by two windows that are covered by glass coverslips on each side. The purpose of this holder is to detect, image, and measure flowing microparticles [T1, T2] and some biological cells like red blood cells (RBCs).

Table 4: Main components used in the building of the LSFM system.

| Description	Manufacturer	Quantity
Adjustable mechanical slit	ThorLabs	1
Water dipping objective lens for illumination (10x/0.3)	Olympus	1
Water dipping objective lens for illumination (20x/0.5)	Olympus	1
Fluorescent microscopy filter with different color and bandpass (FWHM 30-50 nm) and a longpass that block the illumination well	ThorLabs	1 to each illumination source
USB-4D-Stage its compact 4 axis motor assembly, sample positioning arm, 5 M3 screws to bolt the sample positioning arm onto the motor assembly	Picard-Industries	1
Chamber Holder– Aluminum	Self Made	1
Sample Chamber – Plastic	Self Made	1
QImaging Camera, (FAST 1394), COOLD MANO 12 BIT, type 01-QIC-F-M-12-C	Qimaging www.qimaging.com	1
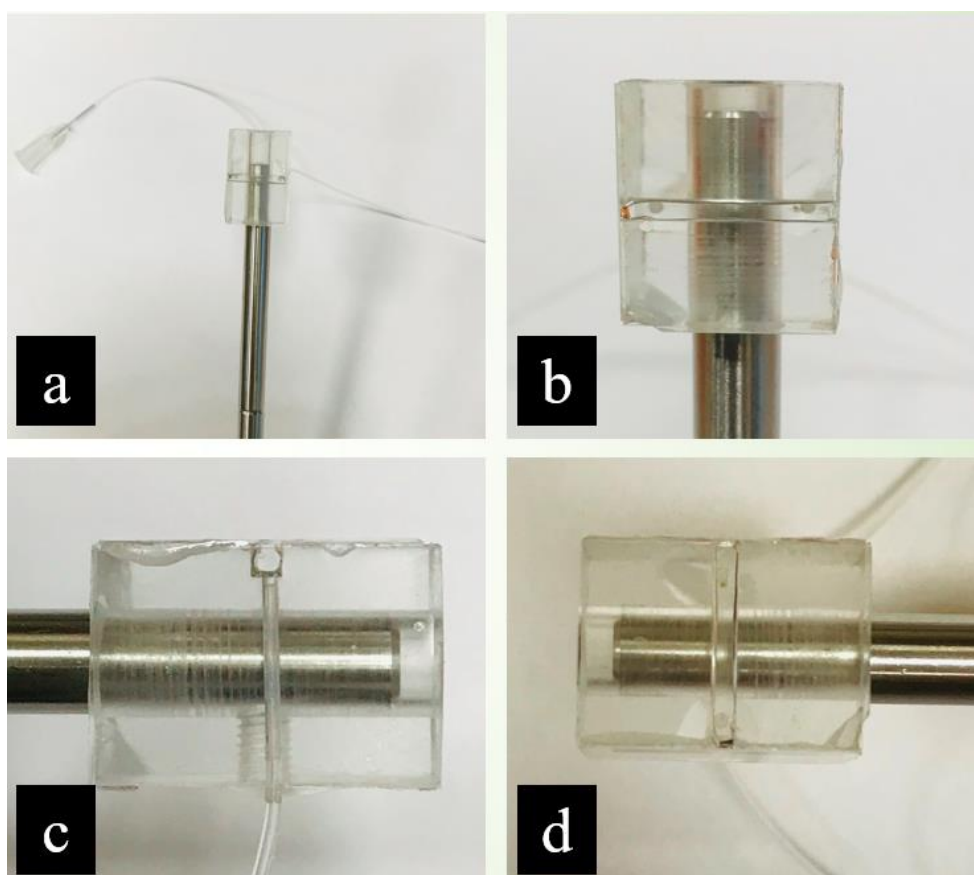
Figure 21: Flow-through sample holder for the LSFM system.

D. Image acquisition part via the detection side

The collected images of a fluorescent sample by the CCD camera with different axes in real-time are treated and combined using ImageJ software to create a 3D image view of the sample. The image acquisition process begins after the formation of the light sheet that can be monitored on the pc screen and the 4D-translation stage is used to adjust the sheet position. Here it is worth mentioning an appropriate color filter should be used to image the fluorescence effect of the sample. Despite that, it is essential that the sample receives the least amount of light exposure, which is why the laser is only turned on for the duration of the image recording by using an optical shutter.

4. Results and discussion

This chapter contains the results of my research work. The first part deals with the systematic Raman spectroscopic study of the degree of conversion of DEGDMA polymers fabricated by gamma radiation polymerization method in different solvents. In addition to the adaptation of a Raman spectroscopic method for the determination of the DC in these systems, this research also served as a basis for my further work, related to the fabrication of DEGDMA microparticles with fluorescent and SERS enhancement properties. The production and characterization of monodisperse luminescent microparticles is described in Chapter 4.2. The last section details the results related to the fabrication of SERS substrates: synthesis of polymeric microparticles decorated with gold nanoparticles, as well as its use for the detection of biological samples.

4.1. Study of the reaction kinetics of gamma radiation-initiated polymerization of diethylene glycol dimethacrylate in different solvents by Raman spectroscopy

The DEGDMA monomer has two methacrylate groups allowing the formation of a highly crosslinked structure. In case of gamma radiation initiation, the polymerization mixture is composed of only the solvent and the DEGDMA monomer and it has been shown earlier that bulk structures ranging from non-porous to macroporous character can be obtained by changing the type and the amount of the solvent [29,33,134]. It has also been shown that the degree of conversion is an important parameter that has to be determined for each monomer-solvent system individually [33].

The Raman spectrum of the non-irradiated DEGDMA monomer contains several well-defined peaks (bottom curve in Figure 22) related to different C–C, C–H, *etc.* bonds of the molecule [135,136], (Their detailed assignment will be provided later).

After the preparation of the polymer from the mixture of DEGDMA and ethanol by irradiating it with different doses of gamma radiation, most of the features of the Raman spectrum, such as peak positions, line widths and peak intensities, remain the same (top four curves in Figure 22). However, several Raman bands in the spectrum show a noticeable dependence on the applied irradiation dose. The intensity of two peaks, located at 1409 and 1645 cm^{-1}, decrease remarkably and they almost vanish completely above 8 kGy irradiation dose. The intensity of the peak around 1725 cm^{-1} also decreases, but only up to 8 kGy dose. Meanwhile, a shoulder appears next to this band at 1735 cm^{-1}, the intensity of which increases with the irradiation dose and it becomes the most intensive band of the high-wavenumber region

(above 1500 cm^{-1}) of the spectrum in samples obtained with doses above 8 kGy. In addition, two other peaks appear as a result of gamma irradiation around 830 and 970 cm^{-1}, and their intensity increases with the applied dose.
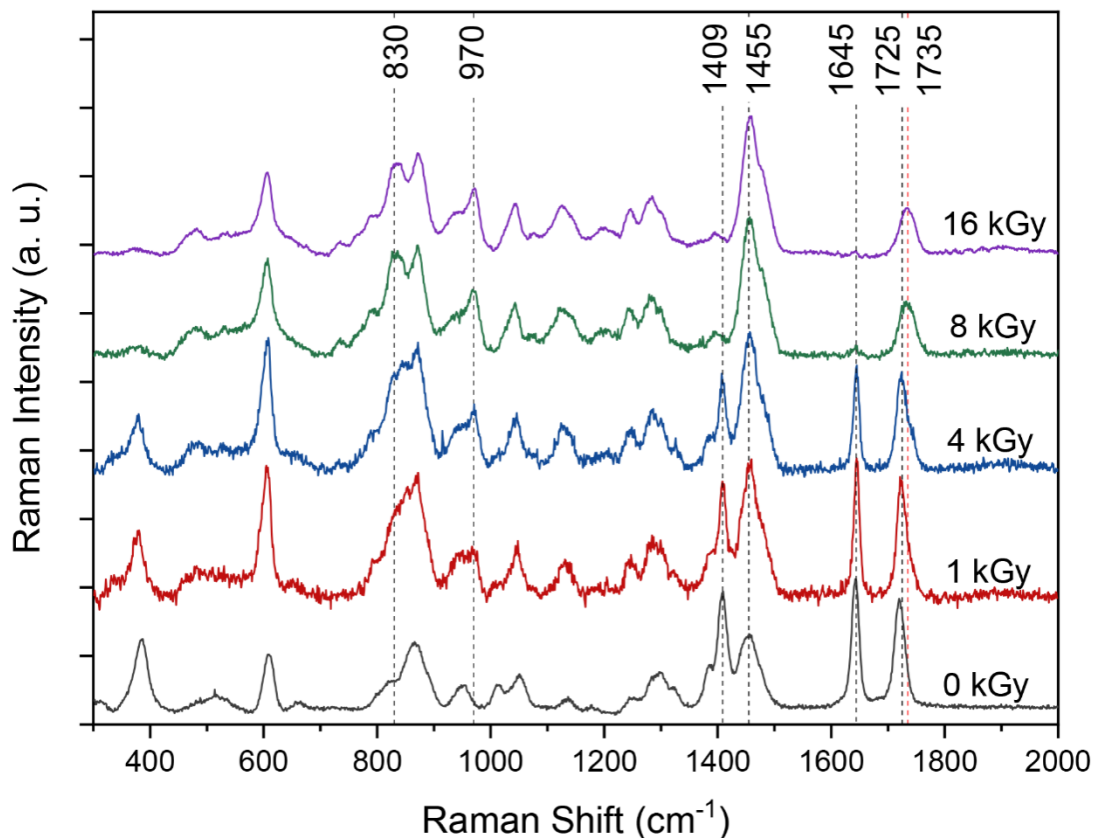

Figure 22: Evolution of the Raman spectrum of DEGDMA/ethanol polymer with applied irradiation dose.

In order to have a better understanding of the Raman bands' appearing in the Raman spectrum of DEGDMA after polymerization, the functional methacrylate group was used for modeling the polymerization process of DEGDMA monomer.

The model of methacrylate monomer was obtained by shortening and modification of the DEGDMA molecule at C-C bond position (Figure 23a,b). The modification consists of CH_2 to CH_3 group substitution prior to the corresponding C-C bond cleavage. The methacrylate polymer model was obtained by cleavage of C=C bond followed by substitution of =CH_2 group of methacrylate monomer by two -CH_2-CH_3 groups bonded to the main structure with single C-C bonds (Figure 23c).
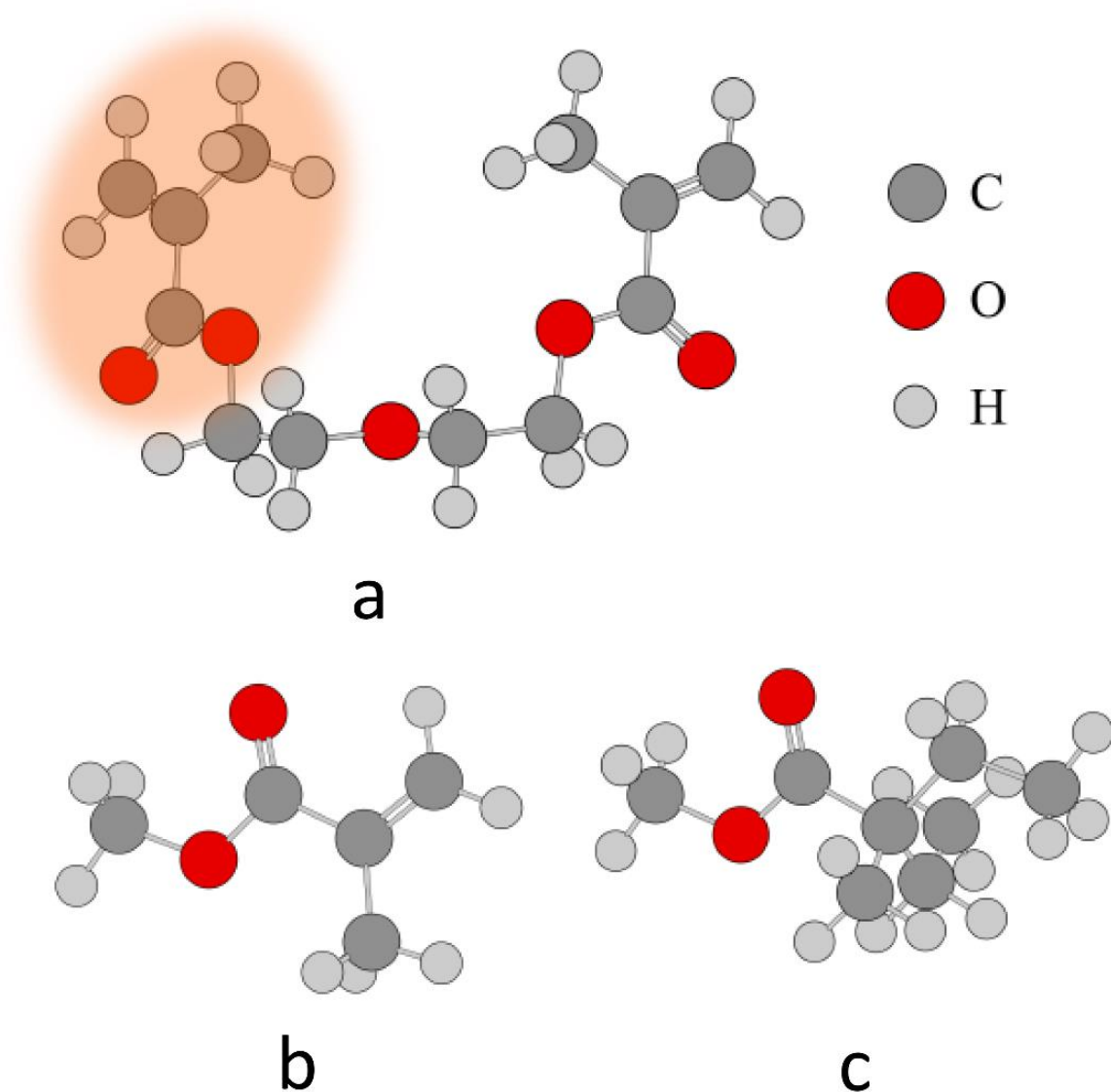
Figure 23: Geometry structure of DEGDMA (a) molecule and corresponding models of methacrylate group in their monomer (b), and polymer (c) states. [T1]

Lorentz-shape function with full width at half-maximum (FWHM) parameter of 10 cm^{-1} were applied for each computed Raman mode (Figure 24). The tentative assignments of the Raman active vibrational modes calculated for monomer and polymer states of methacrylate models are tabulated in Table 5. The theoretical modes of methacrylate models were correlated with the vibrational bands observed in the experimental Raman spectra of DEGDMA monomer and polymer.

Table 5: Experimental bands observed in the Raman spectra of DEGDMA monomer and polymer and calculated* Raman modes of methacrylate models together with their assignments**. [T1]

Monomer			Polymer		
Exp.	**Calc.**	**Tentative assignment**	**Exp.**	**Calc.**	**Tentative assignment**
384	373 389	δ(C-C=C), δ(C-CH$_2$,C=CH$_3$) δ(C-CH$_2$,C=CH$_3$)	373	348	δ(C-C-C)
			478	449	δ(C-C-C)
515	478	δ(C-C-C), δ(C-C-O)	532	469	δ(C-C-C), ν_s(C-C=O)
608	582	δ(C-C=C), δ(C-O-C,O-C=O), ν(C-C)	606	597	δ(C-C-C), ν_s(C-C-C), δ(CH$_2$-CH$_3$)
660	650	δ(CH$_2$,CH$_3$)			
			735	726	δ(CH$_2$-CH$_3$), ν_s(C-C-C)
			762	753	δ(C-C-C), δ(CH$_2$-CH$_3$)
			791	790	δ(C-C=O,C-O-C), δ(CH$_2$-CH$_3$)
820sh	811	δ(C-C=O), ν_s(C-C-C), δ(C-CH$_3$)	830	848	ν_{as}(C-C-C), ν_s(C-O-C), δ(C-CH$_3$,O-CH$_3$)
866			873	879	ν_{as}(C-C-C), δ(C-CH$_3$)
			940	960 977	ν(C-C), δ(C-CH$_3$) ν(C-O), ν(C-C), δ(C-CH$_3$)
950	920	δ(C=CH$_2$), ν(C-C), ν_s(C-O-C)	970	994	ν(C-C), ν(C-O), δ(C-CH$_3$)
1014	959	δ(C=CH$_2$)			
	989	ν(C-O), ν(C-C), δ(C-CH$_3$,C=CH$_2$)			
1051	1005	δ(C-CH$_3$,C=CH$_2$), ν(C-O)	1043	1058	ν(C-C), ν(C-O), δ(C-CH$_3$)
1134	1142 1154	δ(O-CH$_3$), ν_{as}(C-O-C)	1127	1156	ν(C-C), δ(C-CH$_3$)
				1176	ν(C-O), δ(O-CH$_3$)
1179	1185	ν(C-O)	1200	1202	ν_{as}(C-C-C), δ(C-CH$_3$)
				1218	ν_{as}(C-C-C), ν_{as}(C-O-C)
1247			1246	1293	δ(CH$_2$), ν(C-C)
1294	1278	ν_{as}(C-C-C), ν(C-O)	1282	1345	ν(CH$_2$), ν_{as}(C-C-C),
1385	1376	δ_s(CH$_3$), δ(=CH$_2$)			
1409	1398	δ(=CH$_2$), δ_s(CH$_3$)			
1455	1444	δ_{as}(CH$_3$)	1455	1449	δ(CH$_2$), δ_{as}(CH$_3$)
1477	1455	δ_{as}(CH$_3$)	1477sh	1463	δ_{as}(CH$_3$), δ(CH$_2$)
1645	1649	ν(C=C)			
1720	1727	ν(C=O)	1735	1733	ν(C=O)

* The scaling factor of 0.975 was used for all calculated modes.

** ν, δ, s, as - stretching, bending, symmetric and asymmetric vibrations, respectively, sh- shoulder.

The 1409 and 1645 cm^{-1} bands correspond to the vibrations of the methacrylate group [137]. The rapid decrease of their intensity is caused by the polymerization which starts by creating a free radical by breaking the C=C bond in methacrylate group. These free radicals are transferred

to the monomer, forming an active center that can attack other monomers by propagation step. The reaction is terminated when two molecules containing free radicals react and form the final product of the poly(DEGDMA) matrix.
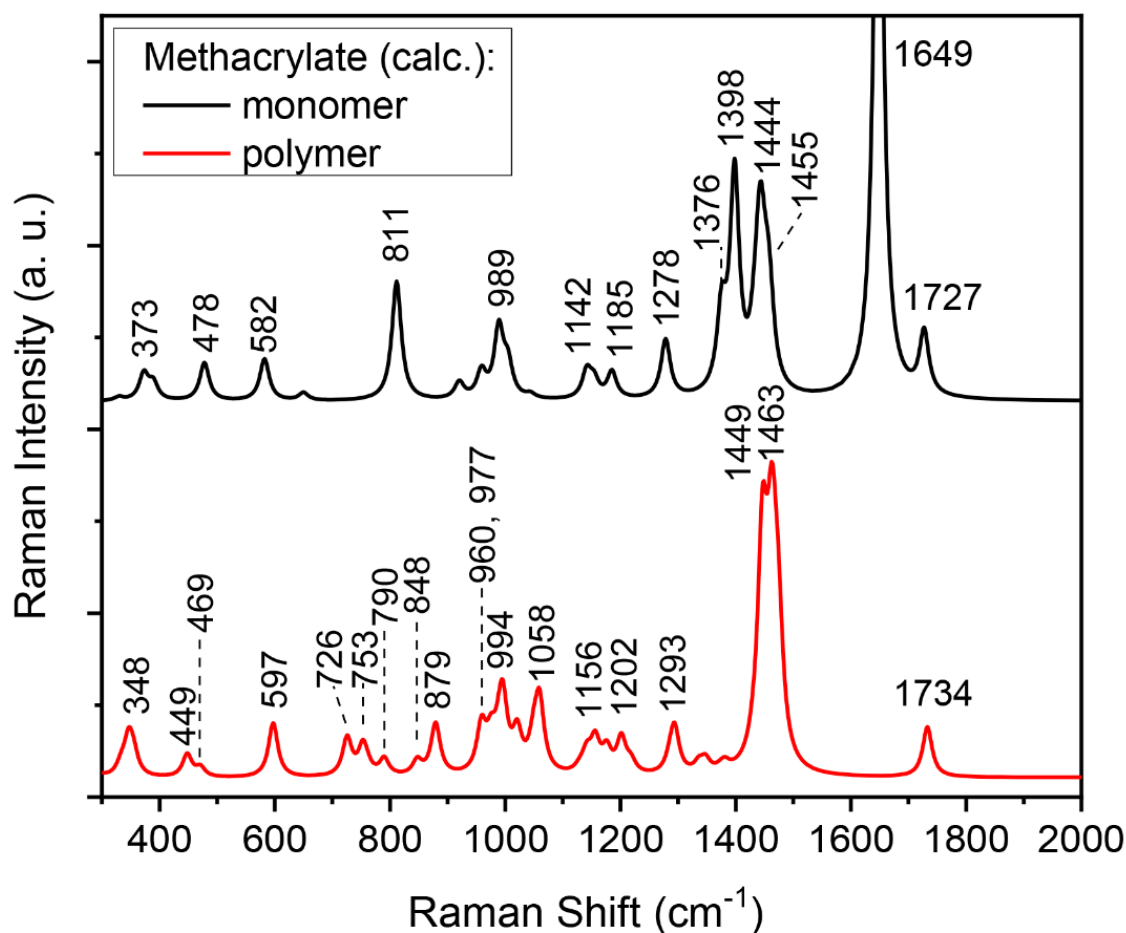

Figure 24. Simulated Raman spectra of methacrylate molecule in monomer and polymer states (the calculated frequencies were scaled by using the scaling factor of 0.975).

The band around 1725 cm^{-1} is related to the carboxyl (C=O) bond of the same methacrylate group [135]. This strong bond is not affected by the gamma radiation, however, its Raman activity is strongly dependent on the conjugation with the neighboring C=C bond described above. Due to this, the C=O peak intensity decreases as the amount of the C=C bonds decreases. However, the carbonyl groups of the formed polymer network will have their own Raman scattering contribution appearing as a new band at 1735 cm^{-1}, shifted to higher wavenumbers due to the lack of conjugation. In other words, gamma radiation enhances the free radical density or electron density in the polymer matrix. This rise in electron density results in a reduction in the order of the C=O bonds, which in turn decreases the intensity and shifts

the peak of the carbonyl [138]. Therefore, the appearance of this new component is an evidence of the increasing degree of polymerization as well.

According to Table 5, the 830 and 970 cm^{-1} peaks are complex ones that are related to C–C and C–O vibrations in different configurations. This assignment is also in good agreement with results published earlier [135,139,140]. The increasing intensity of these peaks with irradiation dose is also an indication of the higher levels of crosslinking, resulting in the formation of new C–C and C–C–C groups in the polymerized matrix.

All the obtained spectra in Figure 22 were normalized to the 1455 cm^{-1} C–H deformation Raman band of the CH$_3$ group of DEGDMA (this band is not affected by the polymerization). This peak has been used as reference peak for the determination of the relative intensity of the C=C Raman band at 1645 cm^{-1}. The C–H deformation and C=C Raman bands were fitted using Lorentzians. Since the 1455 cm^{-1} peak has a shoulder at 1482 cm^{-1}, an additional Lorentzian has been used to obtain the peak intensities precisely. An illustration of the peak fitting is shown in Figure 25.
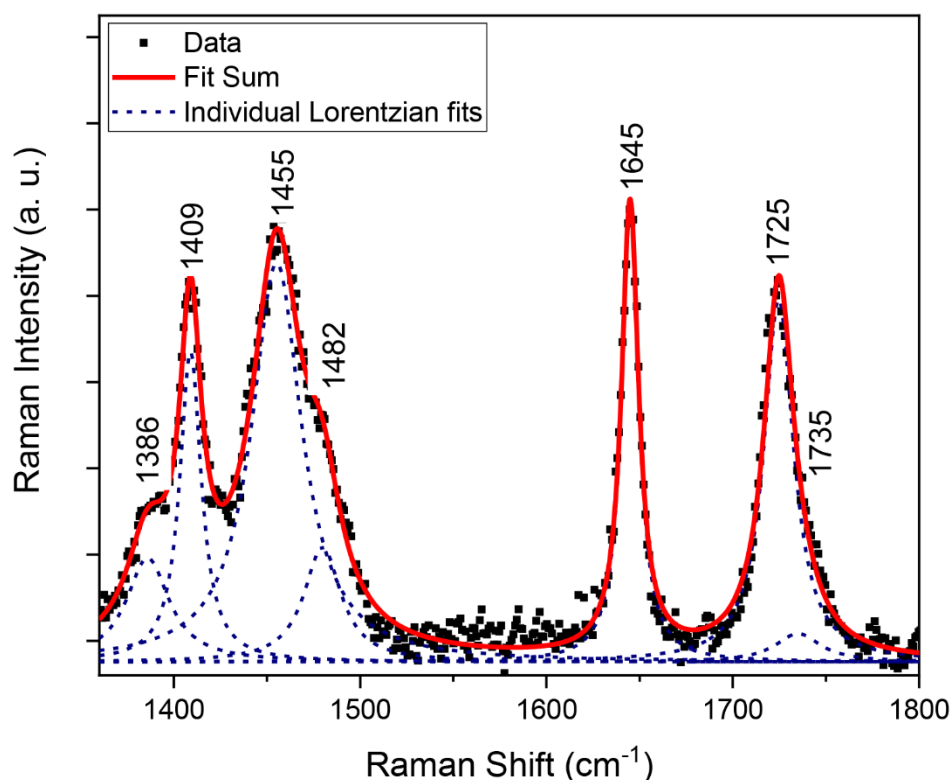

Figure 25: Fitting of the 1360-1800 cm^{-1} region of the Raman spectrum of DEGDMA irradiated with 1 kGy dose with a set of Lorentzian peaks.

The Raman spectroscopy-based degree of conversion (DC_{Raman}) of the cross-linked polymer after gamma irradiation treatment was calculated from the intensity of the Raman peak related to the C=C bond of the methacrylate group at 1645 cm^{-1} according to the following equation [30]:

$$DC_{Raman} = (1 - (R_{C=C}/R_{reference})) \times 100\%, \qquad (22)$$

where $R_{C=C}$ and $R_{reference}$ are the Raman intensities of the 1645 and 1455 cm^{-1} bands in the spectrum after the normalization, respectively. This approach is widely used for the determination of the degree of conversion of different polymers, for example for dental materials [141–144].

Weight-based degree of conversion (DC_{Weight}) has been determined from the weight difference of the monomer and the polymer measured by using a laboratory scale with 0.1 mg precision. The weight of the monomer was measured before mixing it with the solvents. After the irradiation, the obtained samples were washed three times with the corresponding solvent to remove the non-reacted monomers. Then, they were dried at 50°C for two weeks before the weight measurement. The DC_{Weight} values have been determined by using the following equation [35]:

$$DC_{Weight} = (m_{polymer}/m_{monomer}) \times 100\%, \qquad (23)$$

where $m_{polymer}$ and $m_{monomer}$ are the measured weights of the polymer and the monomer, respectively.

Since, in terms of bonding, the degree of polymerization is determined by the number of C=C bonds transformed into single C–C bonds and attached to the polymer network, it can be expected that the change of the intensity of the C=C Raman peak will correlate with the degree of polymerization, and the disappearance of the band is an indication of complete conversion of the monomers. Figure 26a shows the DC_{Raman} data for the DEGDMA monomers irradiated with increasing doses in different solvents. The values were obtained from the Raman peak intensities derived by Lorentzian fitting procedure and using Eq. (22). Beside DC_{Raman}, the weight-based DC_{Weight} values were also calculated using Eq. (23) and the obtained data are shown on Figure 26b. Both Figure 26a,b shows that the type of the solvent has a remarkable effect on the DC and hence, on the kinetics of the polymerization. In general, gamma radiation-initiated polymerization is the fastest for alcohol solvents, followed by ethyl acetate and

acetone. Doses of 10–15 kGy are enough to reach the plateau of the DC curve in all cases. Comparison of Figures 26a,b also show that while the data obtained with the two methods for the different DEGDMA/solvent systems are very similar, DC_{Raman} indicates more rapid kinetics for the polymerization.
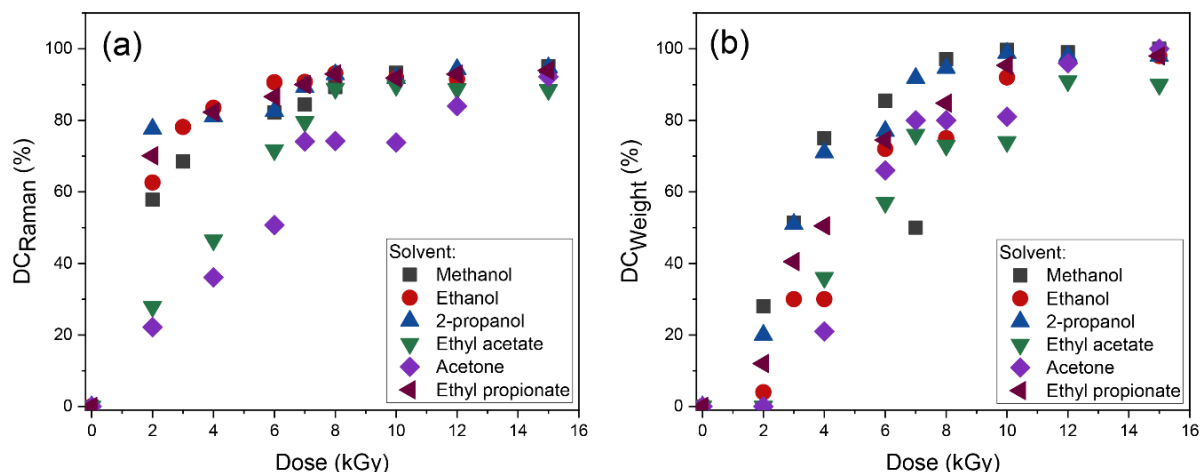

Figure 26: Degree of conversion of different DEGDMA/solvent systems with applied dose determined from (a) Raman peak intensity ratios and (b) weight difference measurements.

The experimental results shown in Figure 26 were also evaluated in terms of reaction kinetics. Figure 27a,b shows the DC_{Raman} and DC_{Weight} values for DEGDMA polymer versus polymerization time. The polymerization time was obtained from the dose and the dose rate values. The data in the Figures were fitted with the Avrami equation [45,145]:

$$y(t) = a\,(1 - \exp(-kt^n)), \tag{24}$$

where *a* is a correction factor, *k* is the Avrami constant related to the reaction rate, and *n* is the Avrami exponent. In case of polymerization, the reaction rate *k* is dependent on the nucleation rate and the propagation rate. The Avrami exponent, on the other hand, is determined by the character of the nucleation and propagation and could have different values ranging from 1 to 4. The former value is characteristic of constant nucleation rate, while the latter of systems with variable nucleation in three dimensions [44]. It should be noted that, since the Avrami exponent is related to the polymerization mechanism, fitting was performed by using the same *n* value for a given solvent in both weight and Raman datasets.

The results of the fitting (in Figure 27) for the different DEGDMA/solvent systems with the two methods are summarized in Table 6 and Table 7, while the determined Avrami constants are shown in Figure 28. The comparison shows remarkable differences between the values
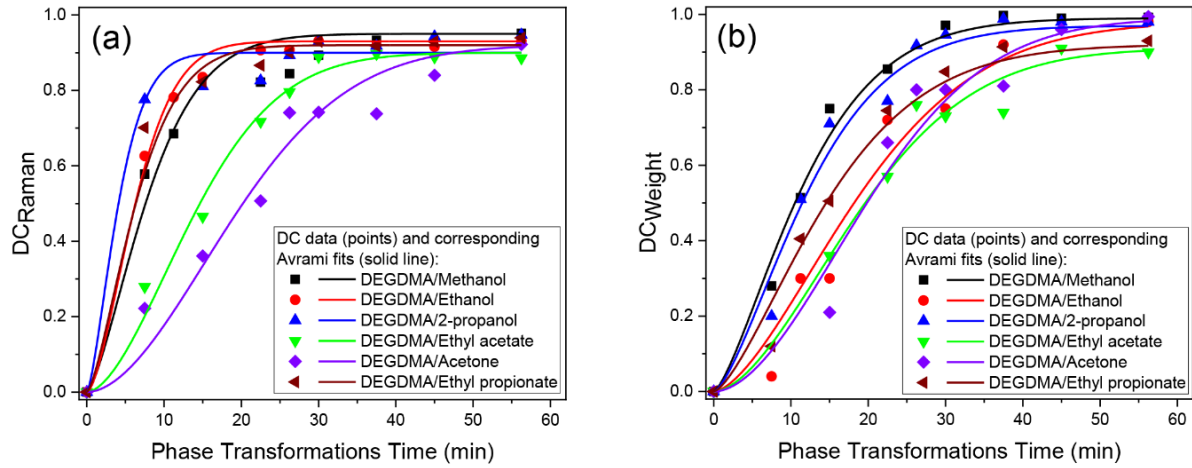
Figure 27: Fitting of the (a) DC_{Raman} and (b) DC_{Weight} data with the Avrami function fr different DEGDMA/solvent systems.

given in the two Tables. The Raman-based Avrami constants always higher than the weight-based ones. Since the same samples were measured with both methods, this difference should be related to the measured property. While weight difference gives information on the mass of the already polymerized amount of the monomer, the decrease of the C=C Raman peak intensity is related to the number of transformed double bonds. In case of monomers with a single carbon double bond, there should be a linear dependence between these two quantities. However, DEGDMA is a compound with two methacrylate groups forming a cross-linked structure instead of chains, so a given amount of this polymer with a higher level of cross-linking will show a C=C Raman peak of smaller intensity. As a consequence, the Raman-based Avrami constant will always be higher than the weight-based one and the difference will be indicative of the level of cross-linking of the structure.

Table 6: Avrami constants obtained from fitting of the DC_{Raman} data.

Composition	k_{Raman} (min^{-n})	n_{Raman}	a_{Raman}
DEGDMA/Methanol	0.0460	1.40	0.95
DEGDMA/Ethanol	0.0400	1.61	0.93
DEGDMA/2-propanol	0.1045	1.45	0.90
DEGDMA/Ethyl acetate	0.0076	1.74	0.90
DEGDMA/Acetone	0.0460	1.85	0.92
DEGDMA/Ethyl propionate	0.0531	1.33	0.91

Table 7: Avrami constants obtained from fitting of the DC_{weight} data.

Composition	k_{Weight} (min^{-n})	n_{Weight}	a_{Weight}
DEGDMA/Methanol	0.0261	1.40	0.99
DEGDMA/Ethanol	0.0067	1.61	0.98
DEGDMA/2-propanol	0.0211	1.45	0.97
DEGDMA/Ethyl acetate	0.0045	1.74	0.91
DEGDMA/Acetone	0.0028	1.85	0.99
DEGDMA/Ethyl propionate	0.0162	1.33	0.92
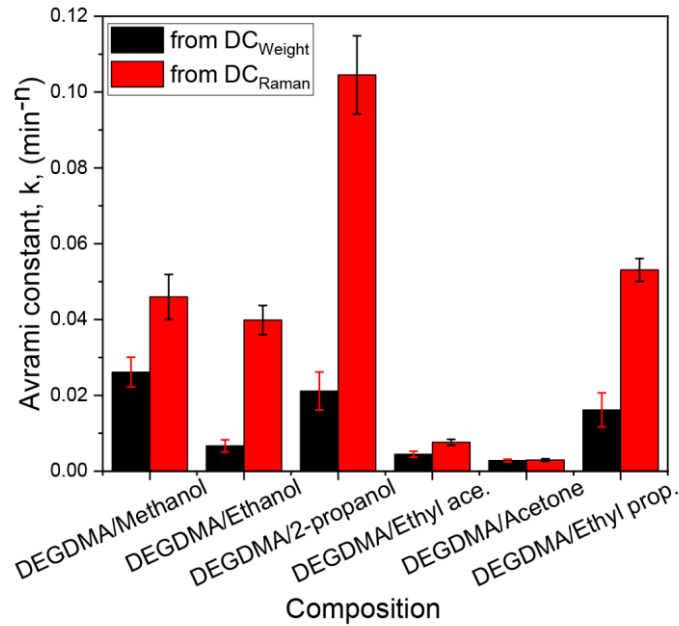
Figure 28: Comparison of k values obtained by fitting the DC_{Raman} and DC_{Weight} data for different DEGDMA/solvent systems.

The data in Tables 6, 7 and Figure 28 show that indeed the alcohol solvents have the highest reaction rates, in the order of 2-propanol > methanol > ethanol and methanol > 2-propanol > ethanol for the Raman spectroscopic- and weight-based methods, respectively. Ethyl acetate and acetone have an order of magnitude smaller *k* values. This difference is mainly due to the polymerization mechanisms being characteristic of the different solvents. As it has been shown earlier, a precipitation polymerization occurs when the DEGDMA monomer is dissolved in alcohols, resulting in a highly micro- and macroporous structure [34]. Since the solubility parameter of alcohols (16.1, 13.4, and 12.3 (Cal/cm^3)$^{0.5}$ for methanol, ethanol, and 2-propanol, respectively) are much larger than that of DEGDMA (6.8 (Cal/cm^3)$^{0.5}$), the growing nuclei quickly precipitate from the solution, and the polymerization continues at the precipitate-

solution interface. The forming new nuclei will also be "absorbed" by the precipitates, which further facilitates their growth. As a consequence, the polymer formation in alcohol solvents is a fast process, occurring simultaneously in many places at the precipitates surface. On the other hand, the solubility parameter of ethyl acetate and acetone are 9.1 $(Cal/cm^3)^{0.5}$ and 10.1 $(Cal/cm^3)^{0.5}$, respectively, and in these solvents DEGDMA precipitates at later stages. Therefore, less propagation occurs simultaneously, and rather a bulk or nanoporous polymer forms upon irradiation. This difference in the polymerization mechanism is responsible for the behavior of the Avrami exponents n_{Raman} and n_{Weight}, being some 15–20% higher for ethyl acetate and acetone compared to the alcohols.

Comparison of the values in Tables 6 and 7 shows that the k values obtained by the Raman and the weight difference methods are similar for acetone, but there is a remarkable difference for some other solvents, especially for 2-propanol. This behavior is presumably caused by the character of the formed polymer and the weight measurement procedure. Only minimal amount of the polymer will be removed during the washing step from the bulk polymer obtained with acetone, while this is not true for the loosely connected nuclei and small fragments formed in alcohols. As a result, smaller k values will be obtained from the weight difference measurements for these solvents.

The correction factor a indicates the height of the plateau of the fitted curves or the degree of polymerization corresponding to total conversion conditions (doses above 12 kGy). It can be seen that according to the weight difference measurements, the conversion is above 97%. However, Raman data give values between 90–95% only. Since Raman spectroscopy detects the intensity of the methacrylate peaks values below 100% indicate the presence of methacrylate groups with intact C=C bonds in the structure. These presumably belong to DEGDMA monomers being either trapped in the polymer network or being connected to the polymer frame through one of their two methacrylate groups only. In other words, structures with lower values are less crosslinked.

In conclusion, the results of this work have shown that the Raman method allows determining the conversion rate of polymeric structures by a non-destructive and, in terms of realization, simple manner. A good agreement was found in the DC determined by Raman spectroscopy and mass difference-based techniques. The data were fitted with the Avrami equation, and the observed differences in the reaction rate were explained by the different characters of the DEGDMA polymerization mechanism in alcohols and other types of solvent,

caused by their solubility values. It was found that the DC for DEGDMA reaches a plateau by increasing the irradiation doses and it exceeds 90% above 12 kGy, independently of the applied solvents. Raman measurements revealed also that there are DEGDMA monomers entrapped intact into the polymer matrix and/or attached to the frame only through the methacrylate group.

4.2. Preparation and characterization of fluorescent monodisperse microparticles prepared by gamma radiation-initiated polymerization

During gamma radiation, free radicals are created in the monomer mixture. These radicals initiate the polymerization reaction and the chain formation in many points of the volume simultaneously, forming a high number of nuclei, the density of which is determined by the dose rate. During the propagation, more and more monomers bind to these nuclei, they grow with time, and – in some specific solvents – precipitate after reaching a certain size. Then, the propagation continues at the precipitate's surface. Since these nuclei are floating in the monomer mixture and they do not shadow the gamma radiation, the formed particles will have a spherical shape. The process ends when the radiation is terminated, or all the monomers are polymerized. In other words, precipitation polymerization occurs during irradiation, and the mixture changes from homogenous to heterogeneous because of cross-linking and polymerization. The properties of the formed particles can be controlled by the composition and concentration of the monomer mixture, and the irradiation conditions, including mainly dose and dose rate [47].

My work on the preparation of fluorescent microparticles started with the detailed study of the conditions of monodisperse microparticle formation from diethylene glycol dimethacrylate. This preparation method with gamma radiation initiation and ethyl propionate solvent has been demonstrated earlier [47], but it was necessary to elaborate the specific conditions for the fluorescent microparticles.

I first studied the effect of the irradiation dose and monomer concentration on the properties of created monodisperse DEGDMA particles. For this, a series of 1, 5, and 10 vol% DEGDMA concentrations in ethyl propionate solvent were irradiated with 1,7, 10, and 15 kGy doses. Our experiments showed that particle formation cannot be detected in the samples irradiated with doses below 4 kGy (Figure 29: a1, b1, and c1). Above 7 kGy microparticles were already observed in the SEM images (Figure 29: a2, b2, and c2). Particle ensembles of nearly identical character (size and density) were obtained with irradiation doses between 10

and 20 kGy as shown in Figure 29: a3, a4, b3, b4, c3, and c4, indicating that the monomer reserve is a bottleneck above 10 kGy. Therefore, 10 kGy dose was used in further experiments.

This dose value is in good agreement with the results of polymer conversion studies presented in section 4.1 showing that increasing irradiation doses result in the DC for DEGDMA reaching a plateau and that it approaches 90% between 8 kGy and 12 kGy, depending on the solvent used in the experiment.
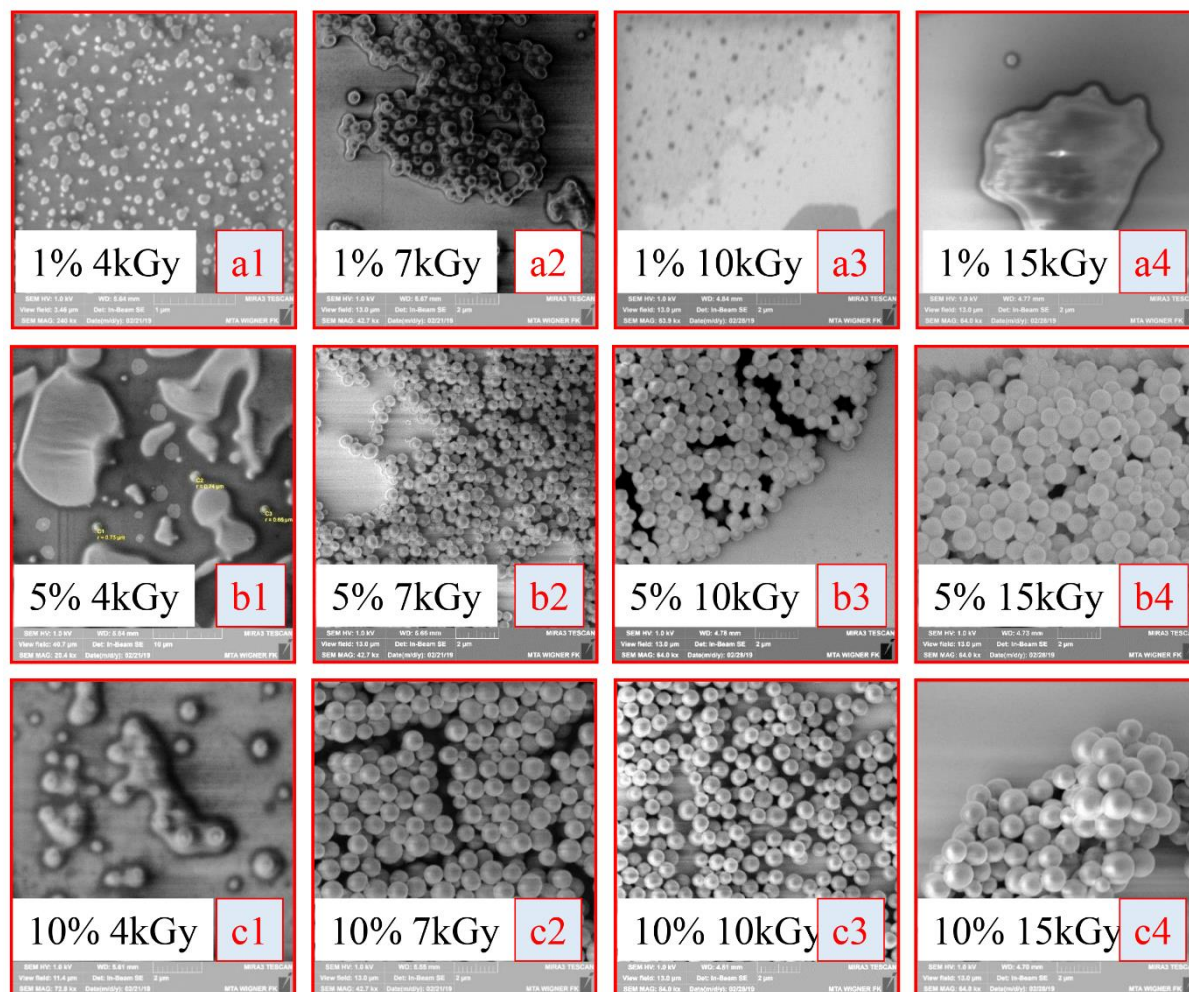

Figure 29: SEM images of monodisperse microparticles prepared from DEGDMA monomer as a function of the irradiation dose (4, 7, 10 and 15 kGy) and monomer concentration (1, 5, and 10 vol%).

Reactions performed with different monomer concentrations in ethyl propionate revealed that concentration also affects the microparticles formation. Polymeric particles were not formed for DEGDMA concentrations below 5 vol% in the monomer mixture. This means that the radicals formed were probably quenched in non-polymerization type reactions when the monomer concentration is too small, and a high enough concentration is needed for an effective

collision of the radicals [28]. Figure 30 shows SEM pictures of microparticles prepared with 5 vol% and 10 vol% DEGDMA content. It can be seen that microobjects with a shape close to spherical were formed in both cases (it should be noted that the drying and the vacuuming in the SEM station could affect the morphology of the particles). The monomer concentration was found to have less effect on the size of the created particles: the average particle size is 0.65 μm for 5 vol% and 0.75 μm for 10 vol% monomer concentrations. This observation is in good agreement with earlier results [47]. The monodispersity of the particle ensembles indicates the instantaneous character of the particle nucleation. Based on our findings we used 5 vol% DEGDMA solution in further experiments.
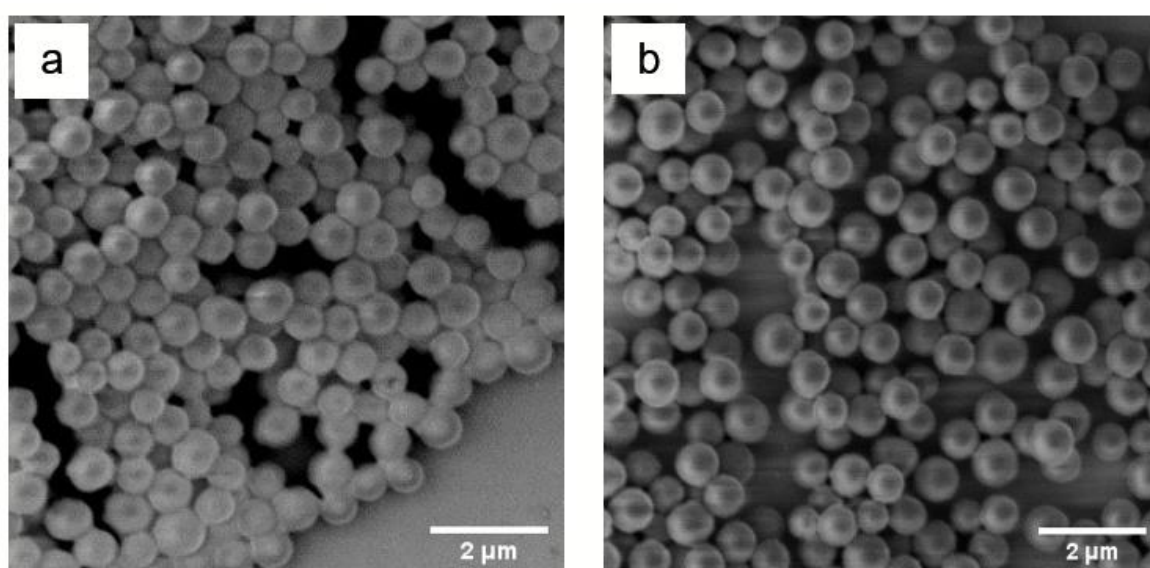

Figure 30: SEM images of monodisperse microparticles prepared from monomer mixtures with (a) 5 vol% and (b) 10 vol% DEGDMA concentration in ethyl propionate. The irradiation dose was 10 kGy.

In the next step of fluorescent microparticle preparation, the effect of the dye concentration was evaluated. The main goal is to prepare fluorescent micro- nanoparticles that can be used in fluorescent imaging as an alternative to pure dye since the traditional organic dyes or fluorescent proteins are employed for *in vivo* or *in vitro* imaging, but one of the major drawbacks is the dye's high photobleaching rate, which makes long-term imaging difficult lead to photodamage of the sample. The performance of the DEGDMA polymer by gamma radiation-induced polymerization with the ethyl propionate solvent was a motivation to incorporate FITC dye into a polymer matrix as an attempt to form fluorescent microparticles. Here I would like to mention that there is no effect of gamma radiation on the structure and optical properties of FITC.

Figure 31 shows SEM pictures of microspheres synthesized with 5, 10, 15, and 20 vol% FITC added to the monomer mixture having 5 vol% DEGDMA content. It can be seen that the formed FITC/DEGDMA composites are less uniform than the pure polymer and the presence of the dye affects their shape as well. Some particles have a non-spherical and elongated shape. Elongated particles are likely those which contain two seeds that coalesced in the very early phase of the growth process. Particles with 2–4 quasi-spherical segments might have attached to each other in the later phase of the growth process, and the side of each sub-particle not touching the other(s) could grow independently of the agglomeration process.
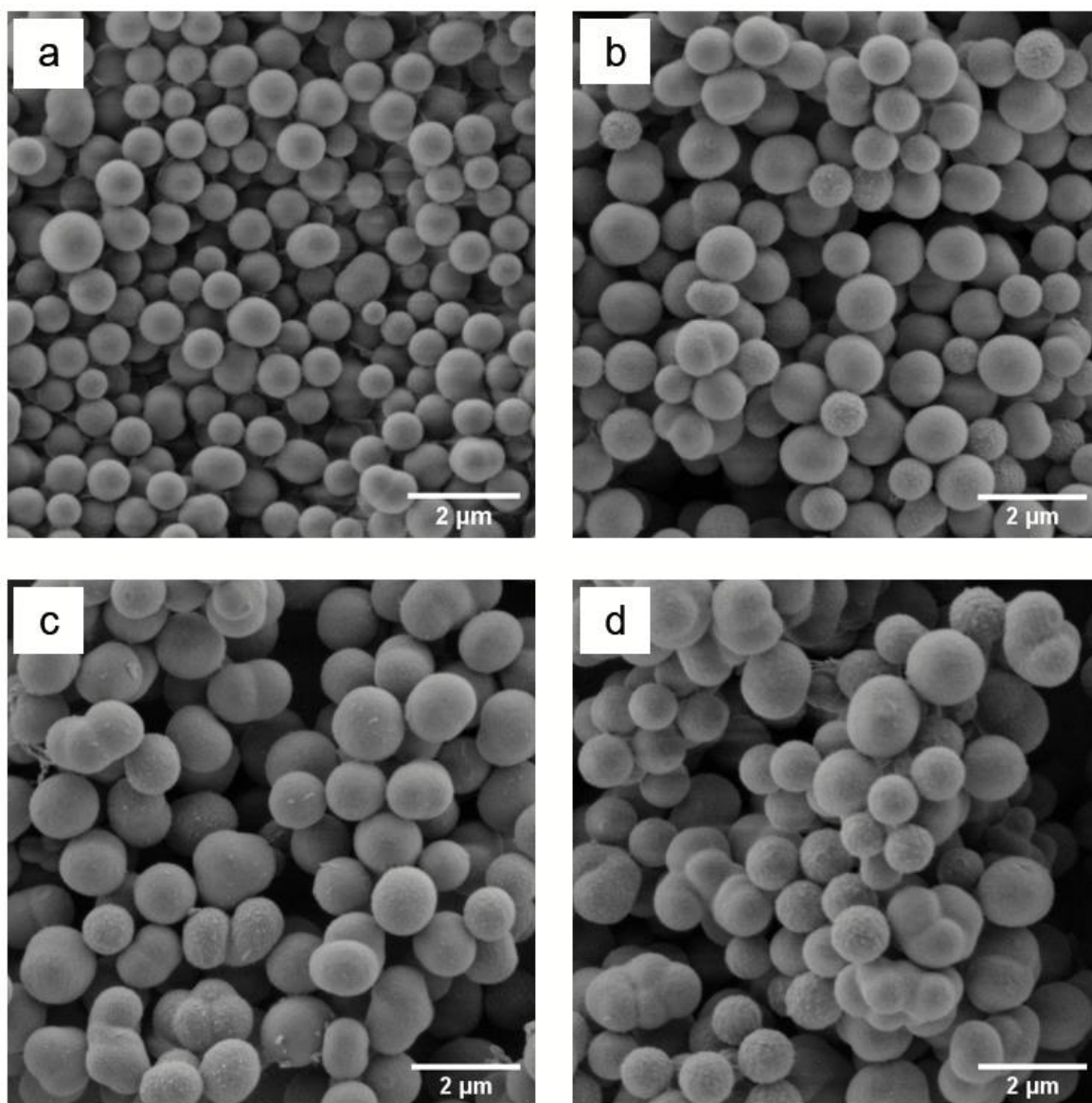

Figure 31: SEM images of luminescent monodisperse particles prepared from ethyl propionate and 5 vol% DEGDMA monomer mixture with different FITC concentrations: (a) 5 vol%, (b) 10 vol%, (c) 15 vol%, and (d) 20 vol%. The irradiation dose was 10 kGy.

In addition, the amount of FITC was found to affect the average particle size as well. Values obtained from the SEM images (Figure 32) show that the particle size increases with FITC concentration from 0.65 μm (0 vol% FITC) to 1.15 μm (15 vol% FITC). A slight decrease can be seen above this concentration.
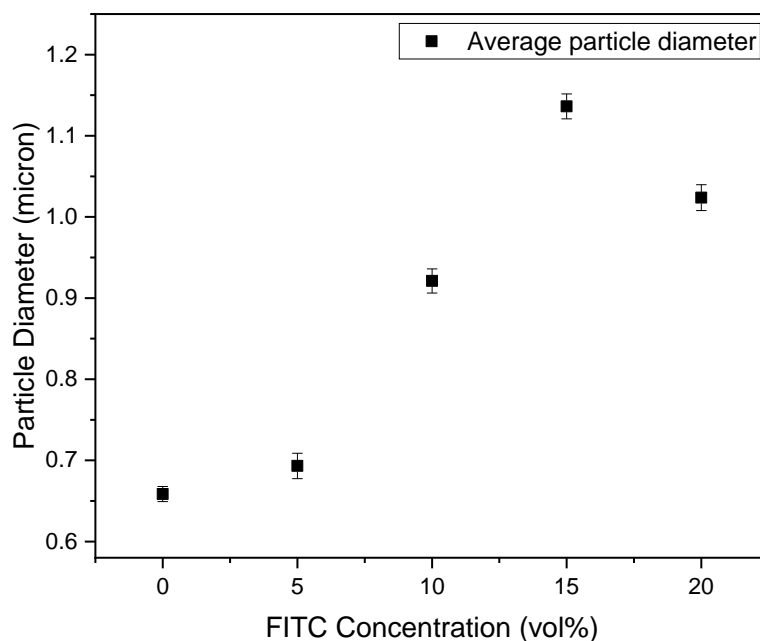

Figure 32: Effect of FITC concentration on the average particle size prepared with 5 vol% DEGDMA concentration and irradiation dose of 10 kGy.

In the first experiments, reaction mixtures with 5 vol% of acetone but without FITC were also tested. The result proved that acetone does not have any appreciable effect on the growth of the spherical particles at this concentration. It can be seen that the presence of FITC has a remarkable effect on the size and shape of the formed microparticles. While FITC is not taking part directly in the free radical polymerization, it can inhibit the chain formation and propagation by impeding the activated monomers.

The nucleation density is determined by the probability of chain formation. It will decrease upon addition of FITC, acting as an inhibitor. Lower nucleation density means fewer growing nuclei and, as a result, a smaller number of precipitated particles in the mixture. Consequently, the latter can grow larger because of the higher monomer reserve in the mixture. However, the inhibitor effect of the dye will decrease the propagation and the growth speed of nuclei. The competition of these two processes will determine the particle size. As Figure 32 shows, this parameter increases only up to 15 vol% FITC concentration. Above this threshold, the particle diameter decreases due to the high amount of the dye. The termination of the

propagation by incorporating FITC molecules could be responsible for the distorted shape of some of the particles (Figure 31).
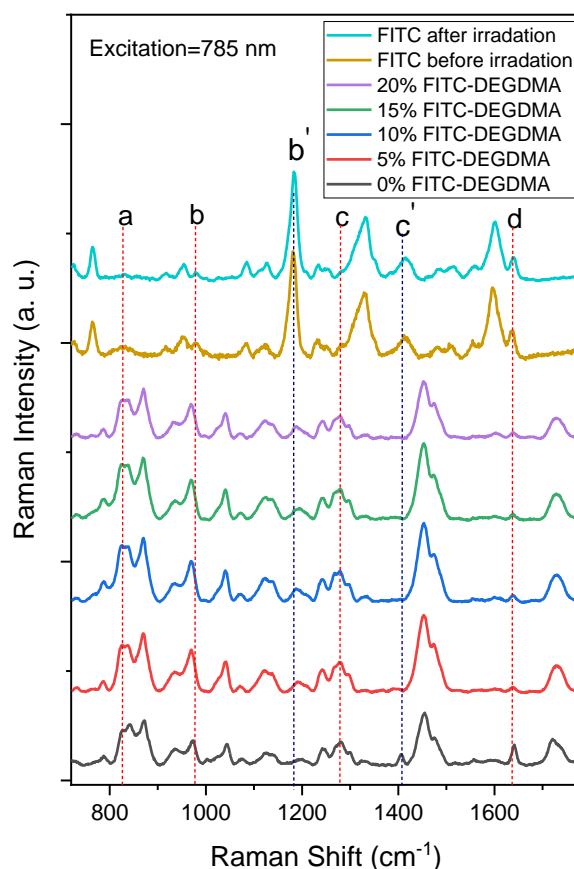

Figure 33: Raman spectra of untreated and irradiated FITC solution, and FITC/DEGDMA composite prepared from 5 vol% DEGDMA monomer with 0, 5, 10, 15, and 20 vol% FITC content. The irradiation dose was 10 kGy (dashed lines: a: 827 cm^{-1}, b: 980 cm^{-1}, b': 1182 cm^{-1}, c: 1280 cm^{-1}, c': 1410 cm^{-1}, d: 1638 cm^{-1} (C=C Raman peak)).

The structure of the samples was studied by Raman spectroscopy. The Raman spectra obtained with 785 nm excitation were normalized to the 1452 cm^{-1} peak after baseline correction. The C=C and C=O peaks at 1638 and 1730 cm^{-1} were fitted using Lorentzians. Raman spectra of the FITC solution (before and after irradiation), pure DEGDMA, and FITC/DEGDMA composites prepared with 10 kGy irradiation dose and different FITC concentrations are shown in Figure 33. The FITC spectra recorded before and after irradiation are very similar, showing that the dye structure is neither destroyed nor altered remarkably upon gamma radiation. Some changes can, however, be observed after the irradiation: the broad peak around 827 cm^{-1} (peak 'a') almost completely disappeared, the relative intensity of the peak at

980 cm^{-1} (peak 'b') is decreased, while the shoulder at 1280 cm^{-1} (peak 'c') became weaker. These changes indicate that some structural alterations occurred after the treatment.

The Raman spectra of the composites are dominated by the DEGDMA peaks and only the strongest FITC peak (peak (b')) can be detected there, the intensity of which increases with FITC concentration.

Analysis of the C=C Raman peak of DEGDMA (peak 'd' in Figure 33) allows to study the effect of the dye on the conversion rate of the DEGDMA matrix. The peak intensities were obtained by fitting of the 1638 cm^{-1} peak and its subsequent normalization on the fitted 1452 cm^{-1} band of the polymer frame not affected by the irradiation [30]. As Figure 34 shows, the conversion is remarkably higher upon the addition of FITC (Figure 34a shows the change of the vinyl peak area, so the lower the value, the lower the amount of vinyl groups and higher the conversion). Since DEGDMA is a monomer with two vinyl groups, this means the formation of a matrix with a higher level of cross-linking, which can be attributed to the inhibition and termination effect of the FITC discussed above. If the involvement of a new monomer molecule from the solution is hindered by the dye, the probability of bond formation inside the polymer matrix increases. Figure 34b shows the calculated DC of DEGDMA at different concentrations of FITC by using Eq. (22).
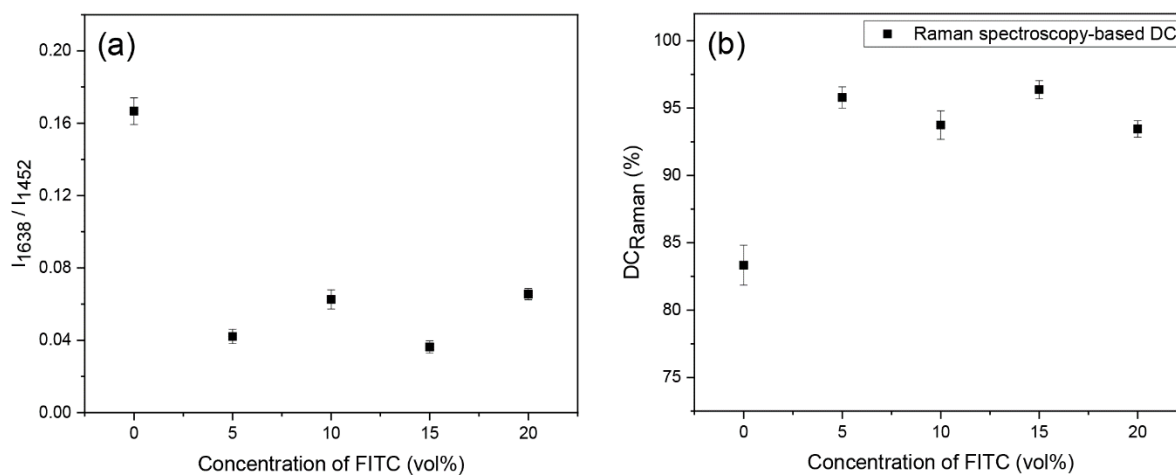

Figure 34: Polymer conversion rate of DEGDMA calculated from the intensity of the Raman peak of the vinyl group at 1638 cm^{-1} as a function of the FITC concentration, (at 10 kGy irradiation dose).

Figure 35a shows the photograph of the vials containing the gamma radiation-treated sample. It can be seen that the suspension prepared with 0 vol% FITC is the whitest and has the highest opacity. As the FITC concentration increases the color of the sample gradually changes

to yellow and it becomes more transparent. This behavior can be seen on the UV–Vis transmittance spectra (Figure 35b) that gradually increases with FITC concentration. In addition to the overall increase of the transmittance, the shape of the curve also changes between 540 and 900 nm. The transmittance is above 40% in this region for the sample prepared with 20 vol% FITC concentration.
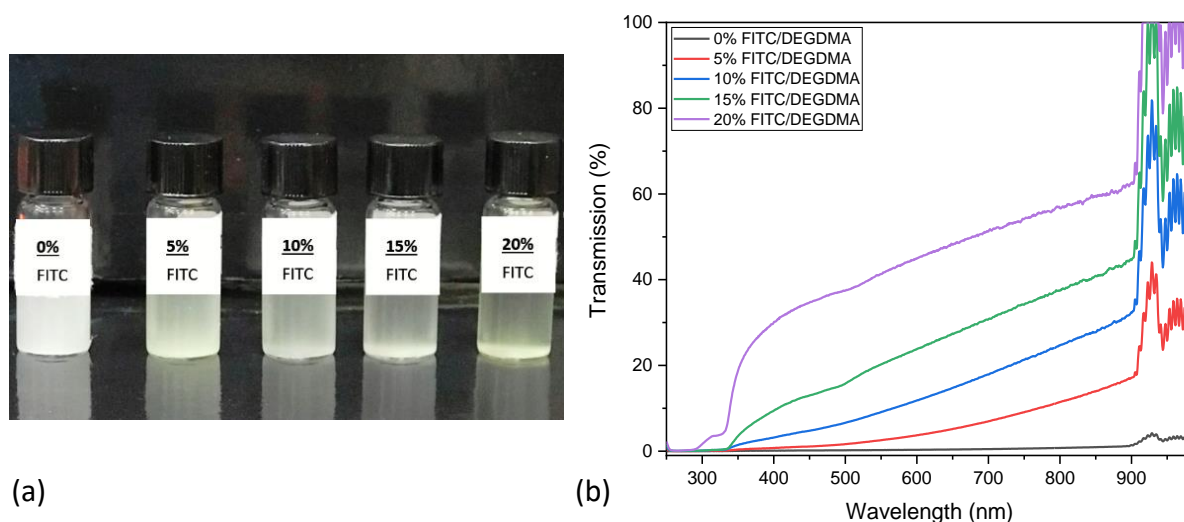

Figure 35: (a) Photograph of gamma-irradiated FITC/DEGDMA composite showing the gradual increase of the light transmittance (the suspension in the vials were washed three times), (b) UV–Vis spectra of FITC/DEGDMA composite microparticles with different concentrations of FITC.

Figure 36 compares the photoluminescence excitation–emission spectra of pure DEGDMA and composite FITC/DEGDMA microparticles and the FITC before and after irradiation. DEGDMA has one strong emission peak around 450 nm that can be excited efficiently around 400 nm. The emission band of FITC is located in the 500–540 nm region and can be excited in the region of 440–470 nm. The same emission peak can be observed in the spectrum of the composite, which is a clear indication of the presence of FITC in the particles. However, while the emission still can be excited in the region mentioned for the FITC above, its highest efficiency is shifted to 410–430 nm. This difference suggests that the dye molecules are not only entrapped in the polymer matrix but form new structural units with electronic levels involved in the new PL excitation mechanism.
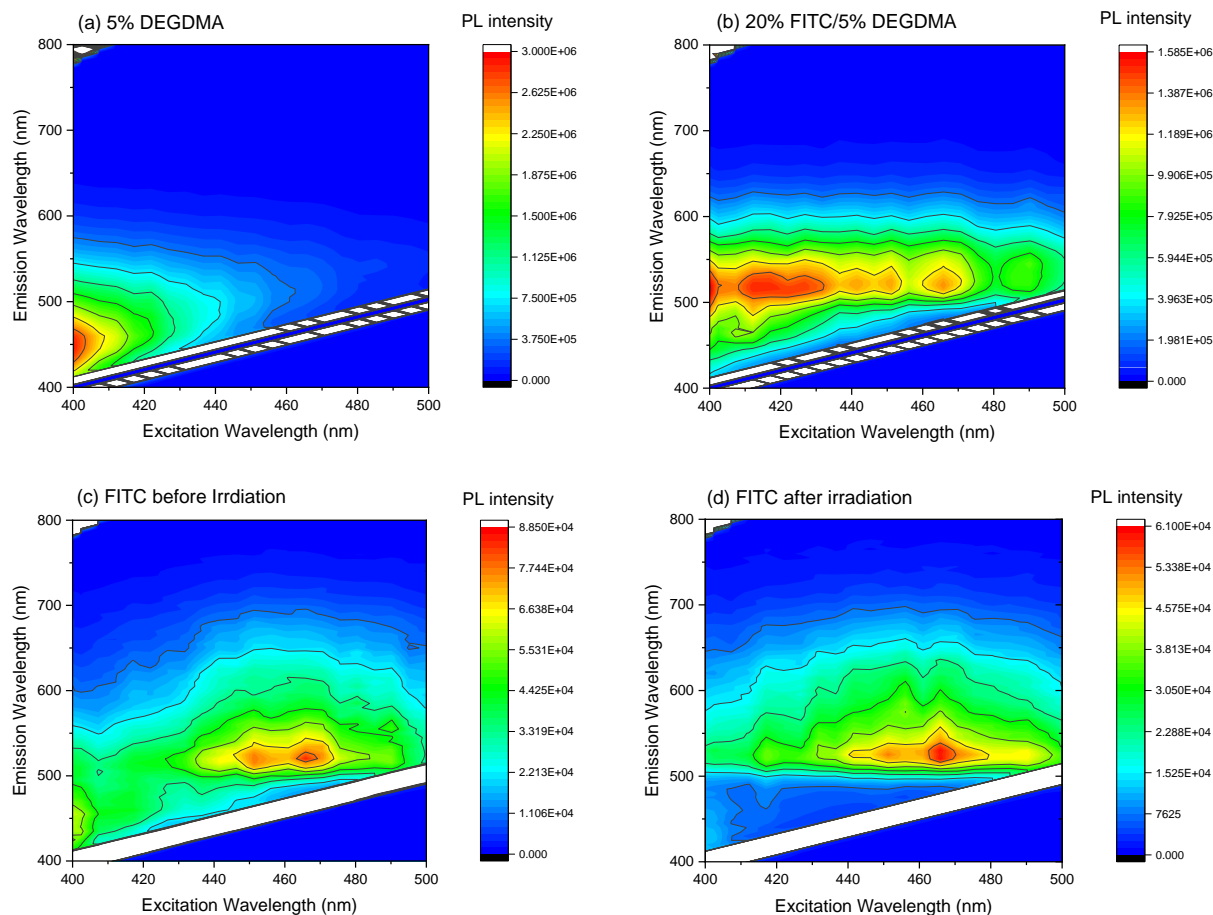
Figure 36: Photoluminescence excitation-emission spectra of (a) pure DEGDMA, (b) composite FITC/DEGDMA microparticles, (c) FITC before irradiation, and (d) FITC after irradiation.

The change of the PL emission peak intensity of FITC excited at 488 nm with FITC concentration is shown in Figure 37. The emission peak position was found to be shifted to 516 nm, compared to the 525 nm value of pure FITC. The values were obtained by fitting of the peak with Gaussian and normalization to the PL emission peak of DEGDMA, fitted with Gaussian as well. It can be seen that the relative peak intensity increases with FITC concentration. Whilst the dependence is not linear, the trend definitely indicates the relation of the emission peak with FITC and the incorporation of the dye into the polymer microparticles.
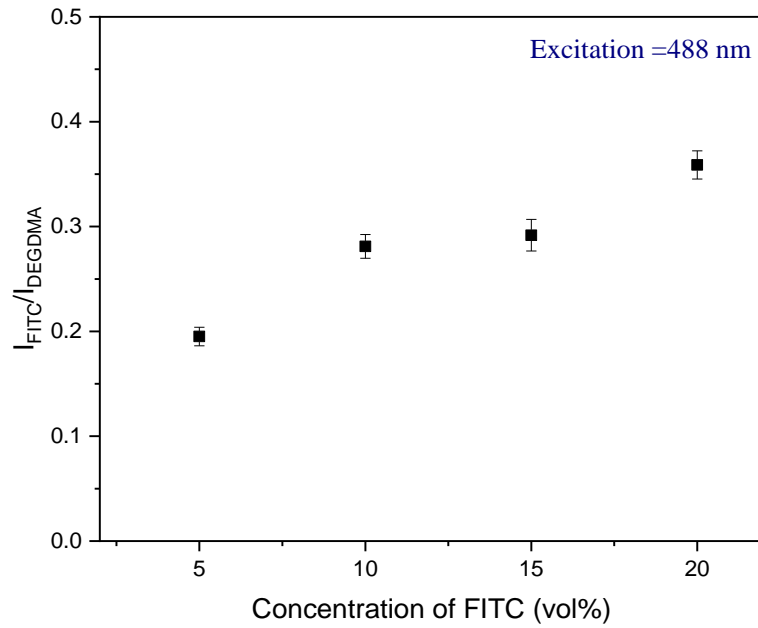
Figure 37: Intensity ratio of luminescent FITC/DEGDMA composite microparticles prepared from 5 vol% DEGDMA monomer with different concentrations of FITC. The irradiation dose was 10 kGy.

The performance of the fabricated fluorescent FITC/DEGDMA microparticles prepared by gamma-induced polymerization was tested with the LSFM system built by me. First of all, after the alignment of the system, standard fluorescent polystyrene (FPS) microparticles of different sizes were used to calibrate the system. Figure 38 shows the image stacks recorded by the LSFM system for FPS with sizes of 2 and 6 µm along different detection lengths (depths) around the focal plane. A 632 nm excitation wavelength was used for illumination of the particles with a 650 nm long-pass filter.

Figure 38a explains the Gaussian mode of laser intensity predicted in the LSFM of the FPS microparticles. This means the fluorescence emission/scattered light from the microparticles sample will have a maximum in the focal plane, which makes the image of the sample as clear as possible. In contrast, the intensity of the light sheet decreases gradually outside the focal plane on the left and right sides along the detection axis. While Figure 38b depicts the sample moving along the Z-axis, this alters the clarity of the image on the CCD camera. In other words, the focal point of the specimen is at Z= 0, where the image is bright, while Z- & Z+ represent the movement of the sample up and down from the focal point, respectively.
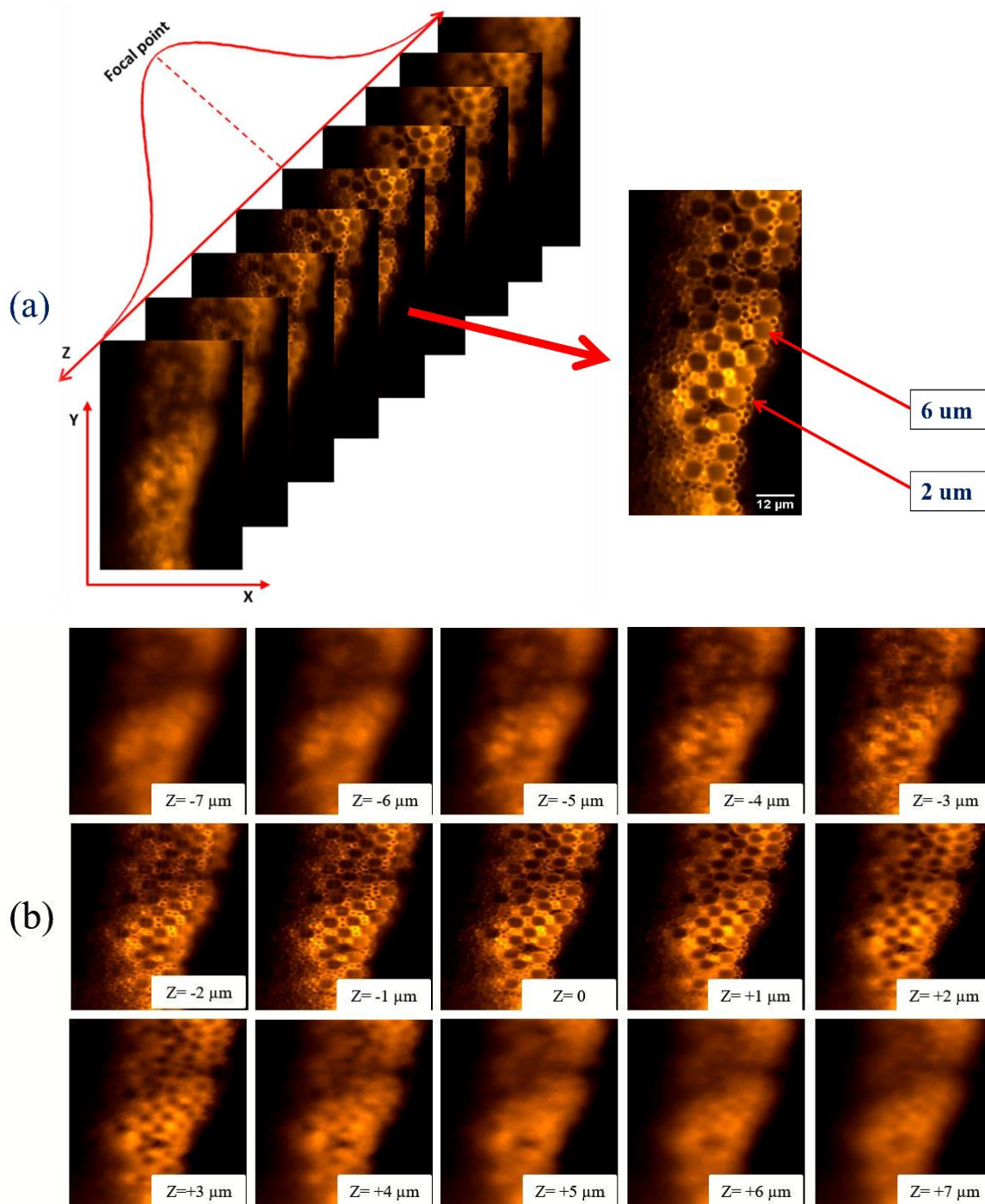
Figure 38: Gaussian-mode of laser intensity predicted in the LSFM of the FPS microparticles sample (a) and image stack of FPS microparticles with sizes of 2 and 6 µm recorded along the detection length (b). The excitation laser was 633 nm. All the images are of the same magnification.

On the other hand, Figure 39 shows the optical microscopy and LSFM images recorded on the FITC/DEGDMA composite microparticles prepared by gamma polymerization. These microparticles were fabricated from 5 vol% DEGDMA monomer with 20 vol% FITC content and the irradiation dose was 10 kGy. Based on the excitation-emission spectra (Figure 36b), a

488 nm excitation wavelength and a 500 nm fluorescent emission filter were used. It seems there is a good agreement with the fluorescent emissions detected by the built LSFM system with PL spectra. This may prove the sensitivity of the constructed LSFM system for imaging fluorescent particles even with a size of less than a micron, which may be in good agreement with the calculated lateral and axial resolution for the LSFM system (0.5 µm lateral and 0.7 µm axial resolution, according to Eqs. (1) and (2)).
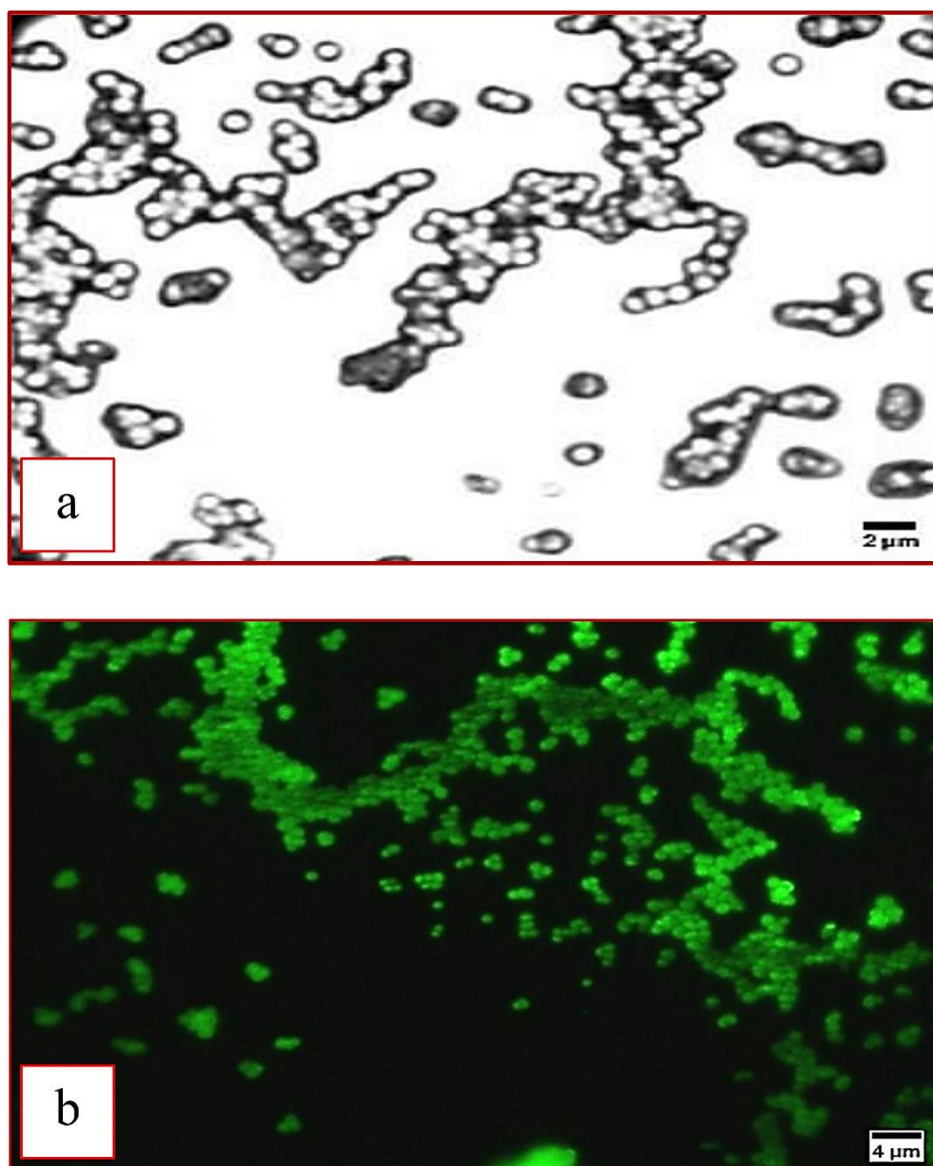

Figure 39: (a) Optical microscopy and (b) LSFM images of fluorescent FITC/DEGDMA composite microparticles prepared from 5 vol% DEGDMA monomer with 20 vol% FITC content under irradiation dose of 10 kGy. The LSFM has been performed with 488 nm excitation laser.

In conclusion, fluorescent FITC/DEGDMA microparticles were synthesized successfully by gamma radiation-initiated precipitation. It was found that the addition of the dye to the monomer mixture increases the size and distorts the spherical shape of the particles. The FITC emission peaks were observed in the photoluminescence spectrum of the composite, with an extended excitation wavelength range. Moreover, the LSFM imaging of fluorescent FITC/DEGDMA microparticles showed good agreement with PL spectra.

4.3. Nanogold-capped poly(DEGDMA) microparticles as surface-enhanced Raman scattering substrates for DNA detection

This work is aimed at the fabrication of polymeric microparticles decorated with gold nanoparticles and the investigation of their SERS enhancement properties. Firstly, gamma radiation-initiated polymerization [T2] has been used to prepare polymeric microparticles of DEGDMA monomer and ethyl propionate solvent then the prepared particles were functionalized with gold nanoparticles.
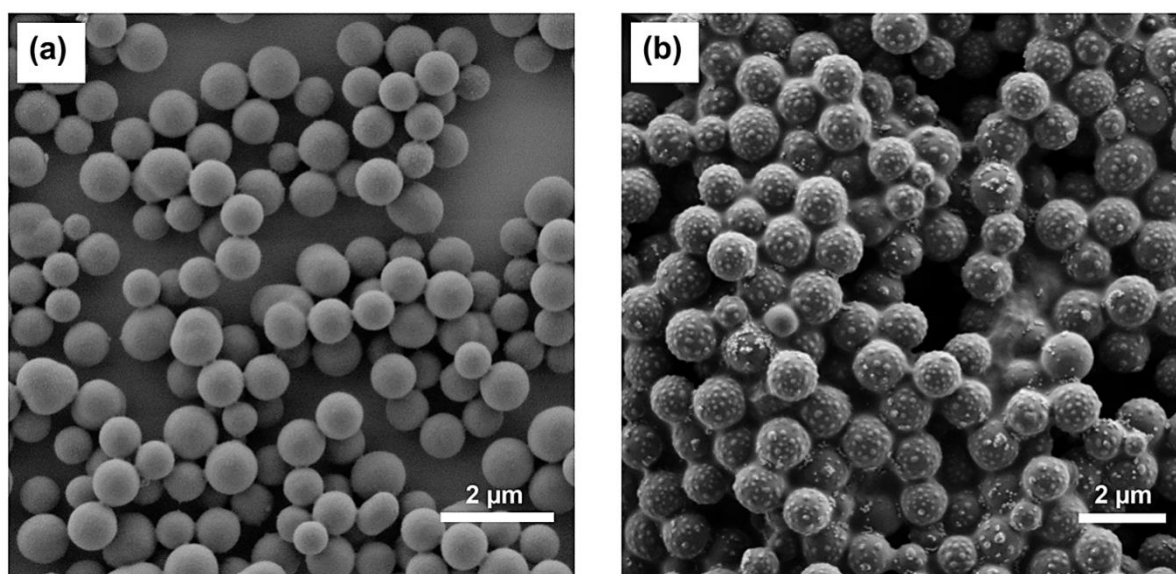
Figure 40: SEM images of poly(DEGDMA) microparticles (a) without AuNPs and (b) decorated with AuNPs. The polymeric particles were prepared from 5 vol% DEGDMA monomer and 95 vol% ethyl propionate solvent, irradiated with 10 kGy.

Figure 40a shows the SEM image of polymeric microparticles prepared from 5 vol% DEGDMA monomer according to the method detailed in Section 3.2. The micrometer-sized particles are of spherical shape, and the average particle size was found to be about 0.9 µm. Particles from the same batch, but after functionalization with thiol group and decoration with gold nanoparticles are shown in Figure 40b, the SEM image shows a uniform coverage of the

microparticle surface with AuNPs. The 40 nm gold nanoparticles seem to be aggregated, and the clusters are localized on the polymer surface in a 100-200 nm distance from each other. According to the SEM pictures, the average size of the aggregated gold nanoparticles is 120 ± 27 nm.
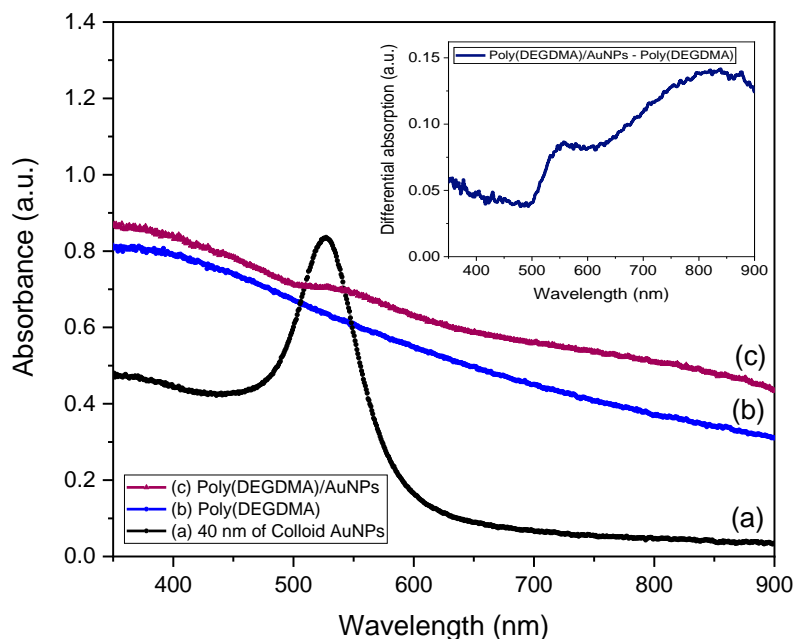

Figure 41: UV-Visible absorption spectra of (a) colloid AuNPs with 40 nm diameter, (b) poly(DEGDMA) microparticles, (c) poly(DEGDMA) microparticles decorated with AuNPs, and the inset shows differential absorption spectrum of [poly(DEGDMA)/AuNPs – poly(DEGDMA)].

UV-Vis absorption spectroscopy was used to determine the spectral position of the plasmon resonance of poly(DEGDMA)/AuNP composite. Figure 41 compares the absorption spectra of the colloidal AuNPs with 40 nm size and poly(DEGDMA) microparticles with and without AuNPs decoration. It is clear that the dominant absorption band of colloidal gold nanoparticles located at 525 nm is related to the plasmon excitation [146]. The non-coated poly(DEGDMA) suspension is semitransparent; no definite absorption peak was detected in the visible region. Its absorption has a maximum at 360 nm and decreases towards higher wavelengths. Similar general behavior can be seen for the decorated poly(DEGDMA) microparticles, however, small but recognizable bands appear between 500 and 650 nm, as well as between 700 and 900 nm in the absorption spectrum. (These are more visible in the inset of Figure 40 showing the differential absorption of the microparticles suspension with gold decoration and without it). These features are related to the gold NPs attached to the

microparticle surface. The maximum of the first plasmon resonance peak is shifted towards higher wavelengths (to 550 nm), which can be related to the aggregation and to the change in the dielectric properties of the surrounding medium of NPs, caused by the presence of the polymer matrix [147,148]. The appearance of the second plasmon peak above 700 nm is definitely due to the formation of nanoparticle aggregates.
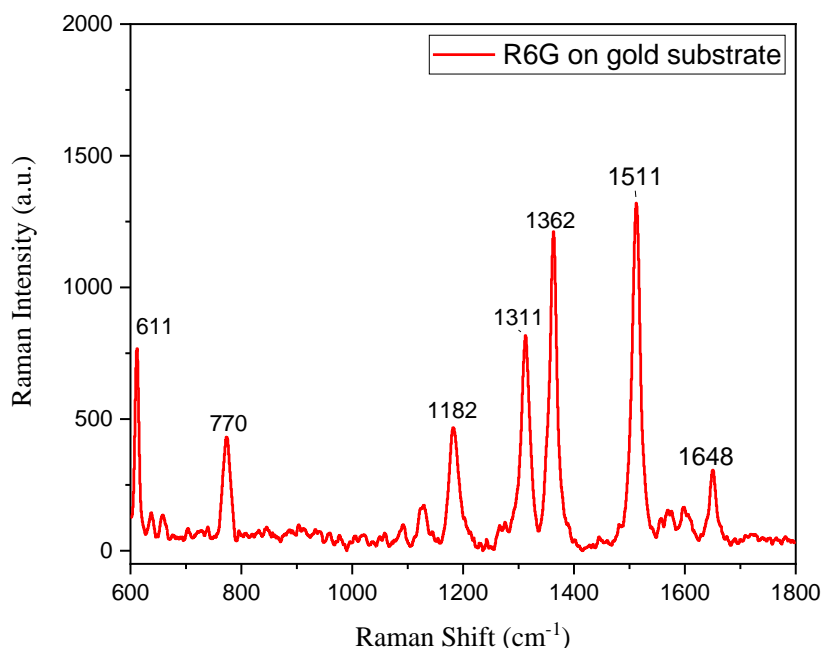

Figure 42: Raman spectrum of R6G solution on a flat gold substrate. The measurement conditions were 5 mmol/L concentration, 785 nm excitation, and 10 s exposure time.

To evaluate the SERS performance of AuNPs decorated polymer microparticles R6G was used as an analyte for Raman spectroscopic investigations. Firstly, the Raman spectrum of pure R6G solution with 5 mmol/L concentration was measured as a reference on a flat gold substrate with 785 nm excitation laser and 10 s exposure time. According to Figure 42, many peaks can be identified in the measured spectrum of R6G, including the medium intensity peak at 611 cm^{-1} to the band with highest intensity at 1511 cm^{-1}. The Raman bands at 611, 770, and 1182 cm^{-1} can be attributed to the C-C-C ring in-plane vibration mode, the C-H out of-plane bending mode, the C-H in-plane bending mode of the R6G molecule, respectively. The band at 1311 cm^{-1} results from the N-H in-plane bending mode, while those at 1362, 1511, and 1648 cm^{-1} are due to in-plane C-C stretching mode of the R6G molecule [121].

In the next step, 5 µL of bare and AuNP decorated poly(DEGDMA) microparticle suspension was deposited on silicon substrate by drop-casting and left to dry at room temperature for 24 hours. Then, the SERS spectra recorded on poly(DEGDMA) microparticles decorated with AuNPs were evaluated using 2 µL aqueous solution of R6G molecules with a concentration of 5 mmol/L. Figure 43 compares the normal Raman and SERS spectra of R6G recorded on poly(DEGDMA) microparticles and poly(DEGDMA)/AuNPs composite, respectively. As a result of the attachment of AuNPs to the surface of poly(DEGDMA) microparticles (red curve in Figure 43) a giant enhancement for all Raman bands can be observed, which is especially spectacular for peaks at 1311. 1362, 1511, and 1648 cm^{-1}. In other words, the signal of R6G was enhanced due to the formation of SERS "hot spots" on the polymeric microparticles composite.
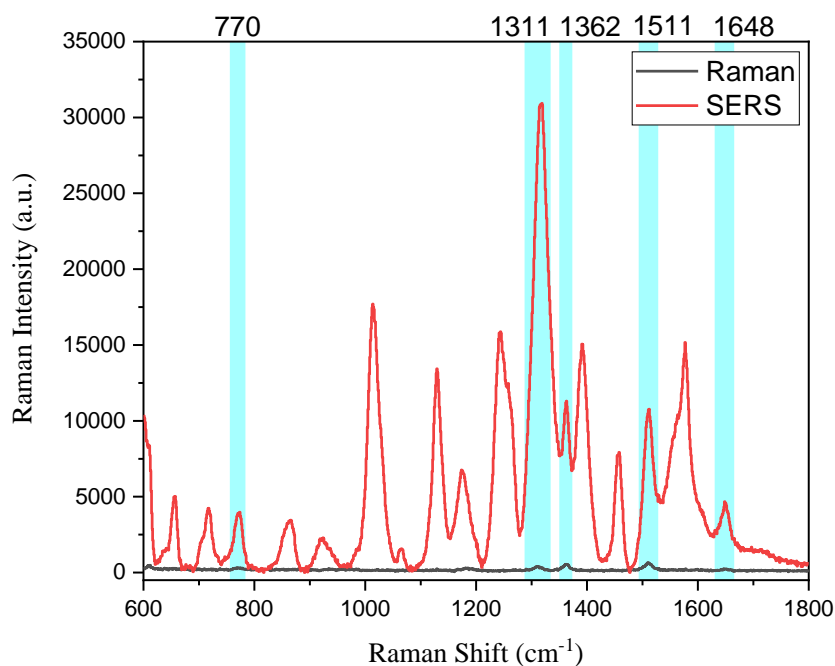
Figure 43: Normal Raman and SERS spectra of R6G solution with a concentration of 5 mmol/L applied on poly(DEGDMA) and poly(DEGDMA)/AuNPs composite, respectively. The spectra were recorded with 785 nm excitation and exposure time of 10 s. [The highlighted light blue bars indicate the Raman bands of R6G].

The SERS spectra of 5 mmol/L R6G dye were investigated with different excitation wavelengths as well. Figure 44 compares the Raman spectrum of the dye on poly(DEGDMA)/AuNPs microparticles composite with 532, 633, and 785 nm excitations. Throughout the measurements, the same laser power of 0.2 mW was used for all three

wavelengths. It can be seen that the 785 nm excitation gives higher enhancement than 632 nm. On the other hand, no Raman scattering can be detected with 532 nm. Based on the above results, it can be concluded that the 785 nm excitation is the most appropriate to excite SERS on of the prepared microparticle composites. This wavelength is the closest to the plasmon absorption maximum of the samples (Figure 41 insert).
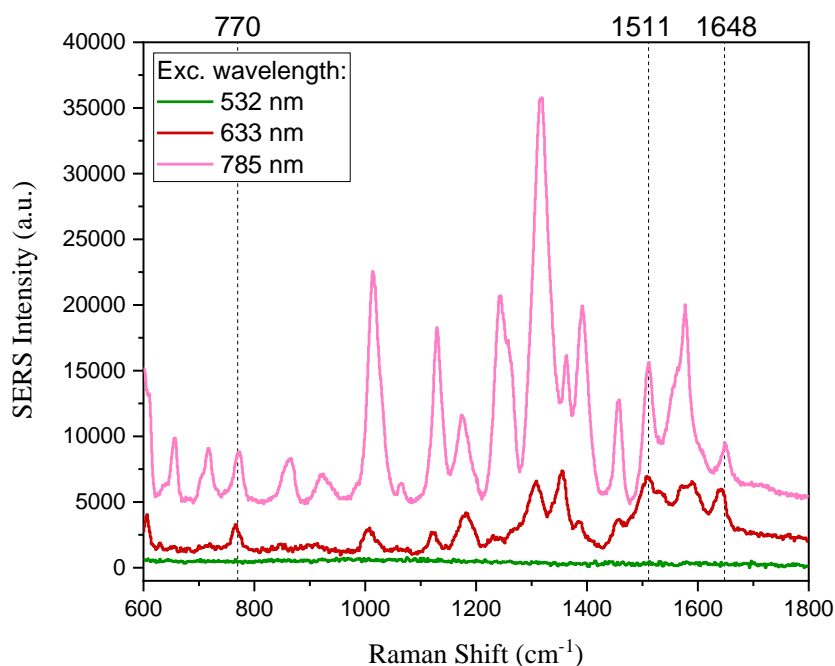
Figure 44: SERS spectra of 5 mmol/L R6G dye dripped on poly(DEGDMA)/AuNPs composite measured with 532, 633, and 785 nm excitations. [The dashed lines characterize the Raman bands of R6G].

SERS spectra of R6G dye for concentrations between 0.02 and 5 mmol/L were measured to assess the sensitivity of the poly(DEGDMA)/AuNPs composite SERS substrate. As shown in Figure 45a the intensity of the Raman peaks depends on the concentration of R6G but can be quite well detected even for the lowest concentration of the analyte. The main R6G peaks and their concentration dependence is shown in Figure 45b. The SERS intensity increases with the concentration of the dye and the enhancement effect shows a tendency of $I_{1311} > I_{770}$ for all the measured concentrations, while the enhancement of I_{1362}, I_{1511}, and I_{1648} are similar for the concentrations of 0.1, 1, 3, and 5 mmol/L.

Figure 45c presents the change of the 1311 cm^{-1} peaks intensity as a function of R6G concentration. The inset shows that the intensity dependence has a nearly linear behavior on the logarithmic scale.
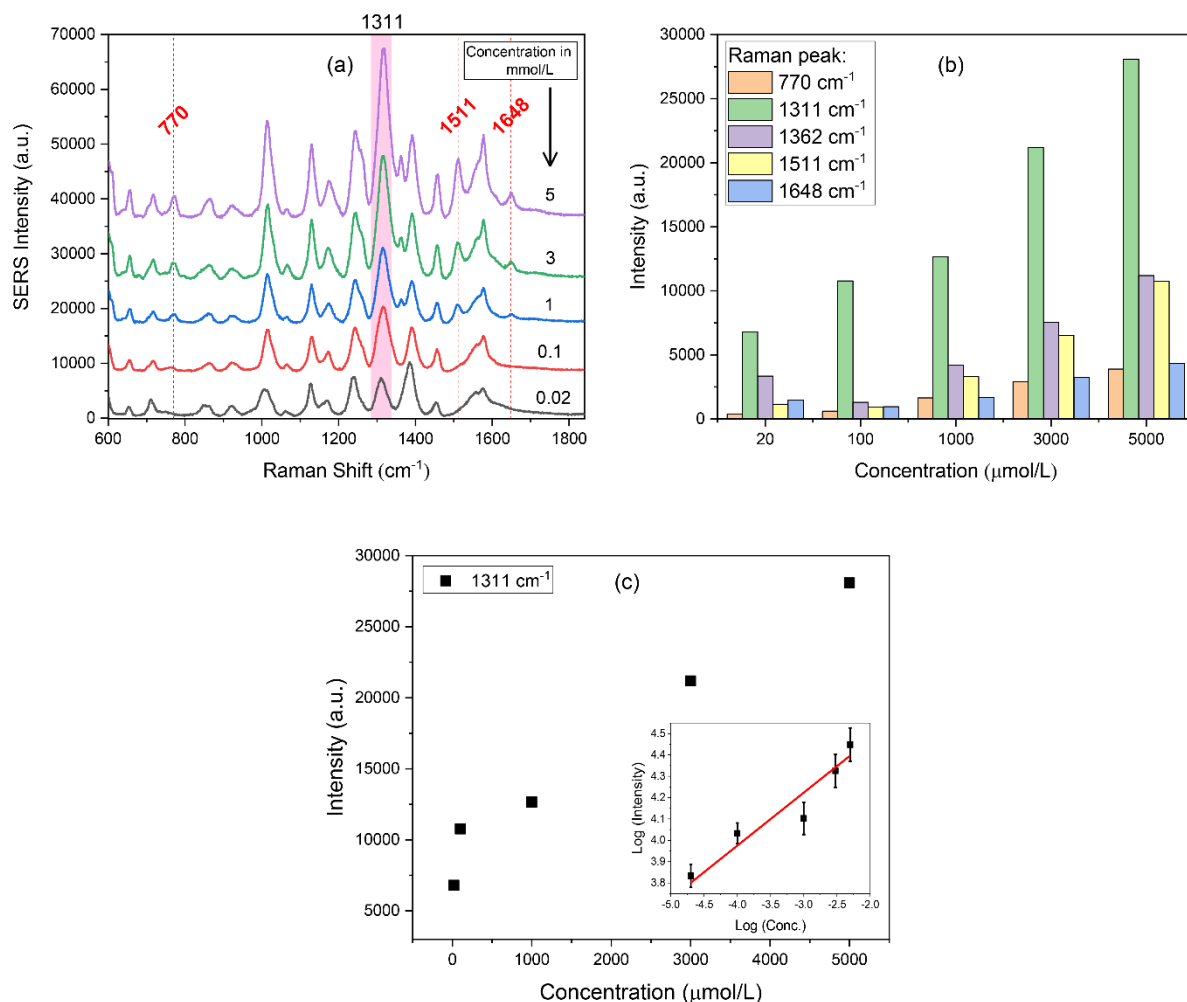
Figure 45: (a) SERS spectra of R6G dye solutions with different concentrations between 0.02 and 5 mmol/L deposited onto poly(DEGDMA)/AuNPs composite, (b) the intensity of the 770, 1311, 1362, 1511, and 1648 cm^{-1} Raman bands as a function of R6G concentration, and (c) variation of peak intensities of the 1311 cm^{-1} band as a function of the R6G concentration. The inset shows the same on a logarithmic scale (3 measurements were performed on each sample).

To evaluate the SERS capability of poly(DEGDMA)/AuNPs composite, the analytical enhancement factor was calculated for the proposed composite at 1311 cm^{-1} peak by using Eq. (21), the normal Raman spectrum of R6G (Figure 43), and the SERS spectrum corresponding to the smallest detectable concentration of R6G (Figure 45). The obtained value for AEF is 4.4 * 10^3 (I_{SERS} = 6737 (a.u.), C_{SERS} = 0.02 mmol/L, I_{RS} = 379 (a.u.), and C_{RS} = 5 mmol/L).

Figure 46: (a) SERS spectra of R6G of 5 mmol/L concentration recorded in five random points (and 3 measurements in each point) on the poly(DEGDMA)/AuNPs composite sample surface and (b) comparison of the Raman intensities of the 1511 cm^{-1} peak.

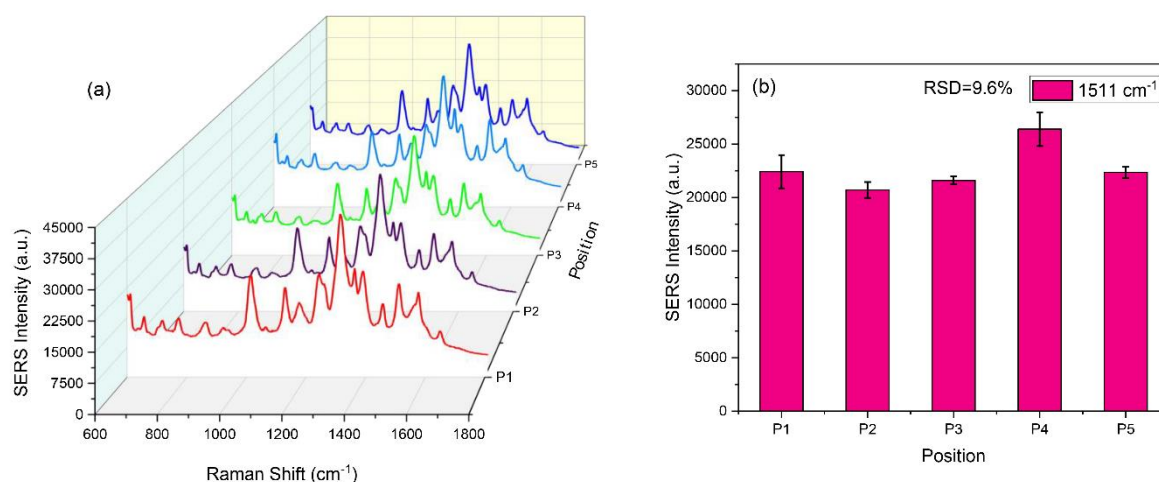To evaluate the uniformity of the poly(DEGDMA)/AuNPs SERS substrate, Raman spectra were measured randomly at different points on the sample surface. Figure 46a displays SERS spectra of R6G with 5 mmol/L concentration at five different points. The intensity of the Raman peaks of the analyte shows a small variation (Figure 46b), which indicates good uniformity of the distribution of the gold nanoparticles and the poly(DEGDMA) microspheres on the substrate (as also shown in the SEM images, Figure 40).

On the other hand, more representative information for the prepared polymer composite was reported, SERS spectra of poly(DEGDMA)/AuNPs composite as a function to the excitation power were investigated. Figure 47a shows the power-dependent SERS spectra of 5*10^{-3} mol/L R6G measured at room temperature. Figure 47b shows the changes of intensity for 1511 and 1135 cm^{-1} peaks as a result of applying different excitation laser powers. In Figure 47b, it is clearly seen that there are two regimes for the peak intensity behavior for both studied Raman bands. In the first regime, a noticeable linear increase can be observed with increasing the laser power up to 0.4 mW. AuNPs create local hot spots that may generate strong electromagnetic fields in the result of which the Raman signal is enhanced[149]. Further increase of the excitation laser power leads to a gradual decrease of the peak intensities. It may indicate a noteworthy rise of the local temperature at the vicinity of hot spots that could quench the Raman scattering process of the analyte [150–152].
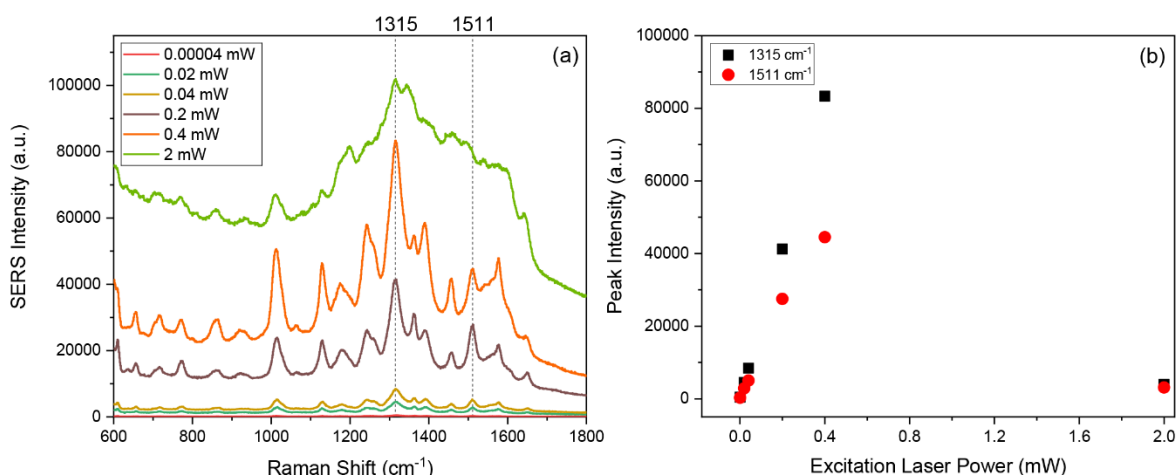
Figure 47: (a) Power-dependent SERS spectra of $5*10^{-3}$ mol/L R6G applied on poly(DEGDMA)/AuNPs composite and (b) peak intensity at 1511 cm^{-1} as function of excitation laser power. The measurements were performed using 785 nm laser with five different powers 0.00004 mW, 0.02 mW, 0.04 mW, 0.2 mW, 0.4 mW, and 2 mW.
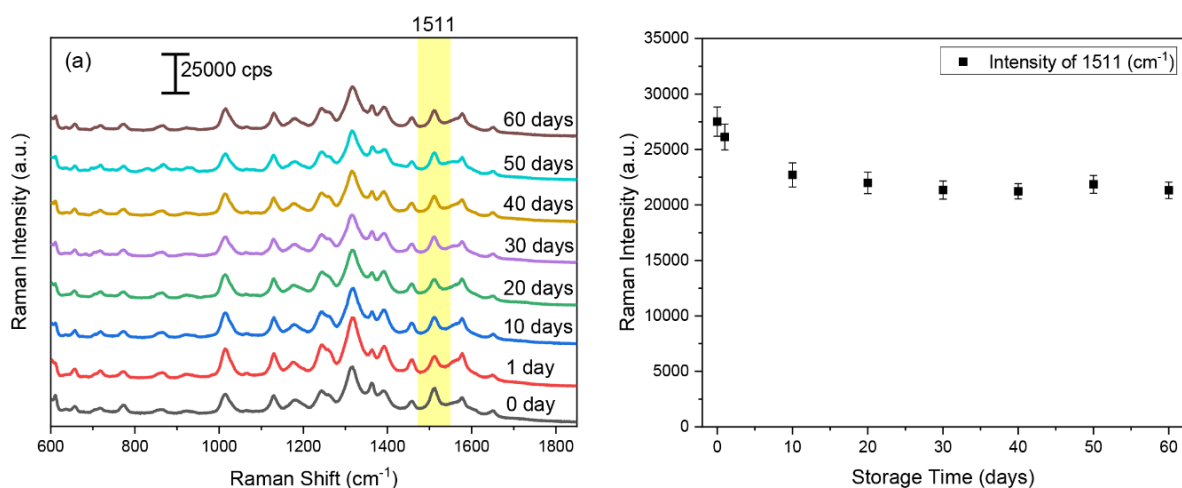
Figure 48: (a) SERS spectra of 5 mmol/L R6G deposited onto poly(DEGDMA)/AuNPs composite collected after storage times of 0 - 60 days, and (b) SERS intensity of the 1511 cm^{-1} R6G SERS peak as a function of storage time.

Furthermore, the aging and temporal stability of the SERS substrates is another characteristic parameter, important for the applications. Figure 48a shows the SERS spectra of 5 mmol/L R6G deposited onto poly(DEGDMA)/AuNPs composite as a function of the time, starting from a fresh sample till 60 days with 785 nm laser excitation. The spectra are very similar, and no significant changes can be observed in the spectrum. The variation of the intensity of the SERS peak at 1511 cm^{-1} with time is shown in Figure 48b. This is some 20% decrease in the intensity in the first 10 days, but it reaches a plateau after that.

As an application, the SERS performance of poly(DEGDMA)/AuNPs was evaluated by using probe- and target-DNA molecules that form a specific sequence from the parasite Giardia lamblia (the β-giardin gene) [153]. SERS measurements of DNA were performed at 785 nm excitation wavelength on poly(DEGDMA)/AuNPs composite sample with an acquisition time of 5 s and accumulations of 5. Figure 49 shows the obtained SERS spectra of DNA attached to poly(DEGDMA)/AuNPs composite. The detected peaks are in good agreement with Raman bands associated with the bases (adenine (A), cytosine (C), guanine (G), and thymine (T)) or the sugar-phosphate backbone (deoxyribose) reported in the literature [154–158]. Table 8 shows the assignments of the main Raman bands of DNA.
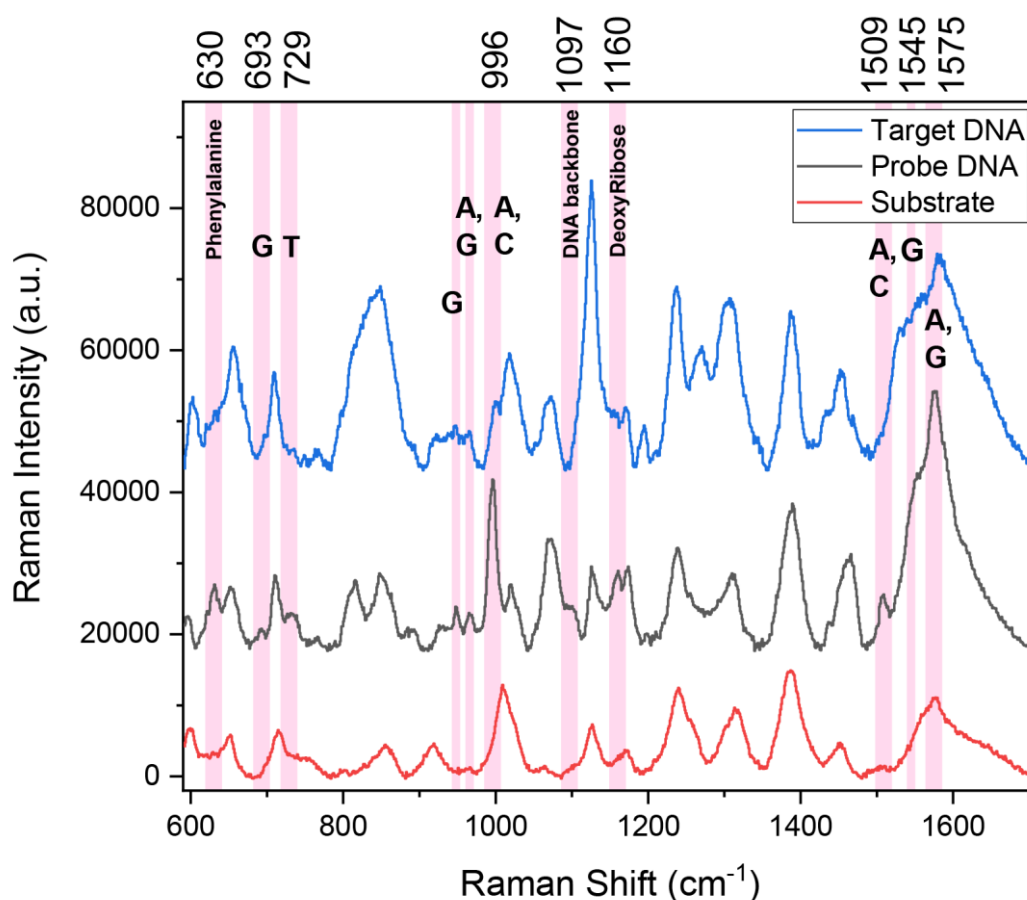
Figure 49: SERS spectra of DNA applied on poly(DEGDMA)/AuNPs composite. The excitation was 785 nm, exposure time 5 s, and accumulations 5.

Figure 49 presents the Raman spectra of the DNA are different that is might be due to the used protocol of the DNA measurements included the preparation of the probe-DNA sample on the poly(DEGDMA)/AuNPs by the immobilization of single stranded DNA on the gold surface, followed by the addition of the target-DNA to the solution. The spectra recorded for the two

samples are different because of the differences in the sequences. The base sequence of the probe-DNA is CGTACATCTTCTTCCTTTTT-[ThiC6]; while that of the target-DNA is AGGAAGAAGATGTACGACCA. There are more T and C oligos in the probe-DNA, while the target-DNA is dominated by A and G oligos, and this is reflected in the Raman spectra as well.

Table 8: Raman bands of DNA and their assignments. Adenine (A), cytosine (C), guanine (G), thymine (T), and the sugar-phosphate backbone (Deoxyribose).

Raman shift (cm^{-1})	Assignment	Reference
630	Phenylalanine	[154]
693	G	[155]
729	T	[156]
948	G	[157]
966	A, G	[157]
996	A, C	[157]
1097	DNA backbone	[156]
1160	Deoxyribose	[156]
1509	A, C	[155]
1545	G	[155,157]
1575	A, G	[158]

In conclusion, a method has been developed to fabricate SERS substrate consisting of DEGDMA polymer microparticle support decorated with gold nanoparticles on the surface. The comparative Raman study on SERS-active and non-SERS-active microparticles revealed that the intensities of the rhodamine 6G peaks were significantly increased due to localized plasmon resonance caused by AuNPs linked to polymeric microspheres in the SERS-active microparticles. The composite showed good SERS sensitivity compared with free AuNPs, with a SERS EF value of $4.4*10^3$ by detecting 20 µmol/L concentration of the R6G dye. The poly(DEGDMA)/AuNPs substrate was demonstrated to be stable for more than 60 days in SERS experiments. The SERS performance of the substrate was demonstrated with the application to a DNA sequence, which also proved the possibility of utilizing the poly(DEGDMA)/AuNP substrate for biosensing applications.

5. Summary

Spectroscopy is an interesting research field because of its wide applications areas. Therefore, in my doctoral thesis, I was centering on the preparation and laser spectroscopic characterization of polymeric microparticles for different applications. Firstly, I prepared microparticles and estimated their optimal preparation conditions, then developed them to fabricate fluorescent microparticles to be used in imaging. Secondly, I obtained a new composite of polymer microparticles covered with gold nanoparticles to be used in surface-enhanced Raman spectroscopic applications to detect certain biomolecules.

The first step of my doctoral research work was to study the reaction kinetics of DEGDMA monomer in different solvents upon gamma irradiation with different doses and to determine the dose dependence of the degree of conversion with Raman spectroscopy and mass difference measurements. Both methods showed good agreement in the DC, therefore, the Raman method was found to be an excellent method of choice to determine the conversion rate of the polymer by a non-contact, non-destructive and, in terms of realization, simple manner, having the potential for real-time remote monitoring in the irradiation chamber. The results were fitted using the Avrami equation, and the observed variations in reaction rate were attributed to the fact that the DEGDMA polymerization process behaves differently in alcohols and other solvents, as determined by their solubility values.

In the second phase, I synthesized polymeric microparticles of DEGDMA monomer with ethyl propionate solvent by gamma radiation-initiated precipitation polymerization firstly, then FITC dye was incorporated into the polymer matrix to form luminescent FITC/DEGDMA microparticles. The morphology, size, bonding configuration, and emission properties of the microparticles were investigated by using SEM, Raman, PL spectroscopy, and LSFM, respectively. It was found that the structure of the FITC was preserved after the irradiation and the obtained microparticles have good emission properties.

In the last part of my study, I have developed the method to synthesize SERS enhanced substrate by attaching gold nanoparticles to polymeric microparticles prepared by gamma radiation-initiated polymerization. Firstly, I fabricated poly(DEGDMA)/AuNPs composite and investigated their enhancement efficiency as a SERS substrate using R6G the common fluorescent probe dye. Secondly, the practical applications of proposed SERS substrates were tested by DNA strand-specific to the parasite Giardia lamblia (the β-giardin gene).

The new scientific results achieved during my doctoral research work are summarized in the following points:

1- I studied the polymerization kinetics of diethylene glycol dimethacrylate (DEGDMA) upon gamma radiation in different solvents with Raman spectroscopy and mass difference measurements [T1].

    (i) I found that the rate of polymerization strongly depends on the type of the solvent, and the process is faster in alcohols than in acetone, ethyl acetate, and ethyl propionate. This behavior was explained by the difference in the solubility parameters of the solvents.

    (ii) By the detailed analysis of the Raman spectrum of DEGDMA with irradiation dose, I showed that there are intact C=C bonds in the polymer structure even well after reaching the plateau in the conversion curve. This indicates the presence of partially polymerized or entrapped monomer molecules in the formed structure. The C=C Raman peak intensity was found to correlate with the type of the solvent and the reaction rate of polymerization, being smaller for alcohols than for acetone, ethyl acetate, and ethyl propionate.

2- I developed a method to synthesize fluorescent microparticles by incorporating fluorescein isothiocyanate isomer-I (FITC) dye into the diethylene glycol dimethacrylate (DEGDMA) polymer network by gamma radiation-initiated polymerization [T2, T4, T5].

    (i) I found that the addition of the dye to the DEGDMA monomer mixture increases the size and alters the spherical form of the resulting particles.

    (ii) I demonstrated that the emission properties of the obtained micro-objects are in good agreement with those of the FITC, but with an extended excitation wavelength range, that can be attributed to the interconnection between the FITC molecules and the polymer structure.

3- I developed a method to synthesize surface-enhanced Raman spectroscopic (SERS) substrate by attaching gold nanoparticles (AuNP) to the polymeric diethylene glycol dimethacrylate (DEGDMA) microparticles prepared by gamma radiation-initiated polymerization [T3, T6].

(i) I showed that the DEGDMA/AuNP composite has two plasmonic peaks in the absorption spectrum. The 550 nm band can be attributed to single gold nanoparticles, and the 700 nm one to their aggregates.

(ii) By studying the surface enhancement properties of the substrate with Rhodamine 6G (R6G) molecule I found that for 785 nm excitation wavelength its enhancement factor is $4.4*10^3$ and the detection limit with 20 µmol/L, and it shows good long-time stability performance over 2 months in SERS experiments. I proved the SERS substrate's biosensing capability through the detection of DNA sequences.

Acknowledgments

All praise be to Allah, the all-knowing who does not forget who remembers him.

My deepest gratitude goes to my thesis supervisor, Dr. Miklós Veres, for his continuous support, helpful advice, motivation, and guidance, for the creation of the research infrastructure. This support helped me along the way to be on the right track and to take steady steps in scientific research. Additionally, I gained a wealth of information and life experience from him.

Many thanks to the members of our research group, Dr. László Himics, Dr. Tamás Váczi, Dr. Roman Holomb, and Dr. István Rigó for their help with my research. Special thanks to Ágnes Szokol for her help with many administrative issues.

I am grateful to Dr. László Péter for his help with SEM images. I wish to thank Zoltán Papp for irradiation of the samples. Many thanks to Dr. Szilvia Kugler and Dr. Attila Tibor Nagy.

A special thanks to Dr. Aladár Czitrovszky, former director of SZFI, for his encouragement during my study in Hungary.

Thanks to the Hungarian Government, The Ministry of Human Capacities, Tempus Public Foundation (TPF) for granting me the Ph.D. scholarship under the program of Stipendium Hungaricum (SH).

I am thankful to the Iraqi government, Ministry of Higher Education and Scientific Research, University of Misan, College of Medicine, for granting me the scholarship approval in 2017.

I would like to thank Prof. Dr. Haitham L. Saadon for his moral support.

My gratitude also goes to my friends: Dr. Mohammed Talib, Eng. Haidar Adnan, Dr. Ahmed Jasim, Dr. Ahmed Mohsin, Dr. Ahmed Dhahir, and Dr. Zaid Isam for their moral support.

Furthermore, I would like to thank my family members for motivating me to achieve my goals. Many thanks to my brother, Dr. Hassan Hadi Mahmood, for his great support and encouragement, and I thank my mother for her prayers to Allah to help me. I have not forgotten that the biggest support in my life goes to my dead father.

Last but not least, I want to thank my strong wife for her immeasurable patience, support, and love.

Malik Hadi Mahmood

Szeged 2021

Publications related to the Ph.D. thesis

[T1]   **Malik H. Mahmood**, László Himics, Tamás Váczi, István Rigó, Roman Holomb, Barbara Beiler, Miklós Veres; "**Raman spectroscopic study of gamma radiation-initiated polymerization of diethylene glycol dimethacrylate in different solvents**", (Journal of Raman Spectroscopy, 52 (**2021**) 1735–1743), doi.org/10.1002/JRS.6207   **Q2**   **IF: 3.133**

[T2]   **Malik H. Mahmood**, László Himics, László Péter, Péter Baranyai, Miklós Veres; "**Characterization of luminescent monodisperse microparticles prepared by gamma radiation-initiated polymerization**", (Optical Materials, 108 (**2020**) 110209), doi.org/10.1016/j.optmat.2020.110209   **Q1**   **IF: 3.080**

[T3]   **Malik H. Mahmood**, Ali Jaafar, László Himics, László Péter, István Rigó, Shereen Zangana, Attila Bonyár, Miklós Veres; "**Nanogold-capped poly(DEGDMA) microparticles as surface-enhanced Raman scattering substrates for DNA detection**", (Submitted for publication to J. Phys. D: Appl. Phys.),

[T4]   **Malik H. Mahmood**, László Himics, Péter Baranyai, László Péter, Miklós Veres; "**Preparation of luminescent monodisperse microparticles prepared by gamma radiation initiated polymerization**", proceedings of the Annual Conference of the Hungarian Microscopic Society at Siófok, Balaton, May 23-25, pp 2 (**2019**).

[T5]   **Malik H. Mahmood**, László Himics, László Péter, Péter Baranyai, Miklós Veres; "**Luminescent monodisperse microparticles prepared by gamma radiation-initiated polymerization**", proceedings of the 14th Hungarian Aerosol Conference at Visegrád, October 2-4, pp 55-57 (**2019**).

[T6]   **Malik H. Mahmood**, Ali Jaafar, László Himics, László Péter,Ágnes Nagyné Szokol,István Rigó, Shereen Zangana, Attila Bonyár, Miklós Veres; "**Surface-enhanced Raman scattering substrates for DNA detection based on nanogold-capped poly(DEGDMA) microparticles**", proceedings of the 25th Saratov Fall Meeting Conference, Laser Physics and Biophotonics, at Saratov, Russia, September 27- October 1, (**2021**).

Further scientific publications

[F1]   Ali Jaafar, **Malik H. Mahmood**, Roman Holomb, László Himics, Tamás Váczi, Anton Y. Sdobnov, Valery V. Tuchin, and Miklós Veres; "**Ex-vivo confocal Raman microspectroscopy of porcine skin with 633/785-NM laser excitation and optical clearing with glycerol/water/DMSO solution**", (Journal of Innovative Optical Health Sciences, (**2021**) 2142003),
doi.org/10.1142/S1793545821420037   **Q1   IF: 1.770**

[F2]   Roman Holomb, Oleksandr Kondrat, Volodimir Mitsa, Alexander Mitsa, David Gevczy, Dmytro Olashyn, László Himics, István Rigó, Ali Jaafar Sadeq, **Malik H. Mahmood**, Tamás Váczi, Aladár Czitrovszky, Attila Csík, Viktor Takáts, Miklós Veres; "**Gold nanoparticle assisted synthesis and characterization of As-S crystallites: scanning electron microscopy, X-ray diffraction, energy-dispersive X-ray and Raman spectroscopy combined with DFT calculations**", (Journal of Alloys and Compounds), (**2021**),
doi.org/10.1016/j.jallcom.2021.162467   **Q1   IF: 5.316**

[F3]   Miklós Veres, László Himics, István Rigó, Roman Holomb, **Malik H. Mahmood**, Péter Baranyai and Tamás Váczi, "**Az indukált Raman-szórás alkalmazása aeroszolok és más mikroobjektumok vizsgálatára**", proceedings of the 14th Hungarian Aerosol Conference at Visegrád, October 2-4, (**2019**).

[F4]   Miklós Veres, László Himics, István Rigó, Sára Tóth Borossáné, Roman Holomb, **Malik H. Mahmood** and Tamás Váczi, "**Indukált Raman-szórás femto-szekundumos lézerrel**", in Kvantumelektronika (**2018**).

References

[1]   M. Lengyel, N. Kállai-Szabó, V. Antal, A.J. Laki, I. Antal, Microparticles, Microspheres, and Microcapsules for Advanced Drug Delivery, Scientia Pharmaceutica. 87 (2019) 20. https://doi.org/10.3390/scipharm87030020.

[2]   L. Agüero, D. Zaldivar-Silva, L. Peña, M.L. Dias, Alginate microparticles as oral colon drug delivery device: A review, Carbohydrate Polymers. 168 (2017) 32–43. https://doi.org/10.1016/j.carbpol.2017.03.033.

[3]   M. Jönsson-Niedziolka, F. Lapierre, Y. Coffinier, S. Parry, F. Zoueshtiagh, T. Foat, V. Thomy, R. Boukherroub, EWOD driven cleaning of bioparticles on hydrophobic and superhydrophobic surfaces, Lab on a Chip. 11 (2011) 490–496. https://doi.org/10.1039/c0lc00203h.

[4]   A. Efimov, A. Lizunova, E. Kalinina, V. Sukharev, V. Ivanov, Electrostatic Aerosol Deposition Method for the Formation of an Ensemble of Monodisperse Particles on a Substrate, Journal of Nano Research. 41 (2016) 53–62. https://doi.org/10.4028/www.scientific.net/JNanoR.41.53.

[5]   M. Liu, X. Zhang, B. Yang, Z. Li, F. Deng, Y. Yang, X. Zhang, Y. Wei, Fluorescent nanoparticles from starch: Facile preparation, tunable luminescence and bioimaging, Carbohydrate Polymers. 121 (2015) 49–55. https://doi.org/https://doi.org/10.1016/j.carbpol.2014.12.047.

[6]   K. Li, B. Liu, Polymer-encapsulated organic nanoparticles for fluorescence and photoacoustic imaging, Chemical Society Reviews. 43 (2014) 6570–6597. https://doi.org/10.1039/C4CS00014E.

[7]   X. Zhang, X. Zhang, B. Yang, Y. Zhang, M. Liu, W. Liu, Y. Chen, Y. Wei, Fabrication of water-dispersible and biocompatible red fluorescent organic nanoparticles via PEGylation of aggregate induced emission enhancement dye and their cell imaging applications, Colloids and Surfaces B: Biointerfaces. 113 (2014) 435–441. https://doi.org/https://doi.org/10.1016/j.colsurfb.2013.09.031.

[8]   X. Zhang, Z. Ma, Y. Yang, X. Zhang, X. Jia, Y. Wei, Fine-tuning the mechanofluorochromic properties of benzothiadiazole-cored cyano-substituted diphenylethene derivatives through D–A effect, Journal of Materials Chemistry C. 2 (2014) 8932–8938. https://doi.org/10.1039/C4TC01457J.

[9]   X. Li, X. Zhang, Z. Chi, X. Chao, X. Zhou, Y. Zhang, S. Liu, J. Xu, Simple fluorescent probe derived from tetraphenylethylene and benzoquinone for instantaneous biothiol detection, Analytical Methods. 4 (2012) 3338–3343. https://doi.org/10.1039/C2AY25564B.

[10]   M. Allen Northrup, T.J. Kulp, S.M. Angel, Application of flourescent particle imaging to measuring flow in complex media, Analytica Chimica Acta. 255 (1991) 275–282. https://doi.org/10.1016/0003-2670(91)80056-Y.

[11]   M. Okubo, T. Nakagawa, Formation of multihollow structures in crosslinked composite polymer particles, Colloid and Polymer Science. 272 (1994) 530–535. https://doi.org/10.1007/BF00653217.

[12]   J. Icha, M. Weber, J.C. Waters, C. Norden, Phototoxicity in live fluorescence microscopy, and how to avoid it, BioEssays. 39 (2017) 1700003. https://doi.org/10.1002/bies.201700003.

[13]   H. Ow, D.R. Larson, M. Srivastava, B.A. Baird, W.W. Webb, U. Wiesner, Bright and Stable Core−Shell Fluorescent Silica Nanoparticles, Nano Letters. 5 (2005) 113–117. https://doi.org/10.1021/nl0482478.

[14]   E. Smith, G. Dent, Modern Raman Spectroscopy: a practical approach, Second Edi, John Wiley & Sons Ltd, 2019.

[15]   R.A. Nyquist, R.O. Kagel, Handbook of infrared and raman spectra of inorganic compounds and organic salts: infrared spectra of inorganic compounds, Academic press, 2012.

[16]   K. Kamarás, A. Pekker, Identification and separation of metallic and semiconducting carbon nanotubes, Oxford Handbook of Nanoscience and Technology: Volume 2: Materials: Structures, Properties and Characterization Techniques. 2 (2010) 141.

[17]   D.W. Shipp, F. Sinjab, I. Notingher, Raman spectroscopy: techniques and applications in the life sciences, Advances in Optics and Photonics. 9 (2017) 315–428. https://doi.org/10.1364/AOP.9.000315.

[18]   I. Rigó, M. Veres, Z. Pápa, L. Himics, R. Öcsi, O. Hakkel, P. Fürjes, Plasmonic enhancement in gold coated inverse pyramid substrates with entrapped gold nanoparticles, Journal of Quantitative Spectroscopy and Radiative Transfer. 253 (2020) 107128. https://doi.org/10.1016/j.jqsrt.2020.107128.

[19]   P.P. Zhang, J. Gao, X.H. Sun, An ultrasensitive, uniform and large-area surface-enhanced Raman scattering substrate based on Ag or Ag/Au nanoparticles decorated Si nanocone arrays, Applied Physics Letters. 106 (2015). https://doi.org/10.1063/1.4906800.

[20]   R. Pilot, R. Signorini, C. Durante, L. Orian, M. Bhamidipati, L. Fabris, A review on surface-enhanced Raman scattering, Biosensors. 9 (2019). https://doi.org/10.3390/bios9020057.

[21]   Y. Cao, M. Lv, H. Xu, F. Svec, T. Tan, Y. Lv, Planar monolithic porous polymer layers functionalized with gold nanoparticles as large-area substrates for sensitive surface-enhanced Raman scattering sensing of bacteria, Analytica Chimica Acta. 896 (2015) 111–119. https://doi.org/10.1016/j.aca.2015.09.018.

[22]   L. Chen, H. Yan, X. Xue, D. Jiang, Y. Cai, D. Liang, Y.M. Jung, X.X. Han, B. Zhao, Surface-Enhanced Raman Scattering (SERS) Active Gold Nanoparticles Decorated on a Porous Polymer Filter, Applied Spectroscopy. 71 (2017) 1543–1550. https://doi.org/10.1177/0003702817703293.

[23]   R. Arshady, Microspheres for biomedical applications: preparation of reactive and labelled microspheres, Biomaterials. 14 (1993) 5–15. https://doi.org/10.1016/0142-9612(93)90015-T.

[24]   Q. Zhang, Y. Han, W.-C. Wang, L. Zhang, J. Chang, Preparation of fluorescent polystyrene microspheres by gradual solvent evaporation method, European Polymer Journal. 45 (2009) 550–556. https://doi.org/10.1016/j.eurpolymj.2008.11.016.

[25]   G. Ma, H. Yue, Advances in Uniform Polymer Microspheres and Microcapsules: Preparation and Biomedical Applications, Chinese Journal of Chemistry. 38 (2020) 911–923. https://doi.org/https://doi.org/10.1002/cjoc.202000135.

[26]   C.M. Tseng, Y.Y. Lu, M.S. El-Aasser, J.W. Vanderhoff, Uniform polymer particles by dispersion polymerization in alcohol, Journal of Polymer Science Part A: Polymer Chemistry. 24 (1986) 2995–3007. https://doi.org/10.1002/pola.1986.080241126.

[27]   X. Huang, W.J. Brittain, Synthesis and Characterization of PMMA Nanocomposites by Suspension and Emulsion Polymerization, Macromolecules. 34 (2001) 3255–3260. https://doi.org/10.1021/ma001670s.

[28]   Y. Naka, Y. Yamamoto, Preparation of microspheres by radiation-induced polymerization. II. Mechanism of microsphere growth, Journal of Polymer Science Part A: Polymer Chemistry. 30 (1992) 1287–1298. https://doi.org/10.1002/pola.1992.080300706.

[29]   Á. Sáfrány, B. Beiler, K. László, F. Svec, Control of pore formation in macroporous polymers synthesized by single-step γ-radiation-initiated polymerization and cross-linking, Polymer. 46 (2005) 2862–2871. https://doi.org/https://doi.org/10.1016/j.polymer.2005.02.024.

[30]   E. Lempel, Z. Czibulya, S. Kunsági-Máté, J. Szalma, B. Sümegi, K. Böddi, Quantification of Conversion Degree and Monomer Elution from Dental Composite Using HPLC and Micro-Raman Spectroscopy, Chromatographia. 77 (2014) 1137–1144. https://doi.org/10.1007/s10337-014-2647-3.

[31]   A. Santini, V. Miletic, D. Koutsaki, Degree of conversion of three fissure sealants cured by different light curing units using micro-Raman spectroscopy, Journal of Dental Sciences. 7 (2012) 26–32. https://doi.org/https://doi.org/10.1016/j.jds.2012.01.005.

[32]   B. Beiler, Á. Sáfrány, Polymer monoliths synthesized by radiation co-polymerization in solution, Radiation Physics and Chemistry. 76 (2007) 1351–1354. https://doi.org/https://doi.org/10.1016/j.radphyschem.2007.02.030.

[33]   Á. Sáfrány, B. Beiler, Á. Vincze, Radiation polymerization and crosslinking: A viable alternative for synthesis of porous functional polymers, Radiation Physics and Chemistry. 79 (2010) 462–466. https://doi.org/https://doi.org/10.1016/j.radphyschem.2009.09.014.

[34]   M. Grasselli, E. Smolko, P. Hargittai, Á. Sáfrány, From microspheres to monoliths: Synthesis of porous supports with tailored properties by radiation polymerization, Nuclear Instruments and Methods in Physics Research Section B: Beam Interactions with Materials and Atoms. 185 (2001) 254–261. https://doi.org/https://doi.org/10.1016/S0168-583X(01)00839-4.

[35]   G. Odian, Principles of Polymerization, Fourth Edi, John Wiley & Sons, Inc., 2004.

[36]   R. Bongiovanni, S.D. Vacche, A. Vitale, Photoinduced Processes as a Way to Sustainable Polymers and Innovation in Polymeric Materials, Polymers. 13 (2021) 2293. https://doi.org/10.3390/polym13142293.

[37]   J. Kabatc, Z. Kucybała, M. Pietrzak, F. Ścigalski, J. Paczkowski, Free radical

polymerization initiated via photoinduced intermolecular electron transfer process: kinetic study 3, Polymer. 40 (1999) 735–745. https://doi.org/10.1016/S0032-3861(98)00282-1.

[38] B. Beiler, Á. Vincze, F. Svec, Á. Sáfrány, Poly(2-hydroxyethyl acrylate-co-ethyleneglycol dimethacrylate) monoliths synthesized by radiation polymerization in a mold, Polymer. 48 (2007) 3033–3040. https://doi.org/10.1016/j.polymer.2007.04.002.

[39] A. Ashfaq, M.-C. Clochard, X. Coqueret, C. Dispenza, M.S. Driscoll, P. Ulański, M. Al-Sheikhly, Polymerization reactions and modifications of polymers by ionizing radiation, Polymers. 12 (2020) 2877. https://doi.org/10.3390/polym12122877.

[40] C. Menchaca, A. Álvarez-Castillo, G. Martínez-Barrera, H. López-Valdivia, H. Carrasco, V.M. Castaño, Mechanisms for the modification of nylon 6,12 by gamma irradiation, International Journal of Materials and Product Technology. 19 (2003) 521–529. https://doi.org/10.1504/IJMPT.2003.003468.

[41] L.G.P. Moraes, R.S.F. Rocha, L.M. Menegazzo, E.B. de Araújo, K. Yukimito, J.C.S. Moraes, Infrared spectroscopy: a tool for determination of the degree of conversion in dental composites, Journal of Applied Oral Science. 16 (2008) 145–149.

[42] S. Imazato, J.F. McCabe, H. Tarumi, A. Ehara, S. Ebisu, Degree of conversion of composites measured by DTA and FTIR, Dental Materials : Official Publication of the Academy of Dental Materials. 17 (2001) 178–183. https://doi.org/10.1016/S0109-5641(00)00066-X.

[43] D.R. Morgan, S. Kalachandra, H.K. Shobha, N. Gunduz, E.O. Stejskal, Analysis of a dimethacrylate copolymer (Bis-GMA and TEGDMA) network by DSC and 13C solution and solid-state NMR spectroscopy, Biomaterials. 21 (2000) 1897–1903. https://doi.org/10.1016/S0142-9612(00)00067-3.

[44] N.P. Bansal, C.H. Drummond III, Kinetics of hexacelsian-to-Celsian phase transformation in SrAl2Si2O8, Journal of the American Ceramic Society. 76 (1993) 1321–1324. https://doi.org/10.1111/j.1151-2916.1993.tb03758.x.

[45] A.K. Diab, M.M. Abd El-Raheem, E.R. Shaaban, H.M. Ali, M.M. Wakkad, Y.A. Taya, E.S. Yousef, Crystallization kinetics of Pb12Ge12Se76 chalcogenide glass, Phase Transitions. 93 (2020) 323–337. https://doi.org/10.1080/01411594.2020.1723017 Crystallization.

[46] M. Yoshida, M. Asano, I. Kaetsu, Y. Morita, Characteristics of polymer microspheres prepared by radiation-induced polymerization in the presence of organic solvents, International Journal of Radiation Applications and Instrumentation. Part C. Radiation Physics and Chemistry. 30 (1987) 39–45. https://doi.org/https://doi.org/10.1016/1359-0197(87)90148-2.

[47] Y. Naka, K. I, Y. Yamamoto, K. Hayashi, Preparation of microspheres by radiation-induced polymerization. I. Mechanism for the formation of monodisperse poly(diethylene glycol dimethacrylate) microspheres, Journal of Polymer Science Part A: Polymer Chemistry. 29 (1991) 1197–1202. https://doi.org/10.1002/pola.1991.080290814.

[48] Y. Naka, Y. Yamamoto, K. Hayashi, Solvent effects on the formation of cross-linking

microspheres in γ-irridiated solutions, International Journal of Radiation Applications and Instrumentation. Part C. Radiation Physics and Chemistry. 40 (1992) 83–88. https://doi.org/https://doi.org/10.1016/1359-0197(92)90062-K.

[49]   V. Perumal, P.M. Sivakumar, A. Zarrabi, S. Muthupandian, S. Vijayaraghavalu, K. Sahoo, A. Das, S. Das, S.S. Payyappilly, S. Das, Near infra-red polymeric nanoparticle based optical imaging in Cancer diagnosis, Journal of Photochemistry and Photobiology B: Biology. 199 (2019) 111630. https://doi.org/https://doi.org/10.1016/j.jphotobiol.2019.111630.

[50]   R.C. Mundargi, V.R. Babu, V. Rangaswamy, P. Patel, T.M. Aminabhavi, Nano/micro technologies for delivering macromolecular therapeutics using poly(d,l-lactide-co-glycolide) and its derivatives, Journal of Controlled Release. 125 (2008) 193–209. https://doi.org/https://doi.org/10.1016/j.jconrel.2007.09.013.

[51]   L. Tian, X. Li, P. Zhao, Z. Ali, Q. Zhang, Impressed pressure-facilitated seeded emulsion polymerization: Design of fast swelling strategies for massive fabrication of patchy microparticles, Polymer Chemistry. 7 (2016) 7078–7085. https://doi.org/10.1039/c6py01778a.

[52]   X.-W. Ni, H. Shen, L. Chen, G. Wu, R. Lu, T. Miyakoshi, Synthesis of polyimide microparticles by dispersion polymerization, Journal of Applied Polymer Science. 113 (2009) 3671–3675. https://doi.org/10.1002/app.30365.

[53]   K. Rattanasaikaew, A. Chaiyasat, P. Chaiyasat, Secondary particle formation in suspension polymerization using a particulate surfactant, Polymer-Plastics Technology and Materials. 59 (2020) 1801–1811. https://doi.org/10.1080/25740881.2020.1765386.

[54]   H. Yabu, Creation of functional and structured polymer particles by self-organized precipitation (SORP), Bulletin of the Chemical Society of Japan. 85 (2012) 265–274. https://doi.org/10.1246/bcsj.20110197.

[55]   A. Akhavan, E. Ataeevarjovi, The effect of gamma irradiation and surfactants on the size distribution of nanoparticles based on soluble starch, Radiation Physics and Chemistry. 81 (2012) 913–914. https://doi.org/https://doi.org/10.1016/j.radphyschem.2012.03.004.

[56]   A.P. Demchenko, Photobleaching of organic fluorophores: quantitative characterization, mechanisms, protection, Methods and Applications in Fluorescence. 8 (2020) 22001. https://doi.org/10.1088/2050-6120/ab7365.

[57]   Y. Yang, Z. Wen, Y. Dong, M. Gao, Incorporating CdTe nanocrystals into polystyrene microspheres: towards robust fluorescent beads, Small. 2 (2006) 898–901. https://doi.org/10.1002/smll.200600086.

[58]   M.R. Karim, J.H. Yeum, M.S. Lee, K.T. Lim, Preparation of conducting polyaniline/TiO2 composite submicron-rods by the γ-radiolysis oxidative polymerization method, Reactive and Functional Polymers. 68 (2008) 1371–1376. https://doi.org/https://doi.org/10.1016/j.reactfunctpolym.2008.06.016.

[59]   M. Fleischmann, P.J. Hendra, A.J. McQuillan, Raman spectra of pyridine adsorbed at a silver electrode, Chemical Physics Letters. 26 (1974) 163–166. https://doi.org/10.1016/0009-2614(74)85388-1.

[60]   P. Pal, A. Bonyár, M. Veres, L. Himics, L. Balázs, L. Juhász, I. Csarnovics, A
       generalized exponential relationship between the surface-enhanced Raman scattering
       (SERS) efficiency of gold/silver nanoisland arrangements and their non-dimensional
       interparticle distance/particle diameter ratio, Sensors and Actuators, A: Physical. 314
       (2020). https://doi.org/10.1016/j.sna.2020.112225.

[61]   P.A. Mosier-Boss, Review of SERS substrates for chemical sensing, Nanomaterials. 7
       (2017) 142. https://doi.org/10.3390/nano7060142.

[62]   R.F. Aroca, R.A. Alvarez-Puebla, N. Pieczonka, S. Sanchez-Cortez, J. V Garcia-
       Ramos, Surface-enhanced Raman scattering on colloidal nanostructures, Advances in
       Colloid and Interface Science. 116 (2005) 45–61.
       https://doi.org/10.1016/j.cis.2005.04.007.

[63]   Q. Guo, M. Xu, Y. Yuan, R. Gu, J. Yao, Self-assembled large-scale monolayer of Au
       nanoparticles at the air/water interface used as a SERS substrate, Langmuir. 32 (2016)
       4530–4537. https://doi.org/10.1021/acs.langmuir.5b04393.

[64]   F. Svec, Porous polymer monoliths: Amazingly wide variety of techniques enabling
       their preparation, Journal of Chromatography A. 1217 (2010) 902–924.
       https://doi.org/https://doi.org/10.1016/j.chroma.2009.09.073.

[65]   D. Connolly, S. Currivan, B. Paull, Polymeric monolithic materials modified with
       nanoparticles for separation and detection of biomolecules: A review, PROTEOMICS.
       12 (2012) 2904–2917. https://doi.org/https://doi.org/10.1002/pmic.201200142.

[66]   J. Liu, I. White, D.L. DeVoe, Nanoparticle-Functionalized Porous Polymer Monolith
       Detection Elements for Surface-Enhanced Raman Scattering, Analytical Chemistry. 83
       (2011) 2119–2124. https://doi.org/10.1021/ac102932d.

[67]   X. Wang, Y. Du, Q. Li, T. Wu, H. Hu, Y. Xu, H. Zhang, Y. Pan, Fabrication of
       uniform substrate based on silver nanoparticles decorated glycidyl methacrylate-
       ethylene dimethacrylate porous material for ultrasensitive surface-enhanced Raman
       scattering detection, Journal of Raman Spectroscopy. 45 (2014) 47–53.
       https://doi.org/https://doi.org/10.1002/jrs.4418.

[68]   Y. Xu, Q. Cao, F. Svec, J.M.J. Fréchet, Porous Polymer Monolithic Column with
       Surface-Bound Gold Nanoparticles for the Capture and Separation of Cysteine-
       Containing Peptides, Analytical Chemistry. 82 (2010) 3352–3358.
       https://doi.org/10.1021/ac1002646.

[69]   Q. Jiang, T. Zeng, S. Yang, Q. Chen, L. Chen, Y. Ye, J. Zhou, S. Xu, On-column
       enrichment and surface-enhanced Raman scattering detection in nanoparticles
       functionalized porous capillary monolith, Spectrochimica Acta Part A: Molecular and
       Biomolecular Spectroscopy. 141 (2015) 244–251.
       https://doi.org/10.1016/j.saa.2015.01.044.

[70]   T.N. Raja, A.M. Brouwer, Fluorescence Spectroscopy in Polymer Science BT -
       Advanced Fluorescence Reporters in Chemistry and Biology III: Applications in
       Sensing and Imaging, in: A.P. Demchenko (Ed.), Springer Berlin Heidelberg, Berlin,
       Heidelberg, 2011: pp. 91–117. https://doi.org/10.1007/978-3-642-18035-4_3.

[71]   H.B. Bebb, E.W. Williams, Photoluminescence I: Theory, Semiconductors and

Semimetals. 8 (1972) 181–320. https://doi.org/10.1016/S0080-8784(08)62345-5.

[72]   Y. Ding, J. Lee, J. Ma, K. Sung, T. Yokota, N. Singh, M. Dooraghi, P. Abiri, Y. Wang, R.P. Kulkarni, Light-sheet fluorescence imaging to localize cardiac lineage and protein distribution, Scientific Reports. 7 (2017) 42209.

[73]   G.N. McKay, R.C. Niemeier, C. Castro-González, N.J. Durr, Scattering oblique plane microscopy for in-vivo blood cell imaging, Biomedical Optics Express. 12 (2021) 2575–2585. https://doi.org/10.1364/BOE.422993.

[74]   J.M. Girkin, M.T. Carvalho, The light-sheet microscopy revolution, Journal of Optics. 20 (2018) 53002. https://doi.org/10.1088/2040-8986/aab58a.

[75]   P.J. Keller, H.-U. Dodt, Light sheet microscopy of living or cleared specimens, Current Opinion in Neurobiology. 22 (2012) 138–143. https://doi.org/10.1016/j.conb.2011.08.003.

[76]   A.H. Voie, D.H. Burns, F.A. Spelman, Orthogonal-plane fluorescence optical sectioning: Three-dimensional imaging of macroscopic biological specimens, Journal of Microscopy. 170 (1993) 229–236. https://doi.org/10.1111/j.1365-2818.1993.tb03346.x.

[77]   P.A. Santi, Light sheet fluorescence microscopy: A review, Journal of Histochemistry and Cytochemistry. 59 (2011) 129–138. https://doi.org/10.1369/0022155410394857.

[78]   J. Huisken, J. Swoger, F. Del Bene, J. Wittbrodt, E.H.K. Stelzer, Optical sectioning deep inside live embryos by selective plane illumination microscopy, Science. 305 (2004) 1007–1009. https://doi.org/10.1126/science.1100035.

[79]   K. Greger, J. Swoger, E.H.K. Stelzer, Basic building units and properties of a fluorescence single plane illumination microscope, Review of Scientific Instruments. 78 (2007) 7. https://doi.org/10.1063/1.2428277.

[80]   L. Gao, L. Shao, B.-C. Chen, E. Betzig, 3D live fluorescence imaging of cellular dynamics using Bessel beam plane illumination microscopy, Nature Protocols. 9 (2014) 1083–1101. https://doi.org/10.1038/nprot.2014.087.

[81]   R. Tobias, Phonon Raman Scattering in Semiconductors, Quantum Wells and Superlattices Basic Results and Applications, (1998). https://doi.org/10.1007/BFb0110684.

[82]   L.T. Hoang, H. Van Pham, M.T.T. Nguyen, Investigation of the Factors Influencing the Surface-Enhanced Raman Scattering Activity of Silver Nanoparticles, Journal of Electronic Materials. 49 (2020) 1864–1871. https://doi.org/10.1007/s11664-019-07870-8.

[83]   N. Guillot, M.L. de la Chapelle, The electromagnetic effect in surface enhanced Raman scattering: Enhancement optimization using precisely controlled nanostructures, Journal of Quantitative Spectroscopy and Radiative Transfer. 113 (2012) 2321–2333. https://doi.org/10.1016/j.jqsrt.2012.04.025.

[84]   C. V RAMAN, K.S. KRISHNAN, A New Type of Secondary Radiation, Nature. 121 (1928) 501–502. https://doi.org/10.1038/121501c0.

[85] Z. Movasaghi, S. Rehman, I.U. Rehman, Raman spectroscopy of biological tissues, Applied Spectroscopy Reviews. 42 (2007) 493–541. https://doi.org/10.1080/05704920701551530.

[86] M.E. Keating, H.J. Byrne, Raman spectroscopy in nanomedicine: current status and future perspective, Nanomedicine. 8 (2013) 1335–1351. https://doi.org/10.2217/nnm.13.108.

[87] S.P.S. Porto, D.L. Wood, Ruby Optical Maser as a Raman Source, Journal of the Optical Society of America. 52 (1962) 251–252. https://doi.org/10.1364/JOSA.52.000251.

[88] H. Kogelnik, S.P.S. Porto, Continuous Helium–Neon Red Laser as a Raman Source, Journal of the Optical Society of America. 53 (1963) 1446–1447. https://doi.org/10.1364/JOSA.53.001446.

[89] H. Susi, J.S. Ard, Laser-raman spectra of lactose, Carbohydrate Research. 37 (1974) 351–354. https://doi.org/https://doi.org/10.1016/S0008-6215(00)82924-9.

[90] G.J. Puppels, A. Huizinga, H.W. Krabbe, H.A. De Boer, G. Gijsbers, F.F.M. De Mul, A high-throughput Raman notch filter set, Review of Scientific Instruments. 61 (1990) 3709–3712. https://doi.org/10.1063/1.1141963.

[91] M. Delhaye, P. Dhamelincourt, Raman microprobe and microscope with laser excitation, Journal of Raman Spectroscopy. 3 (1975) 33–43. https://doi.org/10.1002/jrs.1250030105.

[92] P.J. Larkin, Infrared and Raman Spectroscopy: Principles and Spectral Interpretation, 2011.

[93] M.J. Baker, C.S. Hughes, K.A. Hollywood, Raman spectroscopy, Biophotonics: Vibrational Spectroscopic Diagnostics. (2016) 3–13. https://doi.org/10.1088/978-1-6817-4071-3ch3.

[94] G. Turrel, J. Corset, Raman Microscopy_ Developments and Applications, (1996).

[95] G.P.R. Chalmers J. M., Handbook of Vibrational Spectroscopy, Journal of the American Chemical Society. 124 (2002) 9958. https://doi.org/10.1021/ja025228w.

[96] R.L. McCreery, Raman spectroscopy for chemical analysis, John Wiley & Sons, 2005.

[97] M.S. Amer, Raman spectroscopy, fullerenes and nanotechnology, RSC Nanoscience and Nanotechnology. (2010) 1–301.

[98] A.L. Derek, The Raman Effect: A Unified Treatment of the Theory of Raman Scattering by Molecules, John Wiley & Sons Ltd, Baffins Lane, Chichester, England, 2002. https://doi.org/10.1038/125205a0.

[99] H. Li, D. Men, Y. Sun, D. Liu, X. Li, L. Li, C. Li, W. Cai, Y. Li, Surface enhanced Raman scattering properties of dynamically tunable nanogaps between Au nanoparticles self-assembled on hydrogel microspheres controlled by pH, Journal of Colloid and Interface Science. 505 (2017) 467–475. https://doi.org/10.1016/j.jcis.2017.06.034.

[100] X. Xu, H. Li, D. Hasan, R.S. Ruoff, A.X. Wang, D.L. Fan, Near-field enhanced plasmonic-magnetic bifunctional nanotubes for single cell bioanalysis, Advanced Functional Materials. 23 (2013) 4332–4338. https://doi.org/10.1002/adfm.201203822.

[101] D.L. Jeanmaire, R.P.V. Duyne, Surface Raman Spectroelectrochemistry, Journal Electroanal Chemistry. 84 (1977) 1–20. https://doi.org/10.1016/S0022-0728(77)80224-6.

[102] M.G. Albrecht, J.A. Creighton, Anomalously Intense Raman-Spectra of Pyridine at a Silver Electrode, Journal of the Americal Chemical Society. 99 (1977) 5215–5217. https://doi.org/10.1021/ja00457a071.

[103] M. Moskovits, Surface roughness and the enhanced intensity of Raman scattering by molecules adsorbed on metals, The Journal of Chemical Physics. 69 (1978) 4159–4161. https://doi.org/10.1063/1.437095.

[104] M. Moskovits, Surface-enhanced spectroscopy, Reviews of Modern Physics. 57 (1985) 783. https://doi.org/10.1103/RevModPhys.57.783.

[105] A. Campion, P. Kambhampati, A. Campion, C. Harris, Surface-enhanced Raman scattering, Chemical Society Reviews. 27 (1998) 241–250. https://doi.org/10.1039/A827241Z.

[106] M. Prochazka, Basics of Surface-Enhanced Raman Scattering (SERS), in: Springer International Publishing, 2016: pp. 21–59. https://doi.org/10.1007/978-3-319-23992-7_3.

[107] E.C. Le Ru, P.G. Etchegoin, Principles of surface-enhanced Raman spectroscopy: and related plasmonic effects, Elsevier, 2009.

[108] S. Schlücker, Surface-Enhanced raman spectroscopy: Concepts and chemical applications, Angewandte Chemie International Edition. 53 (2014) 4756–4795. https://doi.org/10.1002/anie.201205748.

[109] L. Jensen, C.M. Aikens, G.C. Schatz, Electronic structure methods for studying surface-enhanced Raman scattering, Chemical Society Reviews. 37 (2008) 1061–1073. https://doi.org/10.1039/B706023H.

[110] M.A. Ordal, L.L. Long, R.J. Bell, S.E. Bell, R.R. Bell, R.W. Alexander, C.A. Ward, Optical properties of the metals Al, Co, Cu, Au, Fe, Pb, Ni, Pd, Pt, Ag, Ti, and W in the infrared and far infrared, Appl. Opt. 22 (1983) 1099–1119. https://doi.org/10.1364/AO.22.001099.

[111] Jenő Sólyom, Fundamentals of the Physics of Solids :, Volume III, Springer, 2010. https://doi.org/10.1007/978-3-642-04518-9.

[112] N.W. Ashcroft, N.D. Mermin, Solid state physics, new york London, 1976.

[113] V. Amendola, R. Pilot, M. Frasconi, O.M. Maragò, M.A. Iatì, Surface plasmon resonance in gold nanoparticles: A review, Journal of Physics Condensed Matter. 29 (2017). https://doi.org/10.1088/1361-648X/aa60f3.

[114] A.M. Stefan, Plasmonics: Fundamentals and Applications, Springer Science, Business Media LLC, United Kingdom, 2007.

[115] K.A. Willets, R.P.V. Duyne, Localized surface plasmon resonance spectroscopy and sensing, Annual Review of Physical Chemistry. 58 (2007) 267–297. https://doi.org/10.1146/annurev.physchem.58.032806.104607.

[116] T.K. Sarkar, M.N. Abdallah, M. Salazar-Palma, W.M. Dyab, Surface Plasmons-Polaritons, Surface Waves, and Zenneck Waves: Clarification of the terms and a description of the concepts and their evolution., IEEE Antennas and Propagation Magazine. 59 (2017) 77–93. https://doi.org/10.1109/MAP.2017.2686079.

[117] Q. Tan, X. Huang, W. Zhou, K. Yang, A Plasmonic based Ultracompact Polarization Beam Splitter on Silicon-on-Insulator Waveguides, Scientific Reports. 3 (2013). https://doi.org/10.1038/srep02206.

[118] J.R. Lakowicz, Plasmonics in biology and plasmon-controlled fluorescence, Plasmonics. 1 (2006) 5–33. https://doi.org/10.1007/s11468-005-9002-3.

[119] M. Li, S.K. Cushing, N. Wu, Plasmon-enhanced optical sensors: A review, Analyst. 140 (2015) 386–406. https://doi.org/10.1039/c4an01079e.

[120] E.C. Le Ru, E. Blackie, M. Meyer, P.G. Etchegoint, Surface enhanced raman scattering enhancement factors: A comprehensive study, Journal of Physical Chemistry C. 111 (2007) 13794–13803. https://doi.org/10.1021/jp0687908.

[121] S. Bai, D. Serien, A. Hu, K. Sugioka, 3D Microfluidic Surface-Enhanced Raman Spectroscopy (SERS) Chips Fabricated by All-Femtosecond-Laser-Processing for Real-Time Sensing of Toxic Substances, Advanced Functional Materials. 28 (2018) 1–10. https://doi.org/10.1002/adfm.201706262.

[122] G. Zhu, L. Cheng, G. Liu, L. Zhu, Synthesis of gold nanoparticle stabilized on silicon nanocrystal containing polymer microspheres as effective surface-enhanced raman scattering (SERS) substrates, Nanomaterials. 10 (2020) 1–9. https://doi.org/10.3390/nano10081501.

[123] F.M. Spiga, A. Bonyár, B. Ring, M. Onofri, A. Vinelli, H. Sántha, C. Guiducci, G. Zuccheri, Hybridization chain reaction performed on a metal surface as a means of signal amplification in SPR and electrochemical biosensors, Biosensors and Bioelectronics. 54 (2014) 102–108. https://doi.org/10.1016/j.bios.2013.10.036.

[124] T. Lednický, A. Bonyár, Large Scale Fabrication of Ordered Gold Nanoparticle-Epoxy Surface Nanocomposites and Their Application as Label-Free Plasmonic DNA Biosensors, ACS Applied Materials and Interfaces. 12 (2020) 4804–4814. https://doi.org/10.1021/acsami.9b20907.

[125] B.J. Inkson, Scanning electron microscopy (SEM) and transmission electron microscopy (TEM) for materials characterization, in: Materials Characterization Using Nondestructive Evaluation (NDE) Methods, Elsevier, 2016: pp. 17–43. https://doi.org/10.1016/B978-0-08-100040-3.00002-X.

[126] J. Huang, T. Cavanaugh, B. Nur, An Introduction to SEM Operational Principles and Geologic Applications for Shale Hydrocarbon Reservoirs, (2013). https://doi.org/10.1306/13391699M1023580.

[127] A.A. Bunaciu, V.D. Hoang, H.Y. Aboul-Enein, Vibrational micro-spectroscopy of human tissues analysis, Critical Reviews in Analytical Chemistry. 47 (2017) 194–203.

https://doi.org/10.1080/10408347.2016.1253454.

[128] M.J. Frisch, G.W. Trucks, H.B. Schlegel, G.E. Scuseria, M.A. Robb, J.R. Cheeseman, G. Scalmani, V. Barone, B. Mennucci, Ga. Petersson, Gaussian 09, Revision d. 01, Gaussian, Inc., Wallingford CT. 201 (2009) 150–166.

[129] A.D. Becke, Density-fnnctional exchange-energy approximation with correct asymptotic behavior, Physical Review A. 38 (1988) 3098–3100. https://doi.org/10.1063/1.1749835.

[130] C. Lee, W. Yang, R. G. Parr, Development of the Colic-Salvetti correlation-energy formula into a functional of the electron density, Physical Review B. 37 (1988) 785–789. https://doi.org/10.1103/PhysRevB.37.785.

[131] V.A. Rassolov, J.A. Pople, M.A. Ratner, T.L. Windus, 6-31G* basis set for atoms K through Zn, Journal of Chemical Physics. 109 (1998) 1223–1229. https://doi.org/10.1063/1.476673.

[132] J.L. Holmes, J.C. Lindon, G.E. Tranter, Encyclopedia of Spectroscopy and Spectrometry (3-Volume Set with Online Version), (2000) 2690.

[133] G.R. Hayes, B. Deveaud, Is luminescence from quantum wells due to excitons?, Physica Status Solidi (A) Applied Research. 190 (2002) 637–640. https://doi.org/10.1002/1521-396X(200204)190:3<637::AID-PSSA637>3.0.CO;2-7.

[134] S. Yu, F. Ng, K. Ma, A. Mon, F. Ng, Y. Ng, Effect of Porogenic Solvent on the Porous Properties of Polymer Monoliths, Journal of Applied Polymer Science. 127 (2013) 2641–2647. https://doi.org/10.1002/app.37514.

[135] M.B. Moran, G.C. Martin, The Laser Raman Spectrum of Polyethylene Glycol Dimethacrylate), Journal of Macromolecular Science: Part A - Chemistry. 19 (1983) 611–618. https://doi.org/10.1080/10601328308056538.

[136] M. Uygun, W.D. Cook, C. Moorhoff, F. Chen, C. Vallo, Y. Yagci, M. Sangermano, Photopolymerization Kinetics and Dynamic Mechanical Properties of Silanes Hydrolyzed without Evolution of Byproducts. Tetrakis[(methacryloyloxy)ethoxy]silane−Diethylene Glycol Dimethacrylate, Macromolecules. 44 (2011) 1792–1800. https://doi.org/10.1021/ma102903q.

[137] M.A. Gauthier, I. Stangel, T.H. Ellis, X.X. Zhu, A new method for quantifying the intensity of the C=C band of dimethacrylate dental monomers in their FTIR and Raman spectra, Biomaterials. 26 (2005) 6440–6448. https://doi.org/https://doi.org/10.1016/j.biomaterials.2005.04.039.

[138] D. Sinha, K.L. Sahoo, U.B. Sinha, T. Swu, A. Chemseddine, D. Fink, Gamma-induced modifications of polycarbonate polymer, Radiation Effects and Defects in Solids. 159 (2004) 587–595. https://doi.org/10.1080/10420150412331330539.

[139] K. Filipecka, R. Miedziński, M. Sitarz, J. Filipecki, M. Makowska-Janusik, Optical and vibrational properties of phosphorylcholine-based contact lenses—Experimental and theoretical investigations, Spectrochimica Acta - Part A: Molecular and Biomolecular Spectroscopy. 176 (2017) 83–90. https://doi.org/10.1016/j.saa.2017.01.013.

[140] J. Chen, J. Li, L. X, W. Hong, Y. Yang, X. Chen, The Glass-Transition Temperature of

Supported PMMA Thin Films with Hydrogen Bond/Plasmonic Interface, Polymers. 11 (2019) 601. https://doi.org/10.3390/polym11040601.

[141] M. Par, O. Gamulin, N. Spanovic, R. Bjelovucic, Z. Tarle, The effect of excitation laser power in Raman spectroscopic measurements of the degree of conversion of resin composites, Dental Materials. 35 (2019) 1227–1237. https://doi.org/10.1016/j.dental.2019.05.018.

[142] T.K. Vaidyanathan, J. Vaidyanathan, P.P. Lizymol, S. Ariya, K.V. Krishnan, Study of visible light activated polymerization in BisGMA-TEGDMA monomers with Type 1 and Type 2 photoinitiators using Raman spectroscopy, Dental Materials. 33 (2017) 1–11. https://doi.org/10.1016/j.dental.2016.09.002.

[143] C.O. Navarra, M. Cadenaro, B. Codan, A. Mazzoni, V. Sergo, E. De Stefano Dorigo, L. Breschi, Degree of conversion and interfacial nanoleakage expression of three one-step self-etch adhesives, European Journal of Oral Sciences. 117 (2009) 463–469. https://doi.org/10.1111/j.1600-0722.2009.00654.x.

[144] L.E.S. Soares, A.A. Martin, A.L.B. Pinheiro, Degree of Conversion of Composite Resin: A Raman Study, Journal of Clinical Laser Medicine and Surgery. 21 (2003) 357–362. https://doi.org/10.1089/104454703322650167.

[145] J. Málek, T. Mitsuhashi, Testing method for the Johnson–Mehl–Avrami equation in kinetic analysis of crystallization processes, Journal of the American Ceramic Society. 83 (2000) 2103–2105. https://doi.org/10.1111/j.1151-2916.2000.tb01523.x.

[146] N.V. Tarasenko, A.V. Butsen, E.A. Nevar, N.A. Savastenko, Synthesis of nanosized particles during laser ablation of gold in water, Applied Surface Science. 252 (2006) 4439–4444. https://doi.org/https://doi.org/10.1016/j.apsusc.2005.07.150.

[147] C. Rossner, T.A.F. König, A. Fery, Plasmonic Properties of Colloidal Assemblies, Advanced Optical Materials. 2001869 (2021). https://doi.org/10.1002/adom.202001869.

[148] N.G. Bastús, E. Casals, I. Ojea, M. Varon, V. Puntes, The Reactivity of Colloidal Inorganic Nanoparticles, The Delivery of Nanoparticles. (2012). https://doi.org/10.5772/35238.

[149] S. Sahoo, A.P.S. Gaur, M. Ahmadi, M.J.F. Guinel, R.S. Katiyar, Temperature-dependent Raman studies and thermal conductivity of few-layer MoS2, Journal of Physical Chemistry C. 117 (2013) 9042–9047. https://doi.org/10.1021/jp402509w.

[150] R.M. Sarhan, W. Koopman, R. Schuetz, T. Schmid, F. Liebig, J. Koetz, M. Bargheer, The importance of plasmonic heating for the plasmon-driven photodimerization of 4-nitrothiophenol, Scientific Reports. 9 (2019) 1–8. https://doi.org/10.1038/s41598-019-38627-2.

[151] M. Liu, R. Xiang, Y. Lee, K. Otsuka, Y.L. Ho, T. Inoue, S. Chiashi, J.J. Delaunay, S. Maruyama, Fabrication, characterization, and high temperature surface enhanced Raman spectroscopic performance of SiO2 coated silver particles, Nanoscale. 10 (2018) 5449–5456. https://doi.org/10.1039/c7nr08631h.

[152] H. Zhang, Z. Chen, T. Li, N. Chen, W. Xu, S. Liu, Surface-enhanced Raman scattering spectra revealing the inter-cultivar differences for Chinese ornamental Flos

Chrysanthemum: A new promising method for plant taxonomy, Plant Methods. 13 (2017) 1–11. https://doi.org/10.1186/s13007-017-0242-y.

[153] R.A. Guy, C. Xiao, P.A. Horgen, Real-time PCR assay for detection and genotype differentiation of Giardia lamblia in stool specimens, Journal of Clinical Microbiology. 42 (2004) 3317–3320. https://doi.org/10.1128/JCM.42.7.3317-3320.2004.

[154] J. Kim, H.J. Park, J.H. Kim, B. Chang, H.K. Park, Label-free detection for a DNA methylation assay using Raman spectroscopy, Chinese Medical Journal. 130 (2017) 1961–1967. https://doi.org/10.4103/0366-6999.211874.

[155] A.J.R. Chica, M.A. Medina, F.S. Jiménez, F.J. Ramírez, On the interpretation of Raman spectra of 1-aminooxy-spermine/DNA complexes, Nucleic Acids Research. 32 (2004) 579–589. https://doi.org/10.1093/nar/gkh232.

[156] H. Huang, W. Chen, J. Pan, Q. Chen, S. Feng, Y. Yu, Y. Chen, Y. Su, R. Chen, SERS spectra of a single nasopharyngeal carcinoma cell based on intracellularly grown and passive uptake Au nanoparticles, Spectroscopy. 26 (2011) 187–194. https://doi.org/10.3233/SPE-2011-0540.

[157] G.P. Szekeres, J. Kneipp, SERS probing of proteins in gold nanoparticle agglomerates, Frontiers in Chemistry. 7 (2019) 1–10. https://doi.org/10.3389/fchem.2019.00030.

[158] H. Huang, H. Shi, S. Feng, W. Chen, Y. Yu, D. Lin, R. Chen, Confocal Raman spectroscopic analysis of the cytotoxic response to cisplatin in nasopharyngeal carcinoma cells, Analytical Methods. 5 (2013) 260–266. https://doi.org/10.1039/c2ay25684c.
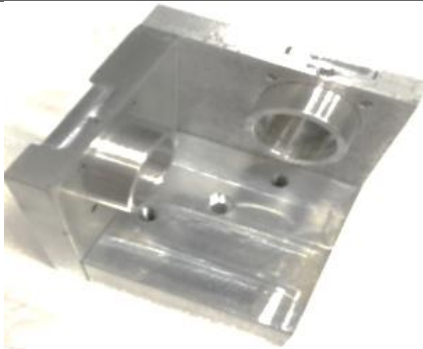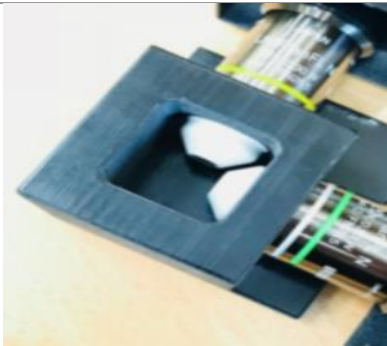
Appendix A

LSFM system that was built and used in the study.
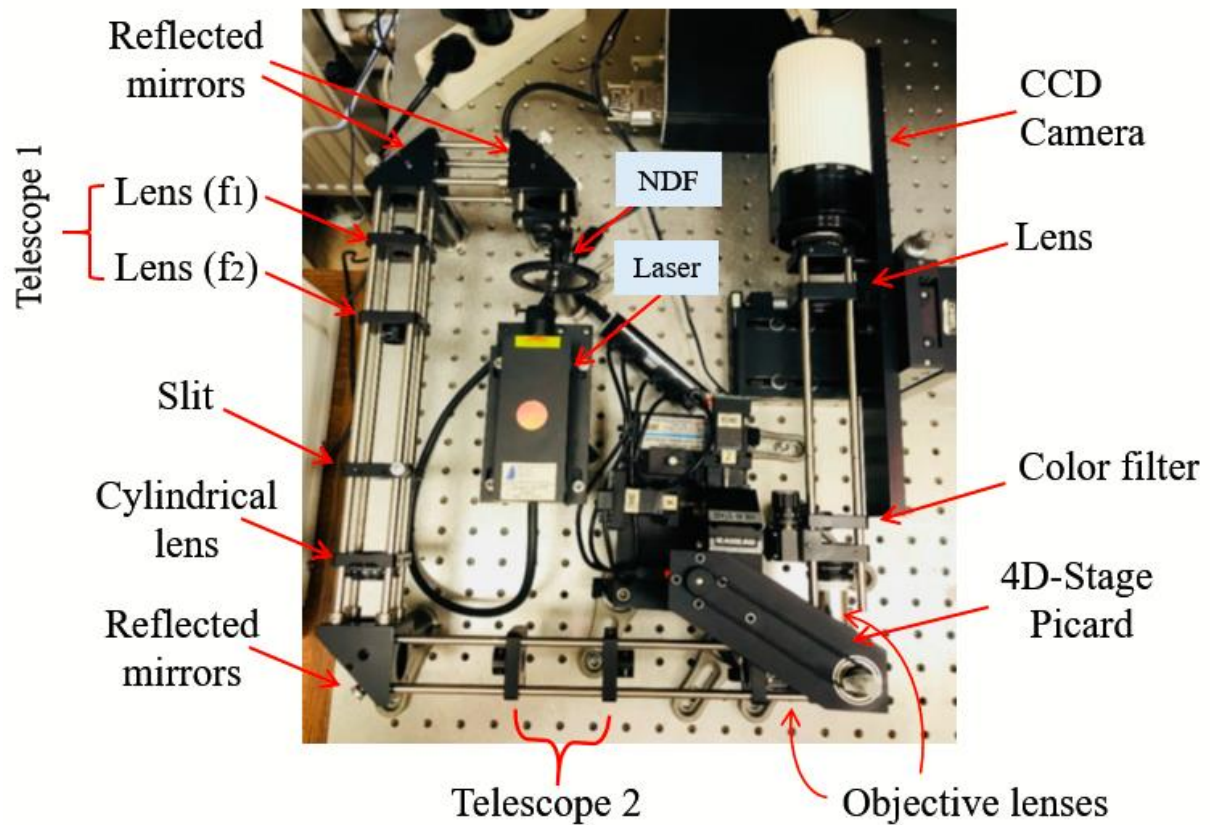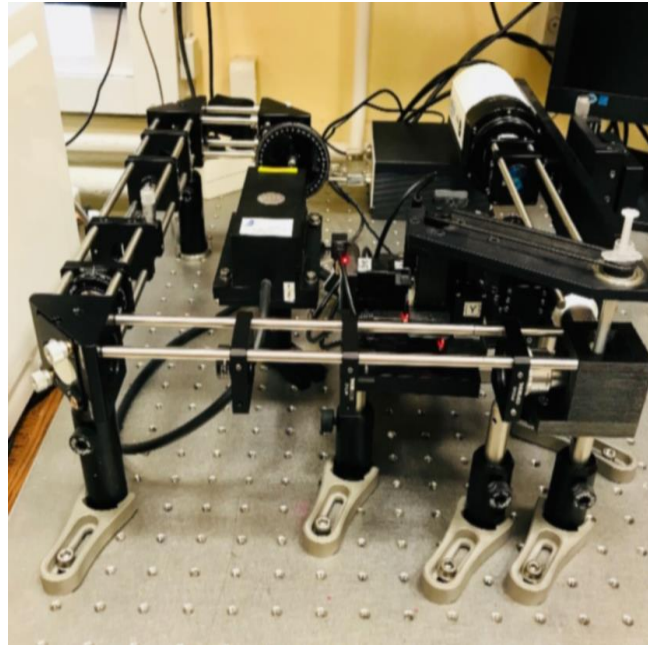
Appendix B

Images of the self made tools for the LSFM.

Description	Image	Manufacturer
Chamber Holder-Aluminum		Self made
Sample Chamber-Plastic		Self made